A structural-metamorphic approach to deciphering the exhumation of the Gubaoquan eclogite in the Beishan Orogenic Collage, NW China

by

Jordy de Vries

A thesis
presented to the University of Waterloo
in fulfilment of the
thesis requirement for the degree of
Master of Science
in
Earth Sciences

Waterloo, Ontario, Canada, 2020

AUTHOR'S DECLARATION

I hereby declare that I am the sole author of this thesis. This is a true copy of the thesis, including any required final revisions, as accepted by my examiners.

I understand that my thesis may be made electronically available to the public.

Abstract

The Ordovician Gubaoquan eclogite is situated in the southern part of the Palaeozoic Beishan Orogenic Collage of the Central Asian Orogenic Belt in NW China. Mapping of an extensive section of the metamorphic tectonite belt around the eclogite and optical petrography have uncovered a high degree of fabric preservation, not recognised by earlier studies.

The study area is underlain by a highly deformed belt of metamorphic tectonites, intruded by syn-tectonic granitoids. The belt largely consists of D_3 retrograde fabrics, with only local preservation of D_1 eclogite-facies fabrics in the cores of mafic boudins. Fabrics associated with D_1-D_4 document a clockwise metamorphic trajectory, characterised by eclogite-facies metamorphism followed by a large decrease in pressure and small decrease in temperature, high-temperature low-pressure conditions and greenschist-facies metamorphism. D_2-D_4 is associated with widespread N-S shortening and local extension.

SHRIMP U-Pb dating of zircon indicates felsic orthogneiss in the area primarily has Neoproterozoic protoliths, whereas metasedimentary rocks and metabasites primarily have Mesoproterozoic protoliths. Metamorphic zircon ages indicate a protracted metamorphic history from ~470 to 420 Ma.

We propose that the metamorphic tectonite belt hosting the Gubaoquan eclogite represents Meso-/Neo-Proterozoic crust that underwent Ordovician-Silurian, north-directed subduction to various depths. The eclogite and its host were detached from the down-going slab, probably due to slab break-off, which also caused extensive syn-tectonic magmatism. Uplift and exhumation probably occurred in an extruding-wedge-type setting. Local convergence continued until the emplacement of the Silurian-Devonian granitoids. Afterwards, the area was tectonically quiescent until the Carboniferous-Triassic, when the area was exhumed.

Acknowledgements

I acknowledge the support of the China Geological Survey, the University of Waterloo and the Natural Sciences and Engineering Research Council of Canada (NSERC) grants of Shoufa Lin and Cees van Staal.

Dedication

First, I would like to thank Cees and Shoufa for letting me be part of this research project and supporting me throughout. I learned a lot from your feedback and our discussions, which allowed me to greatly improve my thesis. I am also very grateful to Chris, for your support, feedback and insights on the metamorphic and geochronological sides of things. Frank Beunk kindly let me use his own microscope at the VU, allowing me to finish my analyses from the Netherlands during the pandemic - thanks a lot for your hospitality and guidance with optical petrography. I also received invaluable help and inspiration from the rest of the China gang – Gabriel, Tong and Quinn - without whom all the days in Liuyuan would have been a lot longer! I also spent a lot of time in the field with Lingchao, with whom I had a great time discussing geology and other things. I would also like to thank Ameerah and Grant, for their support on the days when things were not quite going as planned. And Peter Jan, Ian, Bieke and Pieter– your proofreading and insightful feedback really helped me improve my thesis! Yueting Song, Liu Shu, Chaoyang Wang, Lamei Feng, Yanfei Xia, Peng Song and Li Xun all provided invaluable assistance with field work, translating and interpreting. Lastly, several drivers tirelessly helped me in the field, particularly Mr. Tan, Yang and Wu. But last and very much not least, I would not have been able to complete this thesis without those in Europe who managed to support me despite the distance and time difference, in particular my family, Laura, Darya, Peter Jan, Pieter, Bieke, Lara, Tanvi, Ian, Chiara and Loren.

Table of Contents

List of Figures

List of Tables

List of abbreviations

am – amphibole
and - andalusite
BOC – Beishan Orogenic Collage
BSE – Back-Scatter Electron
bt - biotite
CAOB – Central Asian Orogenic Belt
CL – Cathodoluminescence
COLG – Collisional Granite
cpx – clinopyroxene
CRB – Continental Ridge Basalt
E/N MORB – Enriched/Normal Mid-Oceanic Ridge Basalt
GBQ – Gubaoquan
grt - garnet
HP(LT) – High Pressure (- Low Temperature)
IAB – Island Arc Basalt
ICP-MS/AES – Inductively Coupled Plasma Micro Spectroscopy / Atomic Emission Spectroscopy
ky – kyanite
LOI – Loss On Ignition
LY – Liuyuan
mv - white mica
OIB – Oceanic Island Basalt
omp – omphacite
ORB – Oceanic Ridge Basalt
ORG – Orogenic Granite
Pb_c = common lead
Pb^* = radiogenic lead
plg – plagioclase
P-T-t-D – Pressure-Temperature-time-Deformation
q – quartz
rut – rutile
sill – sillimanite
SHRIMP – Sensitive High-Resolution Ion MicroProbe
st – staurolite
sym – symplectite
SZ – Shear Zone
TAS – Total Alkali vs Silica
tit – titanite
VAG – Volcanic Arc Granite
WPG – Within-Plate Granite

Opening Quote

"Non est delicata res vivere. Longam viam ingressus es: et labaris oportet et arietes et cadas et lasseris et exclames: 'o mors!', id est mentiaris. Alio loco comitem relinques, alio efferes, alio timebis. Per eiusmodi offensas emetiendum est confragosum hoc iter."

- Seneca, Espitulae ad Lucilium 107, 2

"Live is not a delicate matter. You have commenced a long journey: you will slip, collide, fall, become fatigued and exclaim: 'O for death!', it means that you are lying. At one moment you will abandon a comrade, at another you will bury one, at another you will be fearful. It is amidst such falterings that this rugged journey will have to be carried out."

- Seneca, Letters to Lucilius, 107, 2

Chapter 1
Introduction

Continental eclogites are commonly hosted by predominantly felsic terranes that primarily consist of retrograde amphibolite-facies assemblages (Faryad & Cuthbert, 2020; Young & Kylander-Clark, 2015; Rumble et al., 2003). Consequently, the litho-tectonic setting of continental eclogites is difficult to constrain: they may have undergone *in-situ* eclogite-facies metamorphism along with their host, or were metamorphosed and then reached their present litho-structural association through tectonic processes (e.g. Štípská et al., 2006). *In-situ* metamorphism presently is the most accepted theory (e.g. Rumble et al., 2003), although there still exists uncertainty regarding the mechanism inhibiting the formation of eclogite-facies parageneses in the felsic hosts (e.g. dehydration; Young & Kylander-Clark, 2015; Peterman et al., 2009; Masago et al., 2010), or whether the felsic host had undergone pervasive retrogression (e.g. Cooke & O'Brien, 2001).

A key exception to this are continental eclogites that are (partially) hosted by metasedimentary rocks: particularly metapelitic rocks may occasionally preserve peak-metamorphic fabrics (Hoschek, 2013; Smye et al., 2010 and references therein) or are shown to be largely overprinted by retrograde fabrics (e.g. Skrzypek, Štípská et al., 2011; Skrzypek, Schulmann et al., 2011; Smye et al., 2010). In such retrogressed rocks, evidence for earlier deformation stages usually is only preserved as (inclusion trails in) porphyroblasts (e.g. Skrzypek, Štípská et al., 2011).

The preservation of porphyroblasts with such structures is rare in largely retrogressed terranes. Moreover, without detailed mapping and petrographic analysis, these structures may be left unnoticed. Unfortunately, many studies only conduct litho-structural mapping in small areas surrounding their outcrops and/or minimally discuss the structural context of their areas, despite such data potentially allowing for more robust tectonic models. Consequently, few studies exist that adequately integrate lithostratigraphic and structural observations with the PT-t histories of the eclogites and their continental host rock (e.g. Little et al., 2011; Skrzypek, Štípská et al., 2011; Willner et al., 2000).

This study aims to fill this gap through a detailed study of the structure and metamorphism of the Gubaoquan eclogite and the hosting metamorphic tectonite belt. The Gubaoquan eclogite in the Beishan Orogenic Collage (Gansu province, northwest China) is an excellent example of an area where detailed mapping and petrographic analysis may profoundly improve the tectonic models. Except for a few boudins that preserve eclogite-facies conditions at their cores, the metamorphic tectonite belt consists of amphibolite-facies fabrics, which nearly completely obliterated earlier fabrics. Whilst metapelites are abundant throughout the area, no eclogite-facies assemblages have been observed in the host thus far (Soldner, Štípská et al., 2020;2019; Saktura et al., 2017; Qu et al., 2011; Liu et al., 2011). This complicates constraining the relationship of these assemblages relative to eclogite-facies metamorphism. Consequently, both *ex-situ* (Soldner, Štípská et al., 2020) and *in-situ* scenarios (Saktura et al., 2017) have been proposed.

This study presents new petrographic evidence for the earliest deformation stages preserved in the metamorphic tectonite belt that hosts the Gubaoquan eclogite. A much larger area was mapped than by earlier studies, with the intention to better understand the area's litho-structural framework. Novel field and petrographic relationships allow for constraining the relationships between the various deformation stages. New geochronological analyses provide additional constraints on the area's parentage and the timing of metamorphic events across the area. Additionally, new litho-structural observations of the Ordovician-Silurian plutons elucidate how the area's structure and metamorphism relate to its igneous history. By integrating all observations, novel insights are given into the uplift and exhumation of the eclogite and a new tectonic model is proposed. In this way, the Gubaoquan eclogite will exemplify the value of extensive field work and petrographic analysis when trying to understand continental eclogite formation.

Chapter 2
Background

2.1 Geology of the Central Asian Orogenic Belt

The Central Asian Orogenic Belt (CAOB) is one of the largest accretionary orogens on this planet. It is considered as one of the most expansive crustal growth events in Earth history (Hong et al., 2004; Şengör et al., 1993), although this has been disputed (Kröner et al., 2017; 2014). The orogen formed through the accretion of multiple arcs, ophiolites, accretionary wedges and other features against the margins of the Baltica, Siberia and North China cratons (Figure 1) (Xiao et al., 2018; Windley et al., 2007). The orogen is thought to testify for the closure of a major ocean originally lying between these cratons, the Palaeo-Asian Ocean (Xiao et al., 2018). The closure of this ocean may have started as early as the Neoproterozoic (Windley et al., 2007) and may be related to the break-up of Rodinia (Zhao et al., 2018; Kovalenko et al., 2004). The final closure would have been marked by the formation of the Solonker suture zone during the Permian or early Triassic (Li et al., 2014; Xiao et al., 2003). The most accepted tectonic model for the CAOB is an Indonesian-type model, where multiple microcontinents and arcs were simultaneously active (Xiao et al., 2018; Windley et al., 2007). A Kipchak model with one (Şengör et al., 1993) to three (Yakubchuk, 2004) active arcs has also been proposed.

2.2 Geology of the Beishan orogenic collage

The Beishan Orogenic Collage (BOC) is situated in the south-eastern CAOB. Major faults separate it from the Dunhuang Tectonic Belt to the south and the Southern Mongolian arc system to the north (Figure 2). It is positioned along the same sutures that separate the Tarim from the Tianshan in the west, and those that separate the North China craton and the Southern Mongolia accretionary orogen in the east (Cleven et al., 2016). Being in this strategic position, the BOC could play an important role in correlating observations from both orogens. In fact, some consider the BOC as the eastern continuation of the Tianshan, although cross-orogen correlations are only in a preliminary stage (Shi et al., 2014).

The belt is composed of several E-W-striking units, comprising arcs, ophiolites and metamorphic belts (Saktura et al., 2017; Xiao et al., 2010). Continental growth and local convergence may have commenced as early as the Neoproterozoic, whilst final ocean closure occurred as recent as the Early Triassic (Song et al., 2013; Xiao et al., 2010). Therefore, the BOC may hold important evidence for the last active stages of the CAOB and the corresponding closure of the Palaeo-Asian Ocean (Gillespie et al., 2017; Tian et al., 2015).

Problematically, the classification and naming of units within the BOC is inconsistent and non-systematic. The study area (Figure 2) previously has been regarded as a component of the Shuangyingshan-Huaniushan unit (Saktura et al., 2017; Ao et al., 2012; Xiao et al., 2010), the Shuangyingshan arc (He et al., 2018), the Huaniushan arc/unit (Zong et al., 2017; Zhang et al., 2015; Qu et al., 2011), the Dundunshan arc terrane (Cleven et al., 2016) and the Liuyuan microcontinent (Liu et al., 2011). This study uses the non-genetic Shuangyingshan-Huaniushan unit nomenclature, since its tectonic setting may be complicated and no substantive base presently exists for differentiating these two units.

Furthermore, the most recent comprehensive review of the BOC by Xiao et al. (2010) does not separate several sedimentary and metamorphic rock units. Ages for these units range from the Proterozoic to Mesozoic. Xiao et al. (2010) does not specify the tectonic setting of any of these units, or the reason why these units are considered separate arcs. Together with the classification issues, this highlights the highly specialised nature of most studies within the BOC and stresses the need for further research into the BOC's regional geology. This complicates reviewing the regional geology.

The Shuangyingshan-Huaniushan unit lies between two laterally continuous ophiolitic melanges, the Liuyuan ophiolite to the south and the Hongliuhe-Xichangjing ophiolite to the north (Zong et al., 2017; Cleven et al., 2016), which separate the Shuangyingshan-Huaniushan unit from other arc terranes. The Liuyuan ophiolitic melange has been interpreted by some as a rifting basin (Wang et al., 2017), but likely represents closure of a Permian oceanic basin (Mao, Xiao, Windley et al., 2012). A gabbro was dated at 286 ± 2 Ma (Mao, Xiao, Windley et al., 2012). The Hongliuhe-Xichangjing ophiolite was obducted during the Devonian or earlier (Cleven et al., 2015): a gabbro

was dated at 520.3 ± 5.8 Ma and a granite, which intrudes nearshore sediments deposited on top of the ophiolite's protolith, was dated at 413.6 ± 3.5 Ma, both using SHRIMP U-Pb on zircon.

The Shuangyingshan-Huaniushan unit's basement comprises the metamorphic belt that hosts the eclogites. It is composed of Proterozoic – early Palaeozoic clastic and calcareous meta-sedimentary rocks as well as orthogneisses (Saktura et al., 2017; Xiao et al., 2010). This basement was intruded by various Palaeozoic (arc) granitoids, including the Huaniushan arc (Xiao et al., 2010). The extensive Palaeozoic clastic and calcareous sedimentary rocks present in the unit would be attributable to basins related to these arcs, and consequently represent passive margins, fore-arc or back-arc basins (Cleven et al., 2018; Ao et al., 2012). Permian volcanics and sediments represent the youngest stratigraphic unit (Tian et al., 2015), whereas younger Triassic granitoids appear to mark the last stages of orogenic activity (Li et al., 2012).

Some have considered the belt and other Neoproterozoic terranes within the CAOB as microcontinents that once formed one single continent (He et al., 2018). Others have interpreted the belt's protolith as a large Neoproterozoic arc that continues into the Tianshan, related to the assembly of Rodinia (Zong et al., 2017). However, these interpretations are contentious at present and require further work to establish more reliable lithostratigraphic correlations.

2.3 Geology of the Gubaoquan area

The Gubaoquan (GBQ) eclogite is situated in the southernmost part of the Shuangyingshan-Huaniushan unit (Figure 2). It currently is the only documented eclogite body within the BOC and was first discovered by Mei et al. (1999). The most extensively studied eclogite body, measuring 400-by-50 m in size, is situated in one of the most accessible valleys in this area (Figure 3). Several authors (Soldner, Štípská et al., 2020; Soldner, Yuan et al., 2020; Liu et al., 2011) documented many smaller eclogite bodies occurring along strike of the original one.

Soldner, Štípská et al. (2020) were the first to describe the eclogite's structures and compare these with those of the country rock. The country rock displays a steeply dipping, N-S-trending fabric (their S2), that was folded by upright to steeply-inclined folds (their F3) and was largely

overprinted and transposed parallel to a steeply dipping, E-W-trending fabric (their S3). The less retrogressed parts of eclogitic boudins usually are largely isotropic, whilst the amphibolitised parts commonly had a strong fabric (their F3). However, these interpretations are based on observations from a very small area, which may not have preserved the full structural history.

Both Qu et al. (2011) and Soldner, Štípská et al. (2020) provide broadly comparable overviews of the eclogite's peak metamorphic and multiple retrograde assemblages, except that the latter's peak PT estimates are slightly higher. After peak metamorphism, the eclogite would have undergone a large decrease in pressure and small decrease in temperature. Upon reaching higher amphibolite-facies conditions, decompression would have been associated with more cooling. Soldner, Štípská et al. (2020) also observed andalusite, which they thought related to a Buchan-style metamorphism associated with the Ordovician-Silurian granitoids.

Extensive geochronological (Lu-Hf, Sm-Nd, zircon and monazite U-Pb, Biotite Ar-Ar) constraints have been provided for the eclogite and its host. In the latest studies (Saktura et al., 2017; Soldner, Štípská et al., 2020; Soldner, Yuan et al., 2020) these were contextualised through *in-situ* dating or with trace element geochemistry. However, all samples were collected in the close vicinity of the eclogite. Overall, these ages indicate that most of the protoliths of the rocks in the area were emplaced or deposited during the Meso- and Neoproterozoic. A metamorphic event may have occurred during the late Neoproterozoic.

Two major suites of granitoid intrusions occur in the area, which yielded Ordovician-Silurian (Saktura et al., 2017; Mao, Xiao, Fang et al., 2012; Liu et al., 2011) and Silurian-Devonian ages (Zhu et al., 2016). The Ordovician-Silurian intrusions have been interpreted as arc granitoids associated with the same subduction event responsible for eclogite-facies metamorphism (Saktura et al., 2017; Mao, Xiao, Fang et al., 2012; Liu et al., 2011) or as represent post-collisional granites (Soldner, Štípská et al., 2020 and references therein). The Silurian-Devonian intrusions have been interpreted as arc granitoids (Zhu et al., 2016). None of these studies discuss that these interpretations imply the presence of a cryptic suture between the rocks hosting the eclogite, which comprise the lower plate, and the granitoids, which would be emplaced into the upper plate. A

thorough petrogenetic study has not yet been performed on any of these intrusions and the relationship between local magmatism and deformation presently is not well understood.

The eclogite's whole rock geochemistry shows a MORB-like signature, specifically fractionated N-MORB (Saktura et al., 2017). These authors also argue that earlier data from Qu et al. (2011) should be used with caution, as the increased LOI and SiO_2 percentages in much of their data indicate significant metasomatism. Consequently, this may also affect the reliability of Qu et al.'s (2011) whole rock Sm-Nd and εNd results, as neodymium is known to be easily mobilised (Zachariah et al., 1995). Soldner, Yuan et al. (2020) used trace element data, whole-rock εNd and zircon εHf to suggest that the eclogite's protolith was a back-arc basalt at a stretched continental margin.

In terms of interpretations, the earliest studies classified the Gubaoquan eclogite as an oceanic eclogite (Qu et al., 2011; Liu et al., 2011; Mei et al., 1999). However, their conclusion is mainly based on geochemistry, whereas field observations to support such a claim are scarce. Saktura et al. (2017) argued that the field relations and (near-)isothermal decompression are usually associated with continental eclogites. Soldner, Yuan et al. (2020) argued that the metamorphic tectonites represent a Grenvillian arc terrane. Their subsequent publication (Soldner, Štípská et al., 2020) suggests that the eclogite originated in the lower crust and was juxtaposed to the present country rock at mid-crustal levels during their D2, upon which further uplift occurred during upright folding associated with their D3.

Lastly, the earlier studies (Qu et al., 2011; Liu et al., 2011; Saktura et al., 2017) inferred that the ocean basins associated with the Gubaoquan eclogite's and the Liuyuan ophiolite's formation were one and the same. However, the intrusive age of a gabbro in the Liuyuan ophiolite is Permian, substantially younger than the protolith ages of the eclogite (Mao, Xiao, Windley et al., 2012).

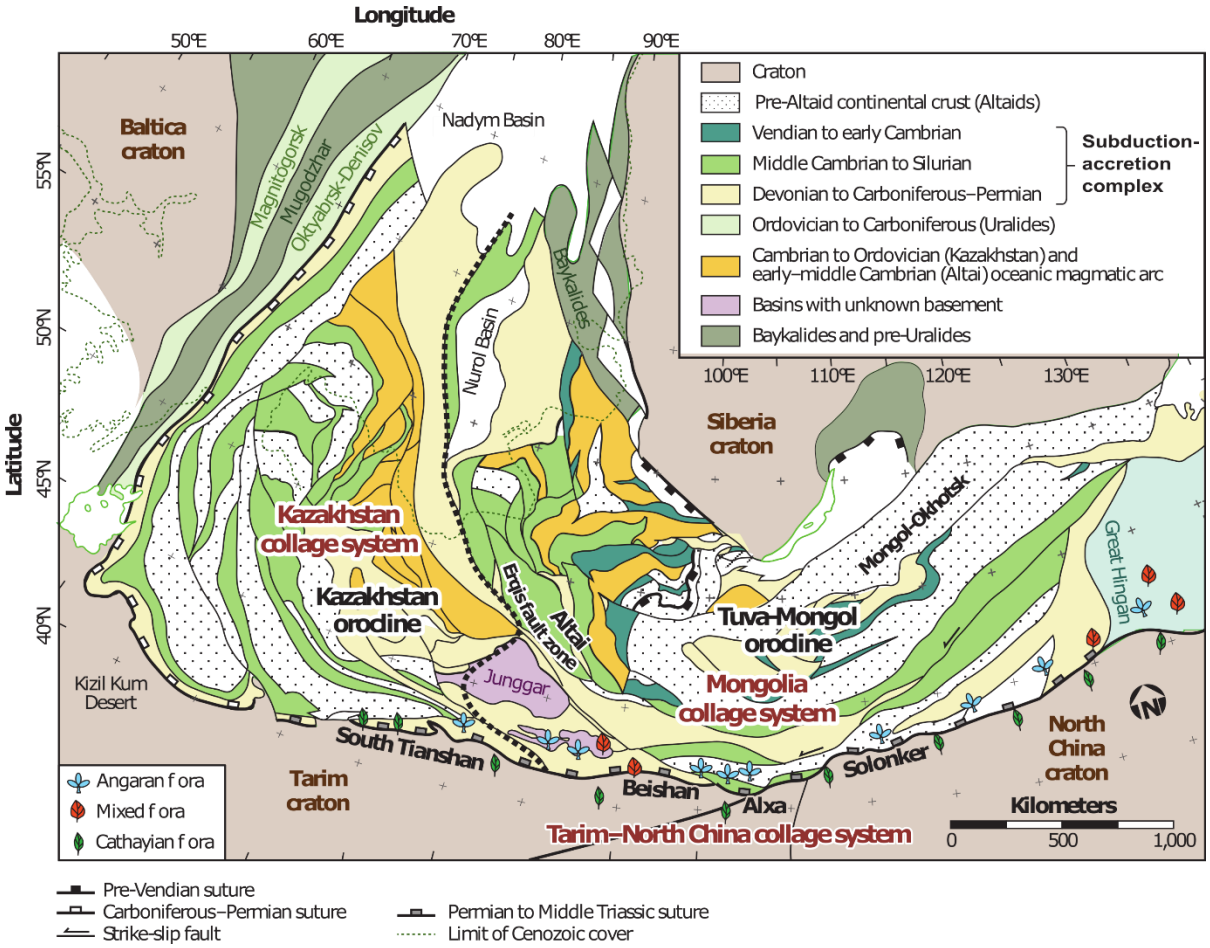

Figure 1. Generalised geology of the Central Asian Orogenic Belt (modified after Xiao et al., 2015).

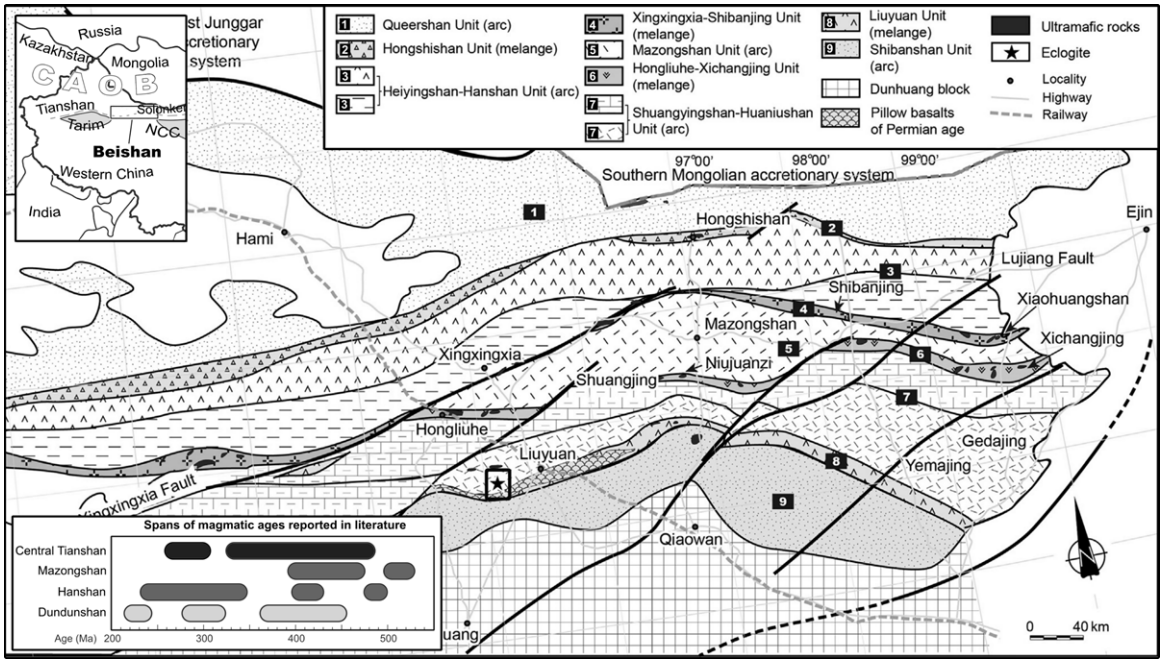

Figure 2. Overview map of the Beishan Orogenic Collage (modified after Cleven et al., 2016; Xiao et al., 2014; Mao, Xiao, Windley et al., 2012). The small black box outlines this study's mapping area. Upper left inset shows approximate geographic location, lower right inset shows a summary of the main igneous phases in the BOC.

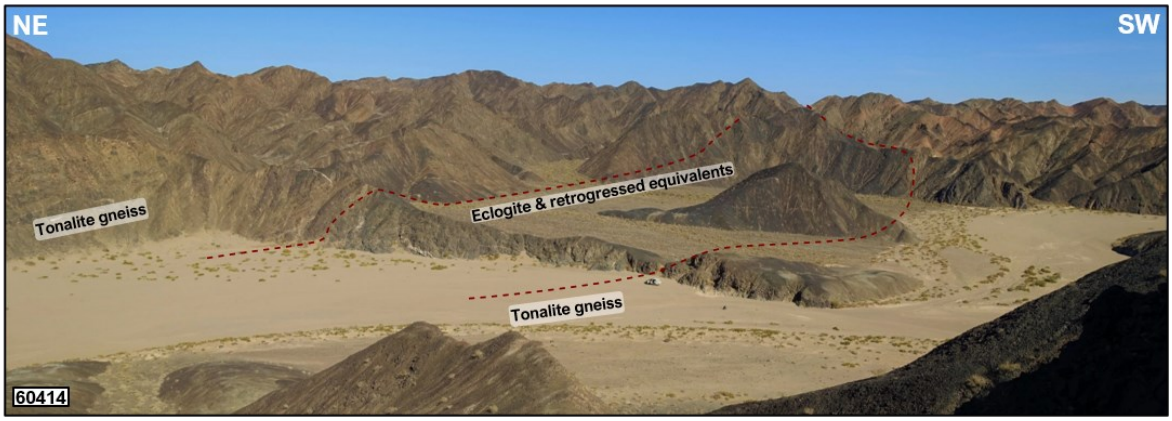

Figure 3. Overview of the largest outcrop of the Gubaoquan eclogite (60414).

Chapter 3
Methodology

Around a hundred days were spent in the field during two field seasons. The study area is located in the southern parts of the Beishan Orogenic Collage, immediately north of the Gubaoquan-Hongliuyuan fault (Figure 2) and covers about 300 km^2. Except for the China Geological Survey 1:50.000 maps (Gansu BGMR, 1966), essentially no detailed maps exist for the area. Approximately 2100 localities were visited in this area. The locations of samples mentioned in this thesis are listed in Appendix A.

Around 400 thin sections were made by the Hebei Geology and Mineral Resources Bureau Langfang Laboratory, providing a good coverage of all major rock types. These were all analysed by standard transmitted light microscopy.

The Beijing SHRIMP centre prepared all zircon mounts for geochronology. Zircons were mounted in epoxy, together with crystal fragments of the zircon standard Temora (Black et al., 2003). The mounts were ground down to expose the zircon.

Ablation spots were selected using transmitted light and CL images, which were taken by the Beijing SHRIMP centre as well. Preference was given to clear areas without cracks, inclusions or multiple zones, in order to minimise discordance. This may introduce a slight bias towards younger zircons, particularly for igneous cores in metamorphic zircons, as younger zircon generally is of better quality.

Select samples were analysed using a SHRIMP II ion microprobe at the Beijing SHRIMP centre, Chinese Academy of Geological Sciences. The analytical procedure is described in Kröner et al. (2012) and references therein. Temora (416.8 ± 1.1 Ma; Black et al., 2003) was used as the primary standard. As the metamorphic rims tended to be very thin, for all samples a beam size of 13 μm was used for both the rims and cores, except for 63905B, for which 24 μm sufficed. Discordance was calculated as $|(^{206}Pb/^{238}U \text{ age} / ^{206}Pb/^{207}Pb \text{ age} - 1)| * 100$. Data was plotted using Isoplot/Ex 3.75 (Ludwig, 2012).

Several geochemical samples of metamorphic and igneous rocks were also collected during the field work. These are not part of this thesis and are included in Appendix D.

Chapter 4
Lithostratigraphic architecture

The mapping area, which measures 300 km^2 and was mapped as part of this thesis, covers a broad area of the metamorphic tectonite belt, several granitoids and mafic intrusions. This map is included as the supplementary file Gubaoquan_map.pdf, which the reader is encouraged to refer to. Two accompanying cross-sections are presented in Appendix B. A smaller close-up map shows the immediate surroundings of the eclogite (Figure 4). Part A'-A'' of cross-section A-A'', which illustrates the local folding pattern, is presented in Figure 5. Its trace is marked in Figure 4. The larger map and cross-sections are summarised in Figures 7-8.

The area can be divided into five different lithological panels: a Proterozoic belt of highly deformed metamorphic tectonites; locally deformed Ordovician-Silurian granitoids; undeformed Silurian-Devonian intrusions; a cover comprised of Carboniferous rhyolites and conglomerates; and lastly, various Permian-Triassic intrusions (Figure 7). The latter two are too small to feature on the map. In the following section, each panel is described by age, from oldest to youngest.

4.1 Metamorphic tectonites

The metamorphic tectonites consist of intercalated layers and lenses of felsic and mafic meta-igneous and metasedimentary units. These units are not uniformly distributed and nine lithological domains labelled A-B-C-D-E-F-G-H-I were identified (Figure 7), based on the relative quantity of felsic orthogneiss or metasedimentary rocks and metabasites. The eclogite only occurs in domain I. The units will be discussed from oldest to youngest, based on cross-cutting relationships: metasedimentary rocks, mafic schist, felsic orthogneiss and eclogite.

4.1.1 *Metasedimentary rocks*

These units have been subdivided based on their composition: the area is too deformed to reconstruct their internal stratigraphy. The siliciclastic rock units are discussed on basis of grain

size: (I) metaconglomerate, (II) quartzite, (III) quartz-rich schist and (IV) mica schist. Lastly, (V) the marble will be described.

(I) The metaconglomerate has a light grey to light brown colour and is composed of variable quantities of ≤3 cm mafic, calcite, feldspar, quartz or leucogranitic clasts, usually in a strongly foliated to mylonitic micaceous matrix (Figure 9A). This unit is rarely exposed and its description is based on a small number of outcrops, predominantly in the very north of the mapping area.

(II) The quartzite is white to light grey and massive to poorly foliated (Figure 9B). It usually contains nearly exclusively quartz, with only a small amount of brown or white mica. The quartz commonly has completely recrystallised, but inherited, coarse grain shapes can be discerned in some cases. Towards the east of the mapping area, several <100 m thick layers of quartzite are intercalated with metamafic layers.

(III) The quartz schist is light grey to light brown. Most occurrences are medium- to coarse-grained meta-lithic and meta-sublithic arenites (Figure 9C). Occasionally, the unit is intercalated with fine layers of mica schist. It usually bears a cm-spaced pervasive foliation but lacks foliation in more quartzose occurrences. It frequently contains mm-scale garnets.

(IV) The mica schist is dark brown to grey-black and relatively coarse (Figure 9D). It predominantly consists of micas and quartz but may contain ≤2 cm-long kyanite or ≤5 mm-sized garnet. The unit may contain abundant quartz veins.

(V) The marbles are less common and are creamy white, light ochre or grey (Figure 9E). The unit ranges from nearly pure marble to calc-arenite in composition. They are pervasively foliated, sometimes intensely sheared and tend to occur near major structural-lithological domain boundaries (Figure 4).

There are some areas where the sedimentary units are interlayered on metre-scales, but more commonly one single unit is found across a larger area. Based on intrusive and crosscutting relationships (Figures 10A-C; 11A), the metasedimentary units are interpreted as the oldest rocks.

Two metagreywacke samples were dated by Soldner, Yuan et al. (2020) and Soldner, Štípská et al. (2020) using U-Pb LA-ICPMS on zircon and monazite. The first sample yielded a single age at 845.6 ± 6.9 Ma, interpreted as a metamorphic event. The second one was discordant

with intercepts at 750 ± 34 Ma and 1461 ± 44 ma, with the former age interpreted as a metamorphic age, the latter as an inherited age. The monazite dating yielded ages of 445-440 Ma (cores) and 436-429 Ma (rims), which were interpreted as syn-D2 and -D3, respectively (Soldner, Štípská et al., 2020). All samples, however, were sampled close to the eclogite, and may not necessarily reflect the age of other domains.

4.1.2 *Metabasites and associated metagranitoids*

The metabasites are rather uniform and generally have a black-grey colour. The unit can be very coarse- (≤1 cm) or fine-grained (≥1 mm), but usually has subequigranular 2-3 mm-long crystals. It primarily consists of dark brown to blue-green amphibole, sometimes with clinopyroxene or plagioclase needles. Commonly, the unit appears to be a hornblendite but generally is found to contain ≥10% (partially sericitised) plagioclase at closer inspection. It frequently contains garnet. The unit appears to have (mela)gabbroic, (mela)dioritic or basaltic protoliths.

The metabasites usually form continuous, hundred-metre-thick packages, whilst in other instances, these can form metre-thick lenses within the metasedimentary rocks (Figure 4). This suggests that the protoliths of the metasedimentary rocks were intruded by mafic dykes or sills, which together with their host were metamorphosed to (garnet) amphibolites (Figure 10A-C).
The unit commonly is associated with significant bodies of meta-trondhjemite and -tonalite (Figure 4). These are never megacrystic and usually do not show augen textures, in contrast to the felsic augen gneisses described below.

Soldner, Yuan et al. (2020) obtained a lower age cluster of 910.9 ± 3.0 Ma and an upper one of 1378 ± 15 Ma for an amphibolite adjacent to the eclogite (LA-ICPMS U-Pb on zircon). There is a possibility that the metabasites are composed of several suites of protoliths.

4.1.3 *Felsic Orthogneiss*

The felsic orthogneiss can be differentiated into two units, based on their composition and dominant colour: a pink gneiss and a grey gneiss (Figure 4). The grey gneiss is white to light grey,

with some minor, pink-coloured areas due to potassic alteration. A yellow colour is common in lower-lying areas, most likely due to alteration as well. The unit had trondhjemitic, tonalitic, granodioritic or occasionally quartz-dioritic protoliths. It may contain ≤10 cm-long plagioclase augen (Figure 11A), whereas in other areas extensive shearing has completely recrystallised these or rocks bearing smaller augen into mylonites (Figure 11B). Interstitial areas primarily consist of quartz, plagioclase, biotite and hornblende. Regularly, these rocks also contain white mica, primarily in highly strained parts. Occasionally, the unit is garnetiferous.

The pink gneiss has a beige to pink colour. It has ≤10 cm-long plagioclase and/or K-feldspar augen in the least strained parts, whereas in others these augen are smaller and/or were extensively stretched. Large cm-sized quartz porphyroblasts are common, which occasionally enclose euhedral hornblende. The interstitial areas primarily consist of biotite with quartz and plagioclase. Occasionally, the unit is garnetiferous. Epidotisation and chloritisation are commonplace towards the south, whereas alteration to muscovite is frequently observed in highly strained areas. Most likely, this unit had a (leuco)granitic to granodioritic or occasionally alkali-feldspar-granitic protolith.

The felsic orthogneiss appears to intrude all the above units and therefore is younger (Figure 11A). In domain I, the felsic orthogneiss contains several lenses of metasedimentary and metabasic rocks, including the eclogite lenses. These may be parts of the country rock that were picked-up by the gneiss's protolith during its emplacement.

An igneous zircon age of 920 ± 14 Ma (SHRIMP U-Pb) was interpreted as the protolith's emplacement age (Saktura et al., 2017). This age was obtained from a tonalite gneiss immediately south of the eclogite. An age of 867.5 ± 1.9 Ma (LA-ICPMS U-Pb) was obtained at another orthogneiss, close to the eclogite (Soldner, Yuan et al., 2020). Ar-Ar dating on biotite from an adjacent orthogneiss yielded an age of 428.9 ± 3.8 Ma (Qu et al., 2011), which was interpreted to date the retrograde path of the rock.

4.1.4 *Eclogite*

The eclogite occurs as ≤500 m-sized mafic pods, of which the cores frequently display eclogite-facies textures. It has a green-red appearance in relatively fresh areas (Figure 12A) and is dark blue-black in more retrogressed sections (Figure 12C). Usually, the eclogite is rather coarse-grained (≤6 mm). The least retrogressed areas predominantly consist of diopside-albite symplectites, garnet and rutile, whereas the most retrogressed areas consist of hornblende, plagioclase, quartz, biotite, and preserve remnants of higher-grade assemblages. Most likely, the eclogite had a basaltic or gabbroic protolith.

The eclogite is hosted within domain I and consists of one major and several smaller variably retrogressed, foliation-parallel screens (Figure 4). The eclogite boudins are hosted by both felsic orthogneiss as well as metasediments (Figure 12B). Towards the west of the major lens, the eclogite and its enveloping host are truncated by a Silurian granitoid body. Towards the east, a trail of smaller lenses can be traced up to the southern boundary of the tectonite belt. Just north of the eclogites lies a domain dominated by metasedimentary rocks and amphibolites, with only a few orthogneiss lenses here.

Zircons (U-Pb LA-ICPMS) from the eclogite yielded 875-860 Ma for the cores and 465-460 Ma for the rims (Saktura et al., 2017; Soldner, Yuan et al., 2020; Qu et al., 2011). The former is interpreted as the emplacement age of the protolith, the latter as the metamorphic age. A ~462 Ma garnet Lu-Hf age was interpreted as dating garnet growth in the eclogite, a ~453 Ma garnet Sm-Nd age as peak metamorphism (Soldner, Štípská et al., 2020).

4.2 Ordovician-Silurian intrusions

This suite has been divided into four units. From oldest to youngest, based on crosscutting relationships, these are: (I) granodiorite to monzogranite; (II) leucocratic tonalite to syenogranite; (III) trondhjemite to leucogranite; (IV) gabbro to diorite. A brief description of each is given below.

(I) The granodiorite to monzogranite is speckled black-white in appearance (Figure 13A). It varies in grain size, but generally is coarse and unequigranular. The unit frequently contains ≤1 cm zoned plagioclase phenocrysts. Hornblende, titanite and biotite are the dominant mafic phases.

This unit also has some minor tonalitic sections, which appear to have a gradational contact with the rest of the unit.

(II) The leucocratic tonalite to syenogranite is light pink to white, medium-grained (≤4 mm) and unequigranular. Hornblende, biotite and titanite are the dominant mafic phases. The unit occasionally contains muscovite. Frequently, mafic-intermediate enclaves with gabbroic to dioritic compositions are present. Generally, this unit has a monzogranitic or granodioritic composition, with some minor tonalitic, monzogranitic or syenogranitic areas. These appear to have gradational contacts and were not differentiable at this scale. Many of these occurrences are associated with D6 faults described below – potentially, these are the result of alteration. This unit crosscuts unit I.

(III) The trondhjemite to leucogranite is white to light pink, is coarse-grained and occasionally pegmatitic. Dykes of this unit are very common throughout the area but are too small to display at this scale. These dykes cross-cut unit II. Larger outcrops are commonly associated with D3-D4 fault/shear zones described below.

(IV) The gabbro to diorite has a dark blue grey colour, is coarse-grained and has an ophitic texture. It usually intrudes as a composite dyke along with rocks of unit II and has xenoliths of said unit. Elsewhere, it intrudes as a composite dyke with rocks of unit III, which it also crosscuts.
These units occur as two major and several smaller intrusions (Figure 7). Many of these intrusions are lenticular and are oriented parallel to the structural grain of the mountain belt. The major intrusion in the south primarily consists of unit II whilst the one in the north consists of both unit I and II. Both intrusions also bear abundant composite mafic-felsic dykes of units III and IV (Figure 13A).

The southern intrusion was dated at 442 ± 4 Ma with zircon U-Pb (Mao, 2008), whilst the northern one has ages of 442 ± 3 Ma (Mao, 2008) and 424 ± 3 Ma (SIMS U-Pb) (Mao, Xiao, Fang et al., 2012). A trondhjemite dyke that crosscuts the eclogite was dated at 424 ± 8.6 Ma (SHRIMP U-Pb) (Saktura et al., 2017). However, Mao (2008) is an unpublished PhD thesis; their ages could not be critically assessed.

4.3 Silurian-Devonian intrusions

The north of the mapping area is bounded by a major batholith that consists of three different units. From oldest to youngest, based on crosscutting relationships, these are: (I) megacrystic monzogranite, (II) leucosyenogranite to leuco-alkali-feldspar-granite and (III) leucogranodiorite to trondhjemite.

(I) The megacrystic monzogranite has <5 cm alkali feldspar megacrysts (Figure 4). It is light pink and unequigranular. Biotite, which occasionally is chloritised, and hornblende are the primary mafic phases. Megacrystic concentrations vary: certain areas are nearly devoid of any megacrysts, whereas others have cumulate textures (Figure 13B).

(II) This leucosyenogranite to leuco-alkali-feldspar-granite is light to dark pink, coarse-grained (4-7 mm) and variably subequigranular to unequigranular. Generally, this unit is highly leucocratic, but it occasionally contains (chloritised) muscovite or biotite. A sharp contact exists between the leucosyenogranite and leuco-alkali-feldspar-granite, but these are undifferentiable at this scale. The syenogranite includes xenoliths of the leuco-alkali-feldspar -granite, indicating it is younger. This unit intrudes the megacrystic granite.

(III) This leucogranodiorite to trondhjemite is pink-grey in appearance, medium-grained (≤4 mm) and subequigranular. Usually, this unit has a leucogranodioritic composition, but it occasionally grades into trondhjemite. It variably contains hornblende and/or biotite as mafic phases. The biotite has commonly been subjected to chloritisation, whilst the feldspars have variably been sericitised. This unit intrudes unit I & II.

These intrusions form the northern boundary of the mapping area. Unit I is the most extensive, whereas units II and III consist of several smaller bodies, which occur immediately south of the megacrystic granite. Unit I was dated at 404.4 ± 1.8 Ma, whilst unit II was dated at 418.5 ± 4.4 Ma (zircon LA-ICPMS U-Pb) (Zhu et al., 2016). This contradicts with the observed cross-cutting relationships and should be further assessed through additional geochronology.

Towards the south of these intrusions, several mafic-felsic (sub-)volcanic units occur. This area is marked as Devonian on Chinese survey maps (Gansu BGMR, 1966), but otherwise no written works exists concerning these units. The difference in intrusive depths between these units

and the granitoid complicates interpreting them as coeval; instead, they may have an age comparable to the Permian (sub-)volcanic units found elsewhere (Li, 2019).

4.4 Permian basal conglomerates and flow-banded rhyolites

In an area too small to feature on the maps, undeformed conglomerates are intruded by rhyolites (Figure 13C). The conglomerate is light grey to white and consists of poorly sorted, sub-angular clasts with a grain size of ≤1 cm. The unit is not bedded or foliated. Clast compositions include pure quartz, pure feldspar, gneiss, dolerite and granite (Figure 13D). Unfortunately, the contact appears to have been structurally modified, but most likely these represent basal conglomerates.

The rhyolite includes several suites. It is deep pink, light pink or light green in colour. The unit is aphanitic and bears minimal mafic minerals. It may contain biotite, quartz, (epidotised) plagioclase and/or pyrite phenocrysts. The phenocrysts commonly are ≤3 mm but occasionally measure up to 1 cm. The unit frequently has spherulitic textures (≤1 cm) and/or flow banding. The flow bands are internally folded into an irregular geometry, suggesting these are igneous flow textures. Apart from its co-occurrence with the conglomerate, this unit is found throughout the mapping area and abuts several units, including the Devonian megacrystic granite. It is offset by D6 faults described below, suggesting these faults are younger.

This conglomerate has not been described before in the mapping area but may be correlatable to Carboniferous-Permian sedimentary units that non-conformably overlie the gneisses towards the east (Li, 2019). Li (2019) also describes several similarly aged (282.2 ± 2.1 Ma; zircon SHRIMP U-Pb) rhyolites in the north-east. However, as there are several suites of rhyolite, this age may not be fully representative.

4.5 Permian-Triassic units

Several younger igneous units occur throughout the area. They include several mafic to felsic intrusions, which variably intrude as lenticular intrusions or dykes. As these are not relevant

to this thesis, they are not described in detail here. Descriptions of these units are given on the large map (Appendix B).

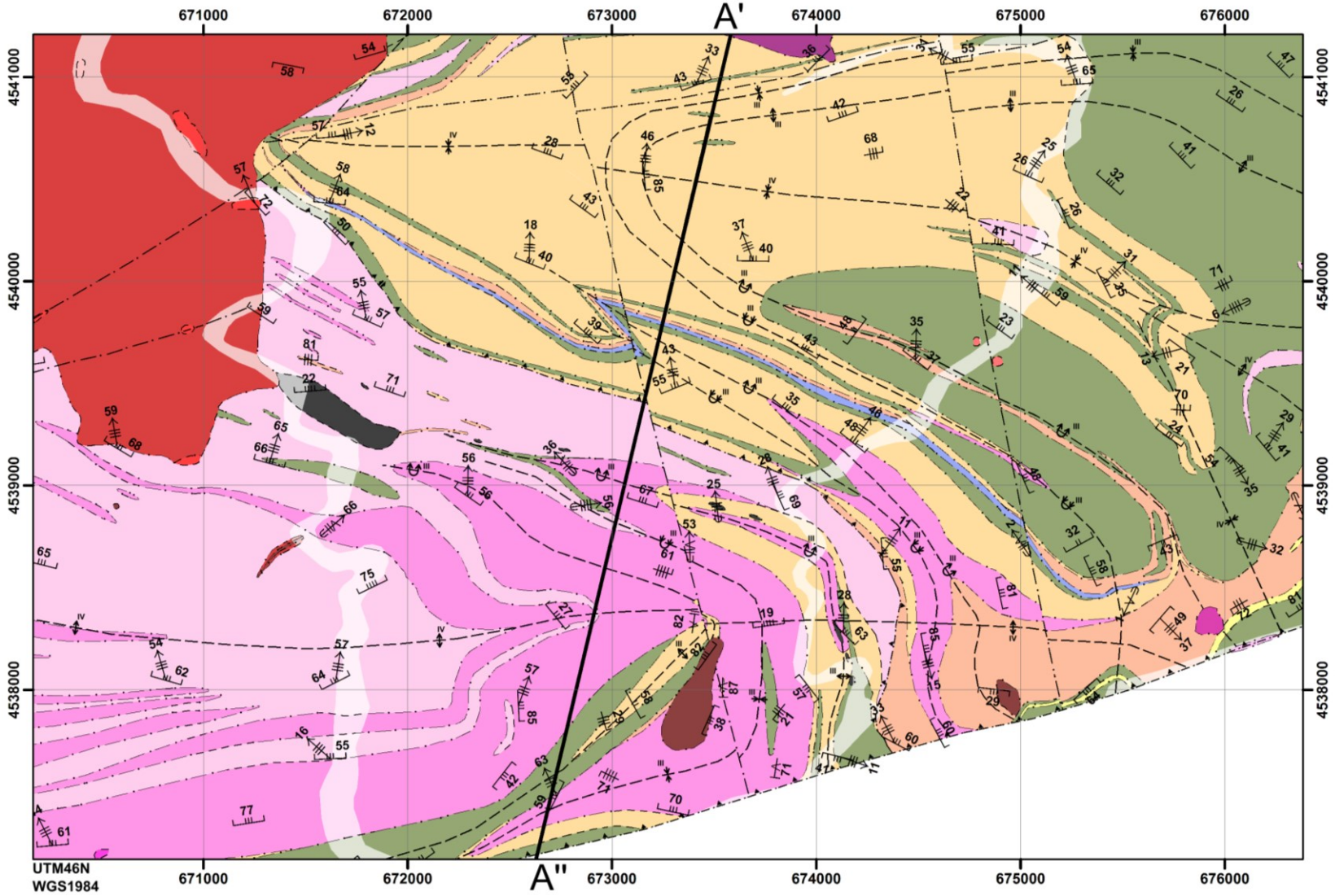

Figure 4. Close-up map of the area surrounding the Gubaoquan eclogite. A representative selection of structural data is shown. The associated legend is shown as **Figure 6**.

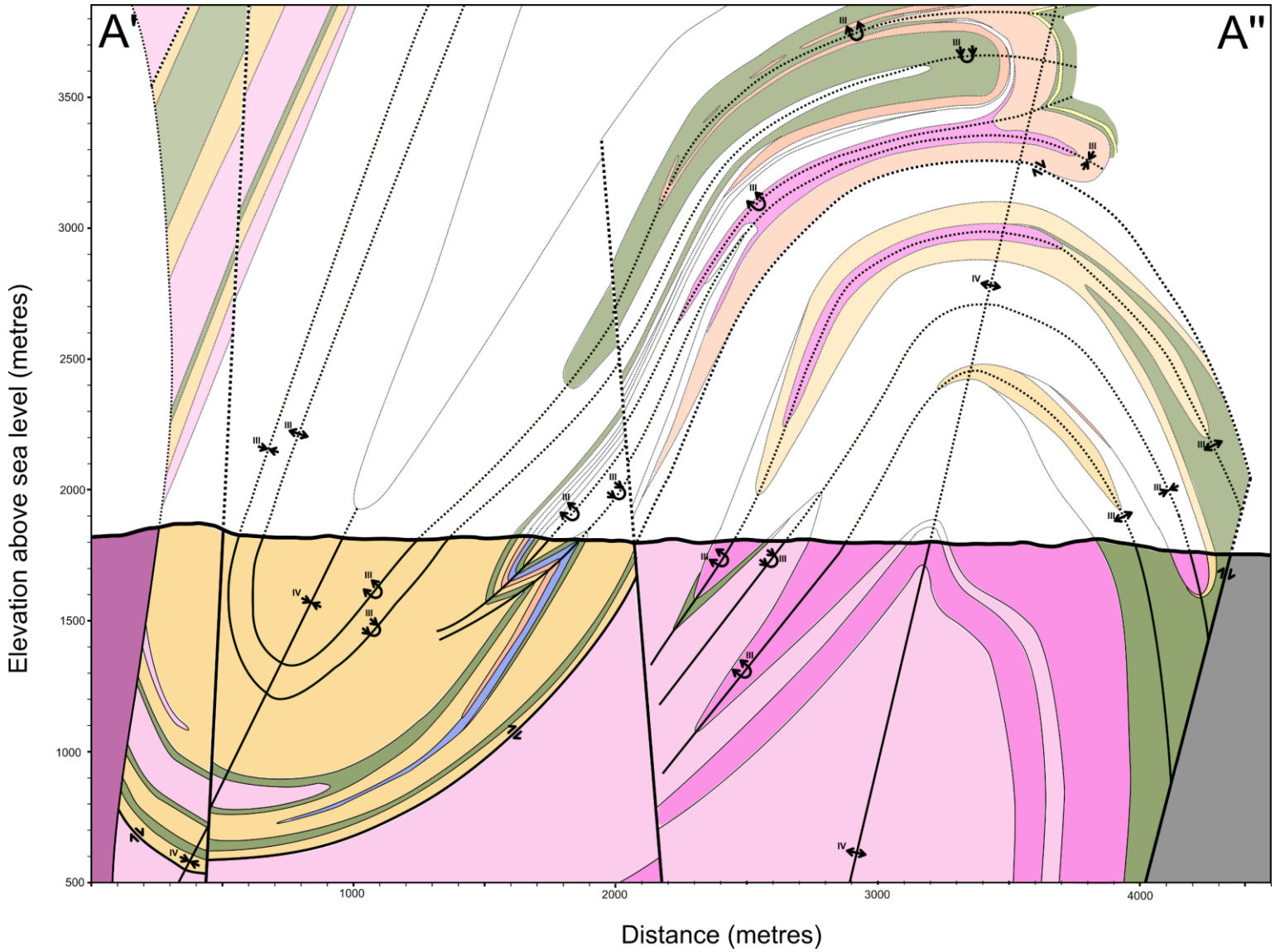

Figure 5. Cross-section along transect A'-A'', as marked in **Figure 5**. The associated legend is shown as **Figure 6**.

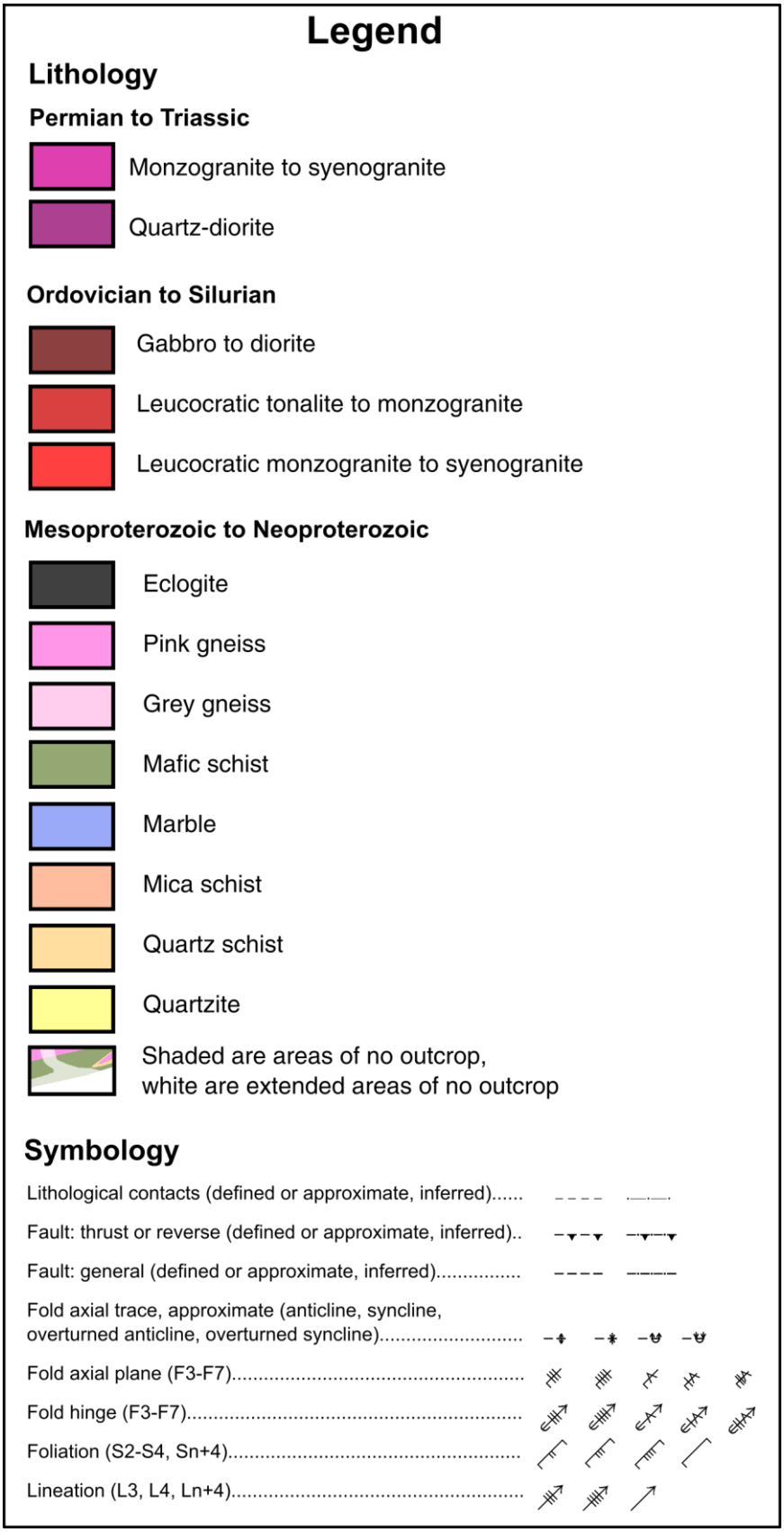

Figure 6. Legend for **Figures 4-5**.

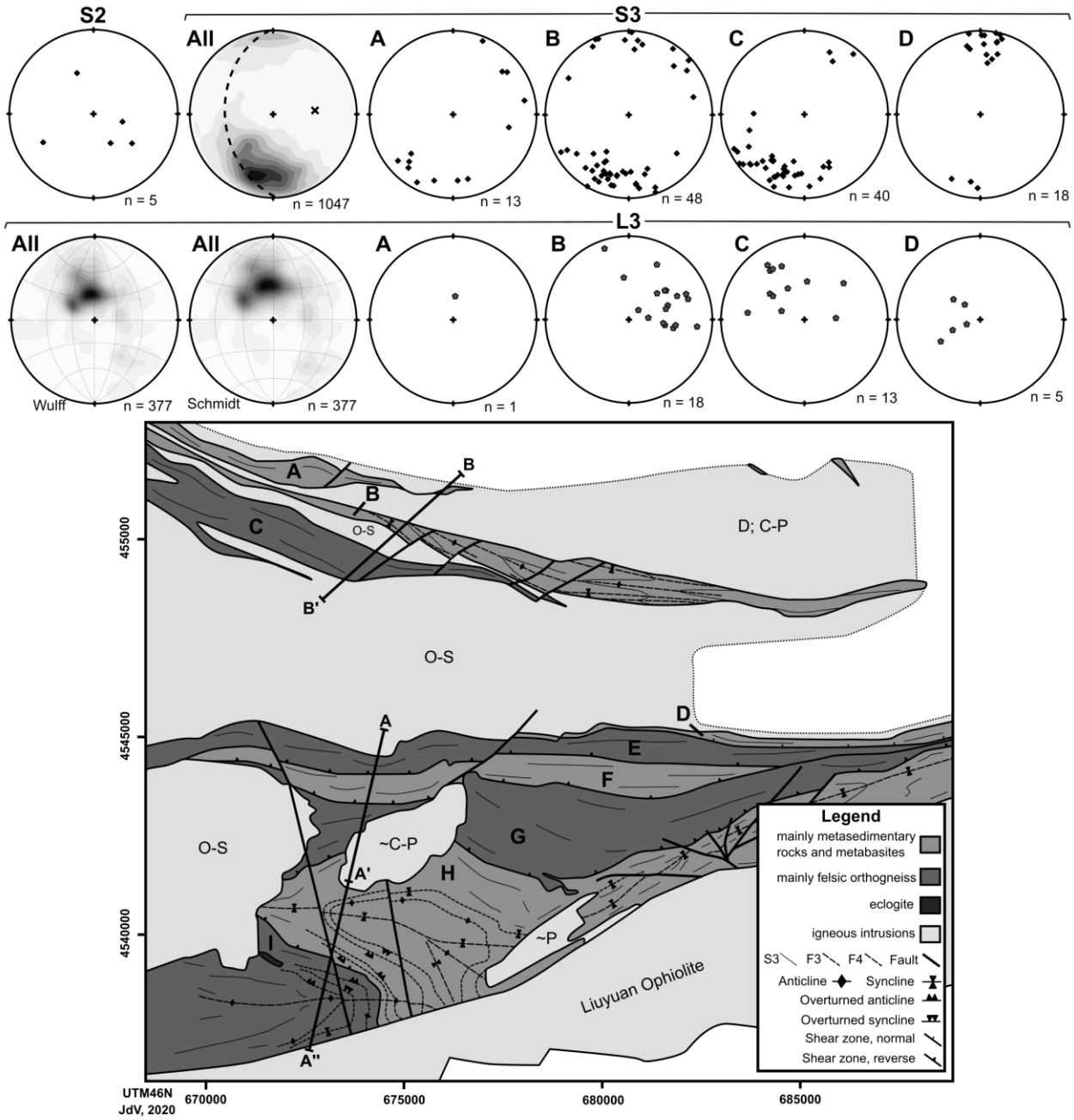
S2
S3
All
A
B
C
D
n = 5
n = 1047
n = 13
n = 48
n = 40
n = 18
L3
All
All
A
B
C
D
Wulff
n = 377
Schmidt
n = 377
n = 1
n = 18
n = 13
n = 5
A
B
B'
C
O-S
D; C-P
O-S
A
D
E
F
G
H
I
A'
A''
O-S
~C-P
~P
Liuyuan Ophiolite
Legend
mainly metasedimentary rocks and metabasites
mainly felsic orthogneiss
eclogite
igneous intrusions
S3
F3
F4
Fault
Anticline
Syncline
Overturned anticline
Overturned syncline
Shear zone, normal
Shear zone, reverse
455000
4545000
4540000
UTM46N
JdV, 2020
670000
675000
680000
685000
S3
S4+n
E
F
G
H
I
n = 62
n = 66
n = 100
n = 431
n = 269
Pτ n = 11
D n = 1
OS n = 87
L3
L4+n
E
F
G
H
I
n = 24
n = 29
n = 57
n = 92
n = 138
Pτ n = 5
D n = 1
OS n = 20

Figure 7, previous page. Simplified map of the mapping area and stereonets of foliations and lineations. The map marks the different domains and shows the two cross-section traces. For the intrusions, the letters denote their emplacement age. The stereonets plot D2, D3 and D4+n foliations and lineations. Foliations are plotted as poles to planes. For D3, separate stereonets for each domain are included. All data are plotted on Schmidt stereonets, whereas L3-all is plotted on both Wulff and Schmidt stereonets, to highlight its distribution girdle. In S3-all, a best-fit girdle and pole are given as well. For D4+n, different shadings are used for each intrusive suite.

Folds and crenulation cleavages

Planar features

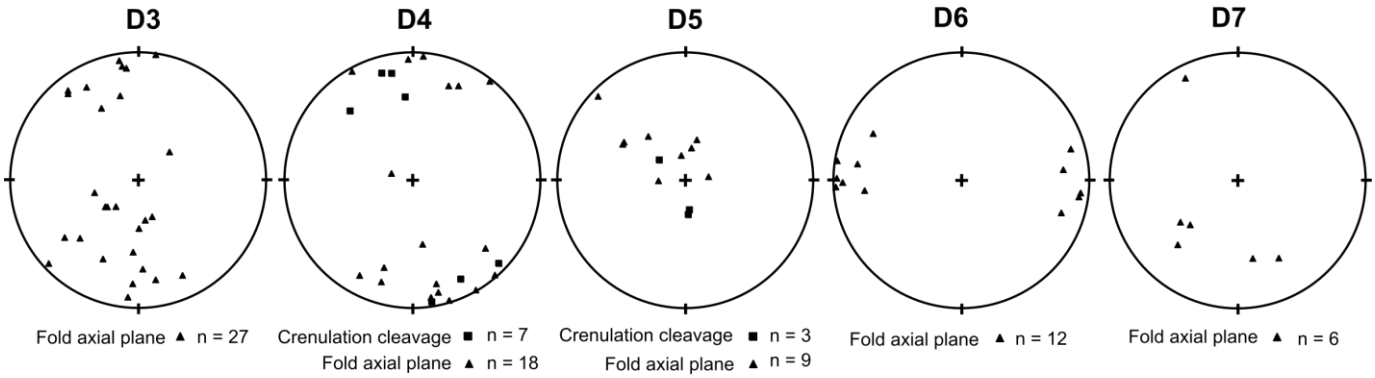

Linear features

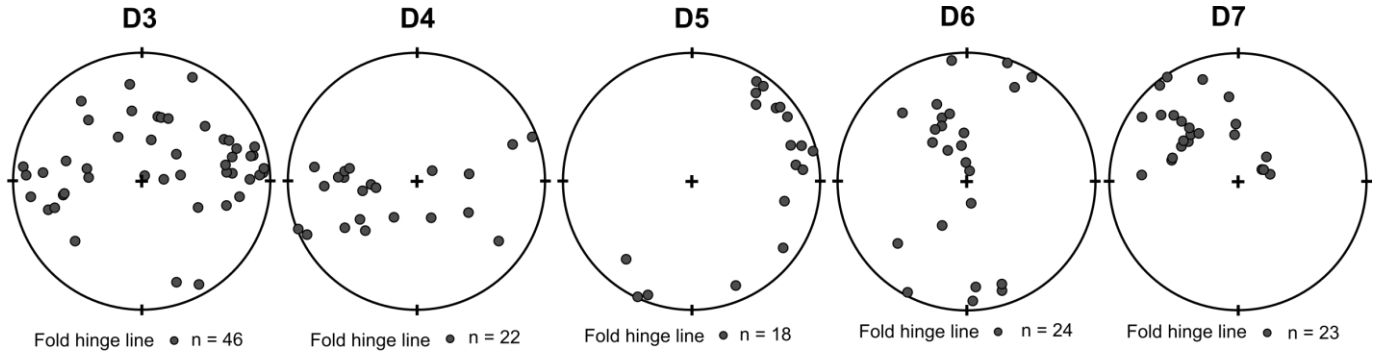

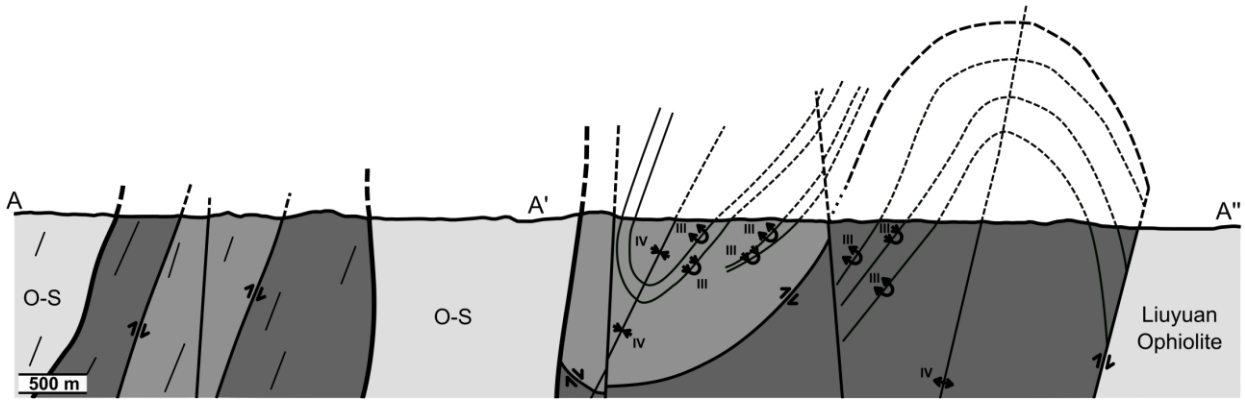

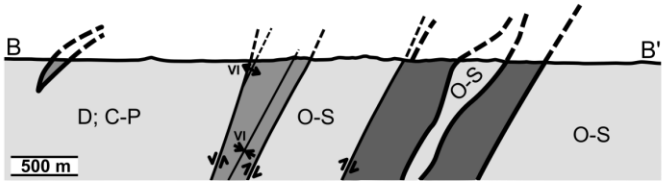

D3 - shearing directions

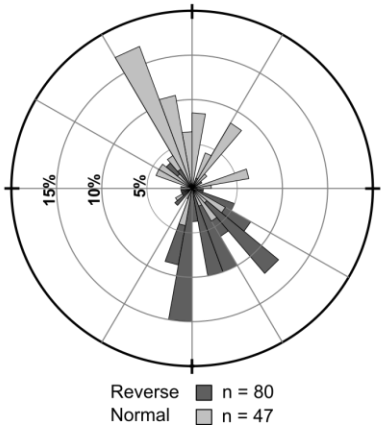

Figure 8, previous page. Stereonets of folds and crenulation cleavages, simplified cross-sections and rose diagram of shearing indicators. Planes are plotted as poles to planes. Part A'-A" in cross-section A-A" corresponds to **Figure 5**. The rose diagram shows the orientation of the shearing direction of the hanging wall.

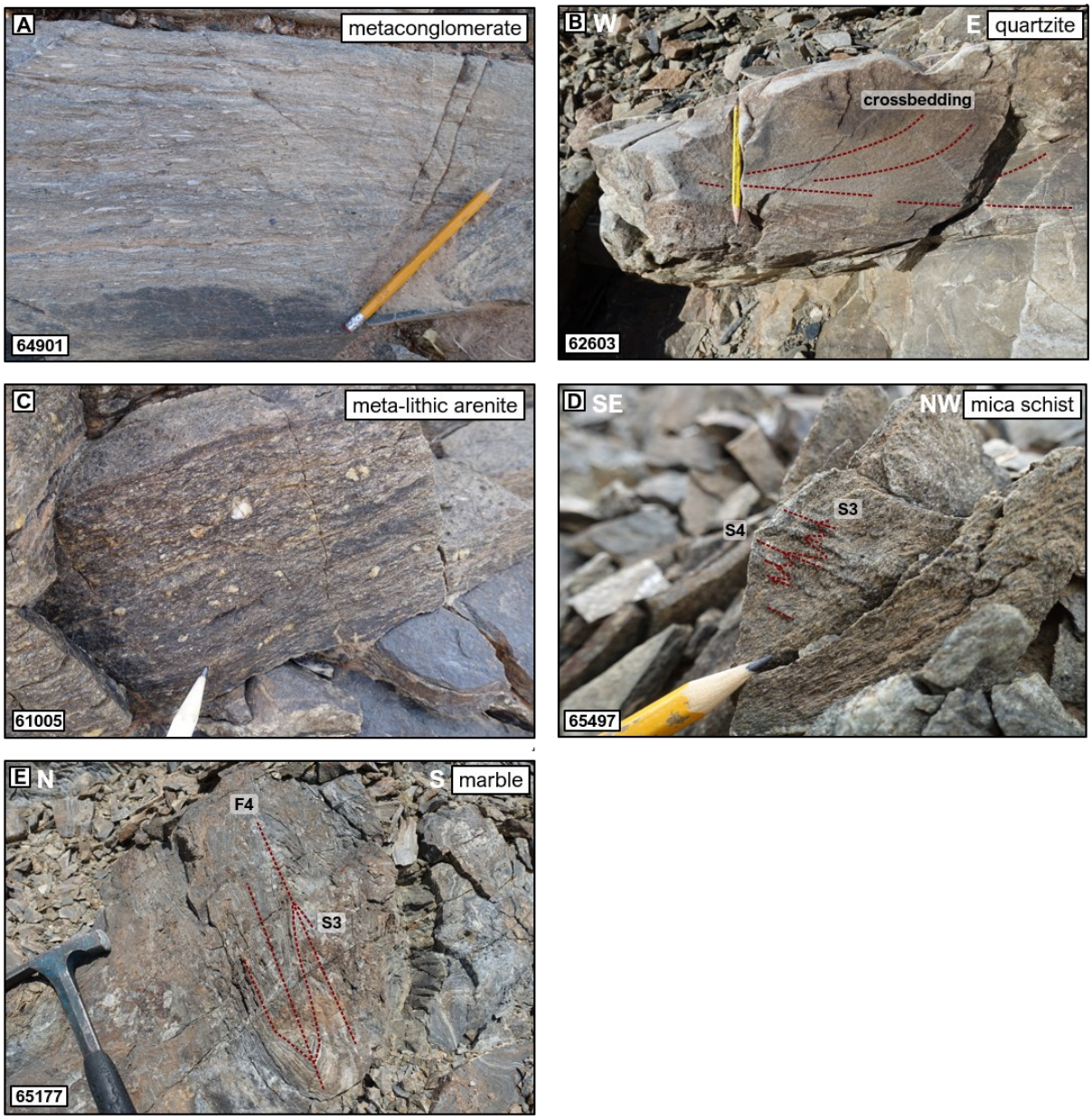

Figure 9. Illustrative photographs for the metasedimentary rocks in the metamorphic tectonite belt. (A) Metaconglomerate (64901). (B) Meta-lithic arenite, illustrative for many of the area's quartz schists (61005). (C) Quartzite with crossbedding preserved on surface perpendicular to S3 & L3 (62603). (D) Mica schist with D4 crenulations (65497). (E) Extensively deformed marble, illustrative for the strain localisation in calciferous units (65177).

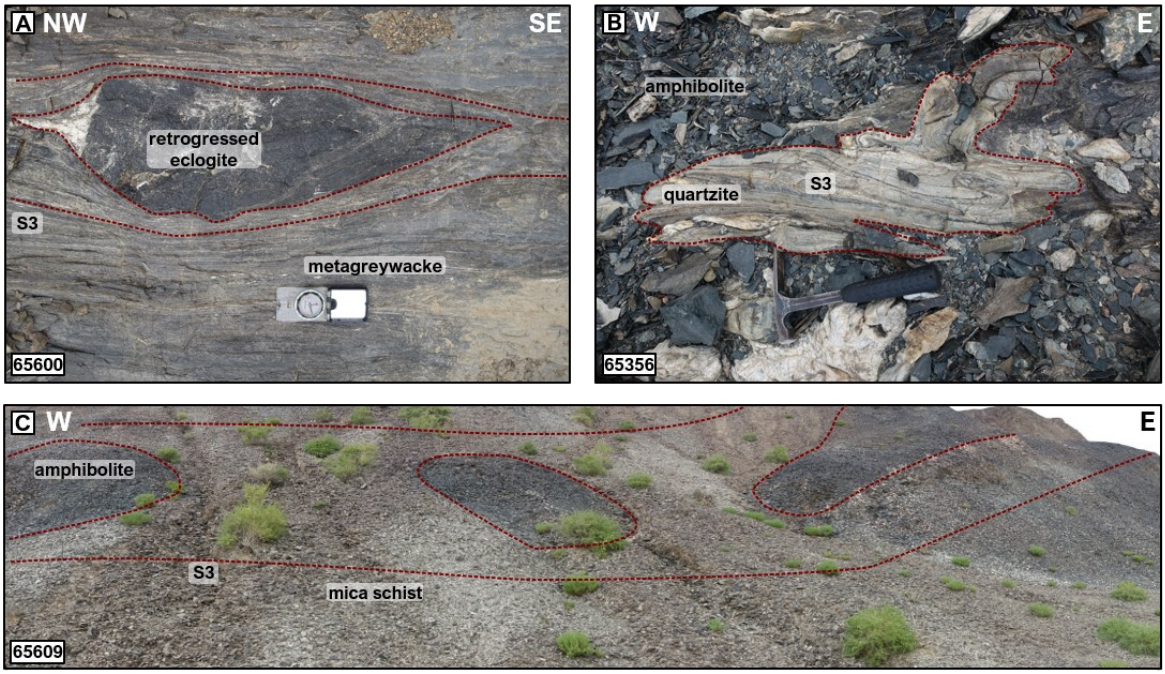

Figure 10. Illustrative photographs for the metabasic rocks in the metamorphic tectonite belt. (A) A lens of amphibolitised eclogite within mylonitic metagreywacke (65600). (B) Sliver of folded quartzite within amphibolite (65356). (C) Several boudins of amphibolite within mica schist (65609).

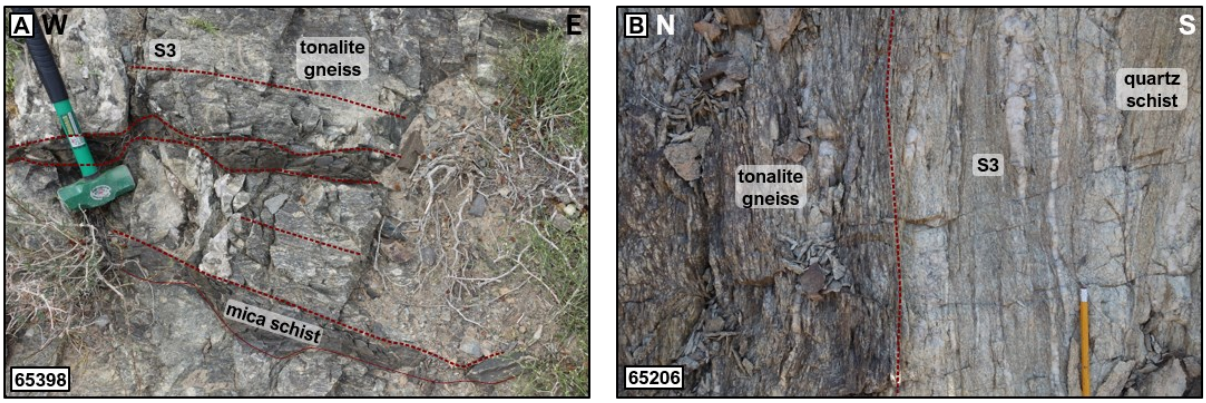

Figure 11. Illustrative photographs for the felsic orthogneiss in the metamorphic tectonite belt. (A) Sheets of tonalite gneiss within a host of mica schist (65398). (B) Sheared contact between tonalite gneiss (left) and quartz schist (right) (65206).

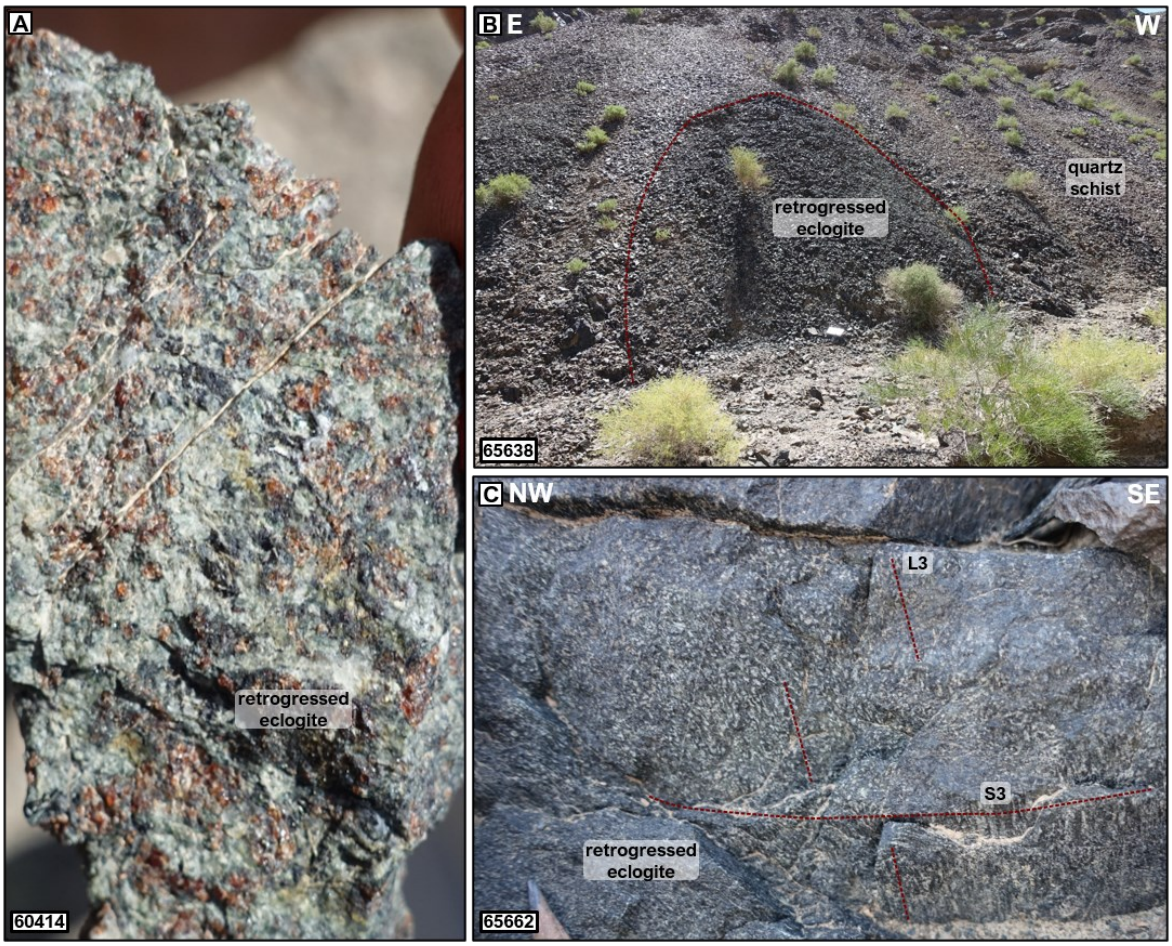

Figure 12. Illustrative photographs for the Gubaoquan eclogite. (A) Piece of eclogite from the core of a boudin, predominantly consisting of assemblage 2 and 3 (60414). (B) Example of a smaller boudin of eclogite, hosted by quartz schist (65638). (C) An entirely amphibolitised section of a boudin, illustrative of the extensive deformation at most boudin margins (65398).

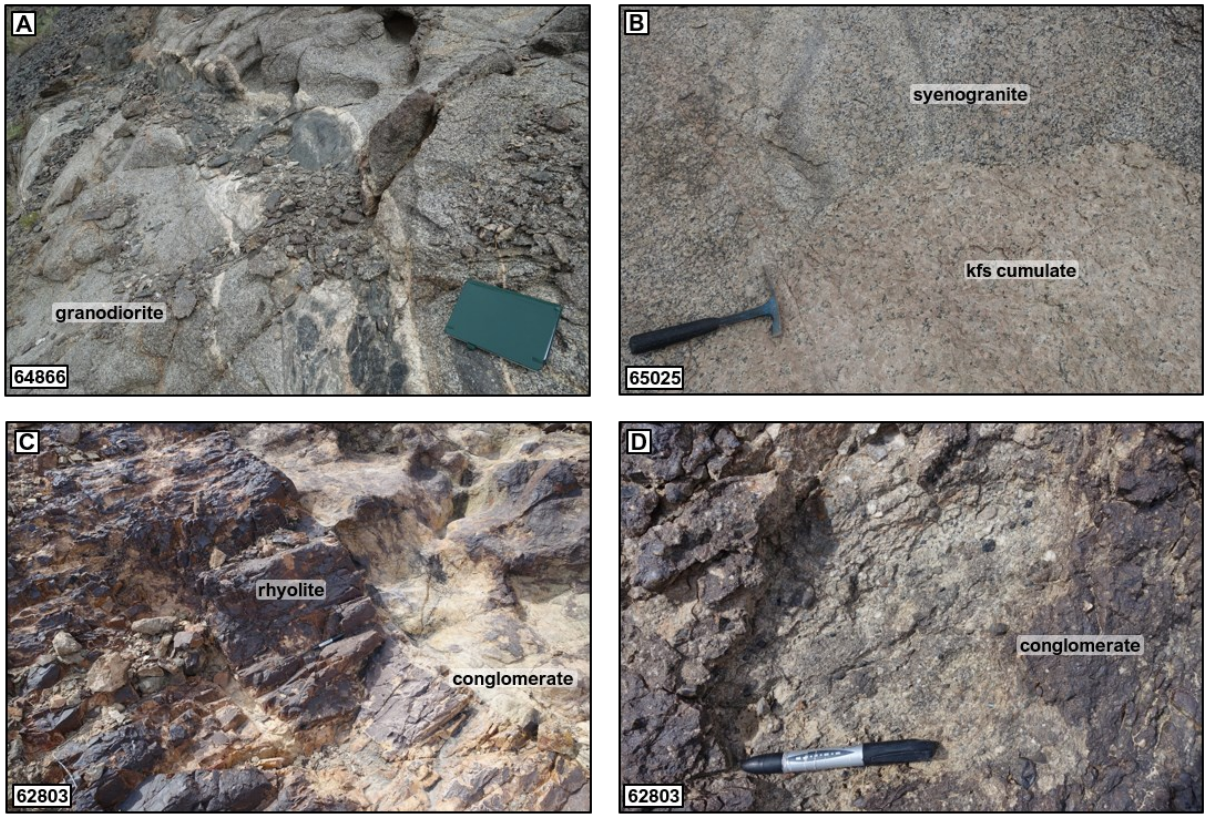

Figure 13. Illustrative photographs of the Ordovician- to Permian-age units across the mapping area; (60604). (A) Composite dyke of leucomonzogranite and microdiorite, crosscutting a hbl-bt-tit granodiorite. Presumed to be of Ordovician-Silurian age (Mao, Xiao, Fang et al., 2012; Mao, 2008) (64866). (B) Cumulate texture of potassium feldspar megacrysts within a megacrystic syenogranite, presumed to be of Silurian-Devonian age (Zhu et al., 2016) (65025). (C) Spherulitic rhyolite dykes crosscutting a conglomerate, both presumed to be of Permian age (Li, 2019) (62803). (D) Close-up of the conglomerate, showing poorly sorted, sub-rounded quartz and mafic clasts (62803).

Chapter 5
Structural architecture

Seven different planar and/or linear structural fabrics have been identified in the study area. These fabrics have been differentiated based on overprinting relationships, orientation, and/or metamorphic assemblage.

5.1 Folding and fabrics

5.1.1 *S1i*

S1 has only been observed within kyanite and garnet porphyroblasts in metasedimentary rocks in thin section, hence this foliation is labelled as an internal foliation (S1i). The composition of this fabric currently is unclear. In all samples, S1i is oriented broadly parallel to the external S3 foliation and compositional layering (Figure 15A-B). This suggests that S1 reflects shortening perpendicular and extension parallel to the compositional layering.

5.1.2 *S2/F2*

S2 is defined by the alignment of quartz, micas, kyanite, sillimanite in metasedimentary rocks, the alignment of hornblende and feldspar in the metabasites, and the alignment of hornblende, feldspar and quartz in felsic orthogneiss. Due to extensive refolding by F3 and younger structures, S2 strikes variably (Figure 7).

F2 folding has only been observed as crenulations preserved in kyanite and garnet porphyroblasts in thin section. These are mm-scale harmonic, open tight folds with broad hinge areas. F2 axial planes and S2 are oriented perpendicular to S1 in the porphyroblasts. In one example, a crenulation cleavage (S2i) is associated with these folds (Figure 14A-B). These observations suggest that S1i was folded by F2 and at least locally developed a crenulation cleavage (S2i) perpendicular to S1i.

At a meso-scale, S2 is difficult to recognise since it is generally transposed by F3 into a composite S2-S3 foliation. It has been preserved as a separate foliation in the hinges of F3 folds (Figure 4). S2 is present in most lithologies of the metamorphic tectonite belt. As the cross-cutting relationship between S1 and S2 has only been preserved within porphyroblasts, these fabrics could constitute a composite S1-2 foliation.

Based on S2 and F2, D2 was a major shortening event at a high angle to S1 and compositional layering. Due to extensive refolding by younger structures, it is unclear what the main shortening axis was at a macro scale.

5.1.3 *S3/L3/F3*

S3 is mainly a transposition foliation and hence, difficult to separate from S2 along the limbs of large F3 folds. S3, like S2 is characterised by the alignment of micas, quartz and feldspar in metasedimentary rocks and the alignment of hornblende, feldspar and quartz in the metabasites, including the Gubaoquan eclogite. In felsic orthogneiss, S3 is associated with ubiquitous augen textures of feldspar (Figure 14F). It occasionally is also associated with S-C fabrics (Figures 14F;15E-F) and accompanied by boudinaging (Figures 4;10C).

S3 strikes variably, due to extensive refolding (Figure 7). Refolding is most prominent towards the northern and southern edges of the mapping area (domains B-C, G-I) (Figure 7). S3 is predominantly aligned E-W to NW-SE, or sub-parallel to the structural grain of the mountain belt. Dips vary, being more than 60° to the north in the very north of the studied area. The metasedimentary rocks immediately north of the eclogite dip more shallowly, generally around 30° N. Lastly, the orthogneiss surrounding the eclogite bodies show steeper dips, exceeding 60° N on average.

L3 stretching and mineral alignment lineations are defined by stretched quartz and feldspar grains or stretched augen in the felsic orthogneiss (Figure 14C), by preferentially aligned micas and stretched quartz in the metasediments and by preferentially aligned amphiboles and plagioclase in the metabasites. L3 lineations generally have a westerly pitch. Considering the dominant N-dipping

S3 orientation, the above translates to primarily NW-plunging lineations (Figure 7). The refolding is clearly reflected in L3's spread.

F3 folds are tight to isoclinal, asymmetric structures and due to refolding, their axial planes lie on a broadly defined, steeply west-dipping great circle (Figure 8). The hinge lines correspondingly show a variety of plunges and are spread along an E-W-trending girdle. Hinges have visibly variable plunges (Figure 8). On a macro scale, F3 is associated with the isoclinal folding of S1-2 and compositional layering (Figures 4-5). As most units still are broadly laterally continuous, the enveloping surface to F3 lies at a low angle relative to the original compositional layering, which implies most folds are asymmetrical. In highly strained areas, both F3 hinge lines, axial planes and axial planar crenulation cleavages associated with F3 folds have orientations parallel to respectively L3 and S3, at meso- and macro-scale (Figure 14A-B;D). Elsewhere, S1-2 is still preserved and is continuous with the S3 foliation on the fold limbs (Figure 14A-C). Hence, S3 represents a composite foliation made-up of a transposed S1-2 and a newly developed axial planar cleavage to F3.

In thin section, S3 is oriented broadly perpendicular to S2i in staurolite and kyanite porphyroblasts (Figure 15C-D). Microfolding and a bimodal orientation of mica (Figure 16G-H) suggest the axial planar S3 crenulation cleavage formed as a result of folding and kinking of S1-2 biotite and/or sillimanite.

S3 is the dominant regional foliation within the metamorphic tectonite belt and is found in all metamorphic units. It commonly forms the main fabric in highly strained, locally mylonitic rocks. The latter have an L>>S tectonite fabric (Figure 14A-G). F3 folds have only been observed in the southern parts of the metamorphic belt (domains D-I) and are especially common in more quartz-rich metasedimentary rocks. In domain F (Figure 7), many S, Z and M folds occur. However, no systematic pattern was established during the mapping, and it was impossible to determine a larger-scale folding pattern based on the meso-scale structures alone. In domains G-I, it was difficult to establish whether F3 folds regionally displayed dominantly S or Z geometries, due to a lack of continuous outcrop, which prevented the reconstruction of a large-scale folding pattern. Thus, more macro-scale F3 folds may exist than those presently inferred.

At a regional scale, F3 fold hinges have broadly continuous, near-cylindrical orientations, but they locally vary highly at outcrop scale, such that they start to resemble sheath folds (Figure 14E). In the Gull Rapids area of the Split Lake block (Northern Superior superterrane), Downey et al. (2009) observed doubly plunging folds, SE-plunging S folds and NW-plunging Z folds; subsequently, they interpreted these as sheath folds developing from drag folds. When applying this to F3, the spread in hinge orientations appears less pronounced than for Downey et al. (2009). The dominant lineation L3 does have a similar orientation to F3 hinge lines at the outcrop scale in highly strained areas (Figure 14C). Regionally, F3 folds occur on all scales, with many meso-scale folds representing parasitic structures to larger-scale folds. Therefore, it is unlikely that F3 formed solely due to shearing-induced drag folding, although locally F3 folds may have been transformed into non-cylindrical or sheath folds following hinge rotation induced by localised shear accompanying D3. Combined, the structural evidence suggests that F3 folds mainly represent the expression of regional shortening, which locally was associated with localised shearing. Such a kinematic movement picture is consistent with the observed enhanced degrees of strain and folding near domain boundaries.

D3 generally led to a high strain (Figure 14A-G), commonly rendering it difficult to identify and systematically map smaller-scale shear zones within the tectonites. D3 microstructures predominantly indicate a top-to-the-south sense of shearing in the zones of locally enhanced degrees of shear such as those observed near domain boundaries. (Figure 14G). On the other hand, observations of north-directed senses of shearing are usually associated with normal displacements (Figures 14F; 15E-F). The north-directed senses of shearing that occur throughout domains F-I, are commonly found immediately adjacent to south-directed ones and they do not appear to be associated with particular domain boundaries, except domain boundary D-E and a laterally continuous zone of north-directed sense of shearing occurs immediately north of the eclogite.

The ubiquitous presence of S3 and L3 throughout the metamorphic tectonite belt, combined with the other characteristics of D3 structures, such as F3 folding at all scales, suggest it constitutes a regional event formed by shortening. No refolding of F2 folds by F3 has been observed. This implies that some F3 folds may represent refolded F2 folds. The transposition of S2 into S3 and F3

folding was accompanied and/or immediately followed by widespread S-directed shearing on S3, albeit with local zones of N-directed normal displacement. Strain localisation especially occurred at the domain boundaries.

5.1.4 *S4/F4*

S4 occurs as a crenulation cleavage in de hinge of F4 folds. It is defined by of preferentially aligned muscovite and quartz in the metasedimentary rocks, and hornblende and plagioclase in the metabasites. S4 generally dips steeply N or S.

F4 folds tend to be harmonic, open to tight structures (Figure 14G). Their axial planes lie oblique to compositional layering (Figure 14G). Characteristic for F4 folds are their steep, northerly-inclined, E-W-striking axial planes and E-W-trending hinge lines (Figures 8;14G). The hinges appear to plunge variably at a kilometre-scale, with one clear change in plunge direction happening north and south of the eclogites. However, no outcrop-scale plunge variations were observed, and it is unclear whether F4 folds were noncylindrical due to progressive deformation, or due to refolding.

L3's small circle distribution and S3's girdle both are indicative of refolding by predominantly E-plunging folds (Figure 8). F4 folds can be seen refolding F3 folds in several locations (Figure 14G-I). The interference geometry appears to resemble type-3 interference patterns (Ramsay, 1967) most closely, albeit with a less extreme angle between the axial planes and slightly different hinge line orientations (Figures 4-5).

D4 structures are most prominent towards the northern and southern edges of the mapping area (domains B-C, G-I; Figure 7). Mesoscale F4 folds are cut by both southern intrusions; the northern intrusion intruded along an F4 axial plane (Figures 4;7). Key examples of macro-scale D4 folds are the anticline and syncline that occur close to the Gubaoquan eclogite (Figure 4). Both folds have eastward plunges in the west and change to a westward plunge direction in the east, illustrative of the varying hinge orientations of F4. These two folds refold F3, giving rise to a complicated pattern (Figures 4-5).

S4 and F4 are indicative of continued regional N-S shortening, under greenschist to amphibolite-facies conditions. Except for boundaries that were unequivocally folded by F4 (G-H, H-I; Figure 7), re-activation during D4 cannot be excluded.

5.1.5 *S4/L4 in Ordovician-Silurian intrusive rocks*

This section solely discusses S4 and L4 in the Ordovician-Silurian granitoids: only one non-igneous structure was recorded in the Silurian-Devonian intrusion and the Permian-Triassic intrusion is too young to be relevant for Ordovician-Silurian tectonism. S4 and L4 generally consist of preferentially aligned hornblende, biotite, titanite, feldspar and/or quartz (Figure 14K-L). Occasionally, these rocks have a 5-10 mm-spaced compositional layering, resembling a gneissic texture. In both lithologies, S4 dips steeply N or S, whilst L4 generally plunges steeply towards the NW (Figure 8).

Since the Ordovician-Silurian intrusions crosscut F4 folds or intrude along their hinges (Figures 4;7), D4 must be coeval or older than D4 in the enveloping host rocks. The D4 fabric suggests that these intrusions were emplaced in a tectonically active environment, characterised by N-S compression and possibly sub-vertical shearing.

5.1.6 *S5/F5*

F5 and S5 are concentrated in a narrow zone near the contact with the Liuyuan ophiolite in the southern part of the area. F5 occurs as asymmetrical folds associated with shallowly SE-dipping S5 shear zones. This contact truncates the strike of units and S3 in domains I and H immediately to the north. Folds of similar orientation and geometry associated with comparable fault structures can also be found in the Liuyuan ophiolite and the sediments to the south of it. S5 is defined by the preferential alignment of greenschist-facies minerals such as actinolite, chlorite, epidote and/or plagioclase in phyllonite zones developed in metabasic lithologies (Figure 14J-K). S5 is rare outside the contact zone with the Liuyuan ophiolite and has not been observed in other lithologies. F5 folds have broadly NE-dipping axial planes that dip at various degrees (Figure 8). The hinges are all

shallowly plunging, predominantly to the NE. The F5 folds are intrafolial and have a consistent sense of asymmetry consistent with south-directed reverse shearing.

The restriction of F5 folds to the contact zone, their consistent sense of asymmetry and association with shear sense indicators suggest they represent drag folds formed during non-coaxial strain. The metamorphic minerals defining D5 fabrics indicate that this deformation stage was associated with greenschist-facies metamorphic conditions and south-directed reverse shearing. The abundance of D5 structures near the boundary separating the Liuyuan ophiolite and the metamorphic tectonite indicates it represents an important south-directed reverse fault structure.

5.1.7 *F6*

F6 is not associated with any planar or linear fabric. Within interbedded psammites – metapelites (domain E; Figure 7), F6 consists of harmonic box folds, which have approximately N-S-striking, sub-vertical axial planes and moderately N-plunging hinge lines (Figure 14P). In other areas, F6 folds are open, upright folds or crenulations with similar axial planes and variably N-S-plunging hinge lines (Figures 8;14O). These folds are particularly prominent near the southern boundary of the metamorphic belt and near major brittle faults.

No conclusive overprinting relationships were observed between F6 and F5, except that the orientation of F5 folds shows a spread that could be the result of F6 refolding (Figure 8) and that F6 folds generally have orientations at a high angle to F5. F6 is seen refolding layers that were affected by F3 (Figure 14O). Like F5, F6 is also present in the Permian Liuyuan ophiolite (Santos, pers. comm.).

D6 is also associated with macro-scale brittle faulting: a conjugate set of brittle faults crosscut nearly all lithologies (Figures 4;7), one trending NW-SE (B1), another NE-SW (B2). B2 is more common and offsets B1. Both are associated with sinistral displacement. Offset on B1 generally measures up to a few hundred metres, whereas B2 is usually associated with tens of metres of displacement, with a few outliers consistent with several hundred metres of displacement. B2

was observed in outcrop on occasion, where it was narrow and discrete. At one locality, a fault attributed to B2 was associated with epidote veins.

Both fault sets crosscut the northern and south-western intrusions, although some appear to die out within the intrusion or are impossible to trace (Figure 8). Neither fault set crosscuts the north-eastern intrusion. B2 crosscuts the contact with the ophiolite, suggesting these faults developed after ophiolite obduction.

F6 and the conjugate fault set indicate E-W compression, parallel to the structural grain of the metamorphic tectonite belt. The brittle faulting and F6's style of folding indicative of low-strain and lower-grade metamorphic conditions.

5.1.8 *F7*

F7 folds have only been observed as refolded F6 folds (Figure 14Q). They have a tight geometry, moderately dipping, NW-SE-striking axial planes and variably NW-plunging hinge lines (Figures 8; 14Q). Their geometry suggests NW-SE dextral displacement.

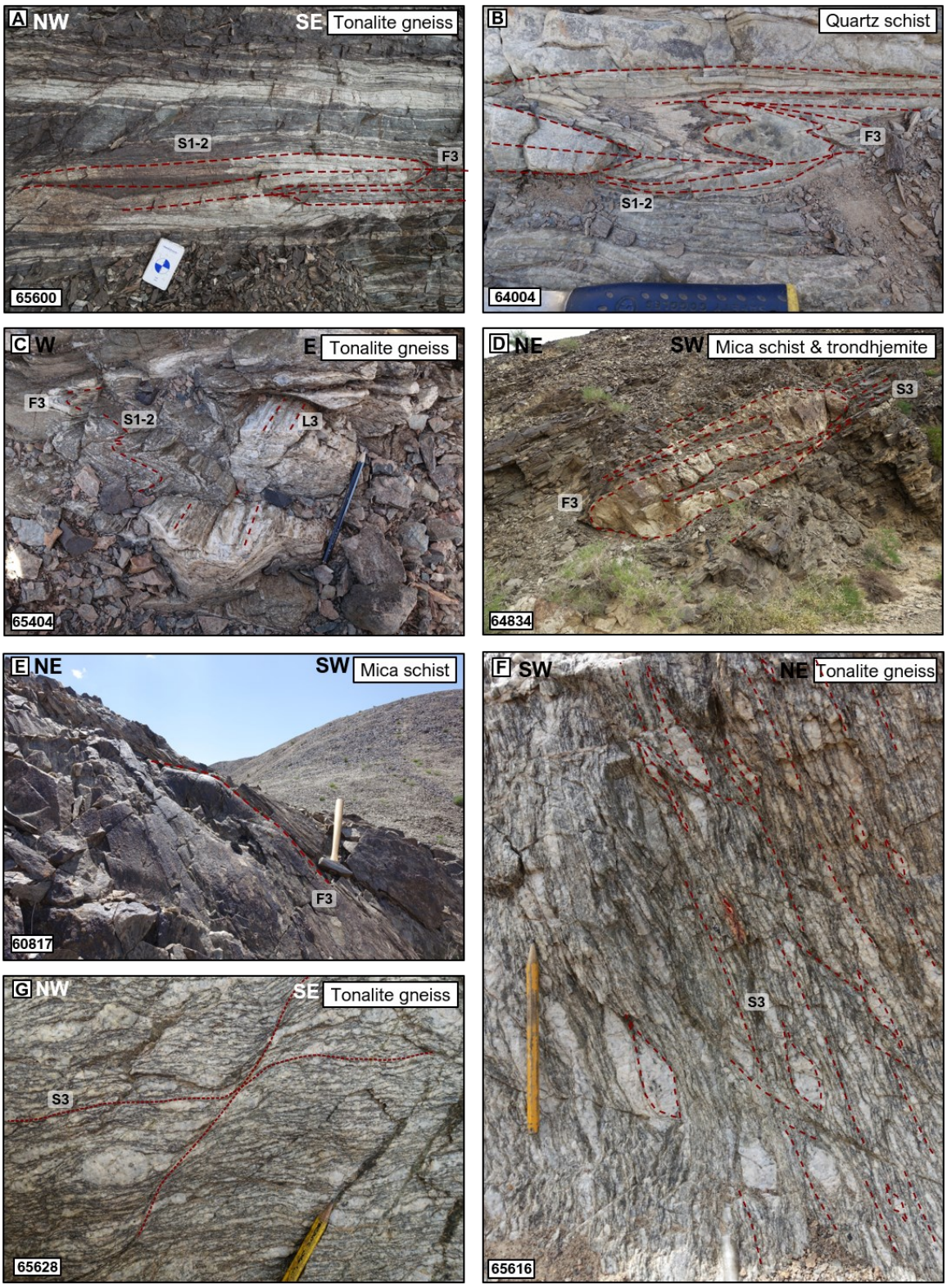
A NW
SE
Tonalite gneiss
S1-2
F3
65600
B
Quartz schist
F3
S1-2
64004
C W
E
Tonalite gneiss
F3
S1-2
L3
65404
D NE
SW
Mica schist & trondhjemite
S3
F3
64834
E NE
SW
Mica schist
F3
60817
F SW
NE
Tonalite gneiss
S3
65616
G NW
SE
Tonalite gneiss
S3
65628

Figure 14, previous page. Examples of structures observed in the field. (A) Isoclinal F3 folds within a highly sheared tonalite gneiss, which transpose S1-2 into S3 (65600). (B) Isoclinal F3 folds within a quartz schist, which transpose S1-2 into S3 (64004). (C) Isoclinal F3 folds in a highly sheared tonalite gneiss, exemplifying the (sub-)parallel relationship between L3 and F3 hinges (65404). (D) F3-folded metatrondhjemite dyke within a mica schist, illustrative of the meso-scale F3 folds in the area (64834). (E) Variably plunging isoclinal F3 fold in a mica schist. Photo made by S. Lin (60817). (F) D3 sigmoidal porphyroblasts and shear bands indicating north-normal displacement, observed near the H-I domain boundary (65616). (G) Sheared tonalite gneiss with shear bands indicating top -SE displacement (65628).

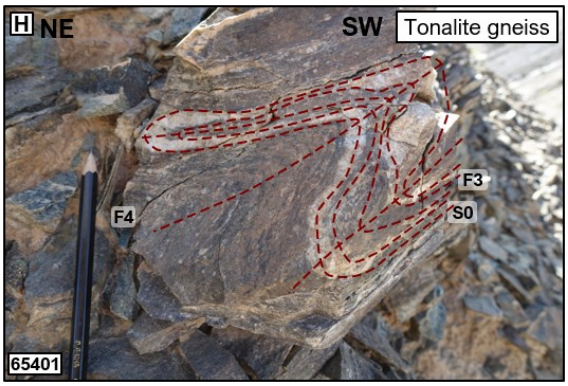
H NE
SW
Tonalite gneiss
F4
F3
S0
65401

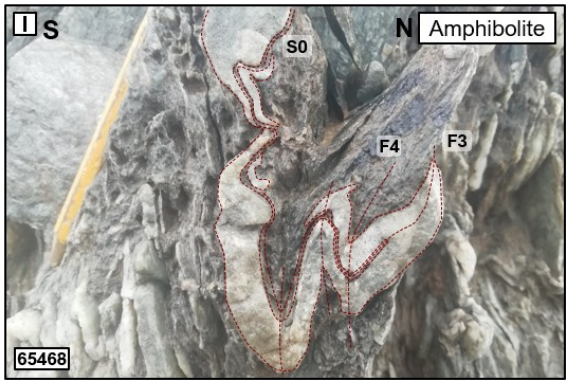
I S
N
Amphibolite
S0
F4
F3
65468

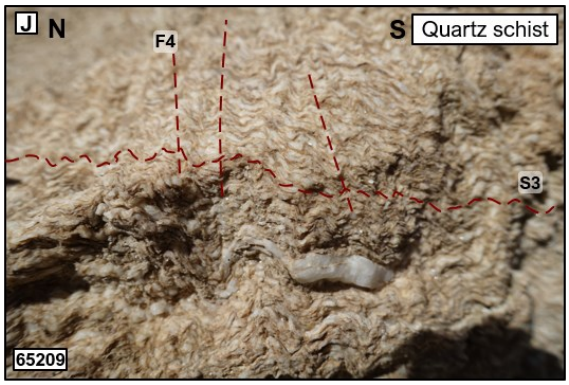
J N
S
Quartz schist
F4
S3
65209


K NW
SE
Granodiorite
S4
64885

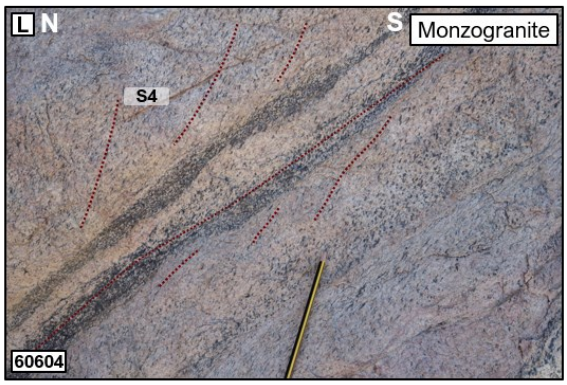
L N
S
Monzogranite
S4
60604

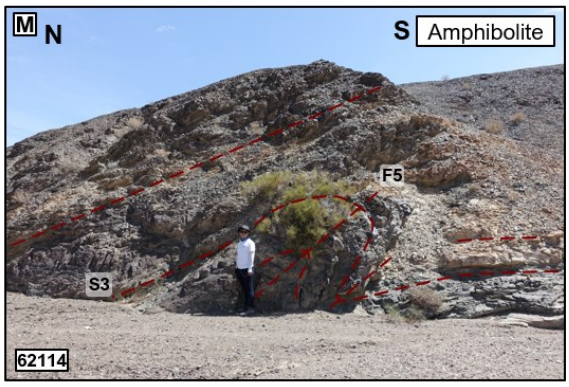
M N
S
Amphibolite
F5
S3
62114

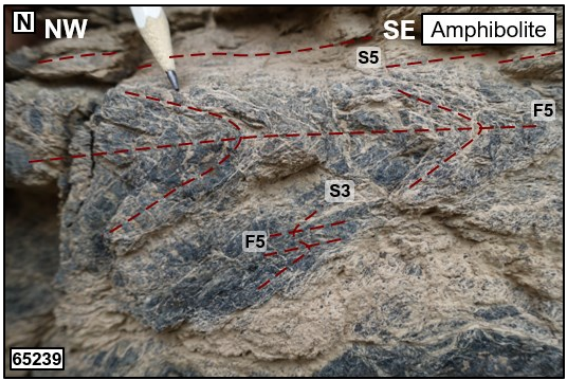
N NW
SE
Amphibolite
S5
F5
S3
F5
65239

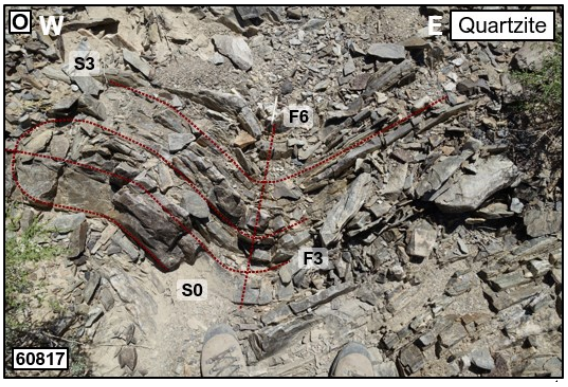
O W
E
Quartzite
S3
F6
F3
S0
60817

Figure 14, continued, previous page. (H) Isoclinal F3 folds refolded by slightly inclined, tight F4 folds in a tonalite gneiss (65401). (I) A quartz vein in an amphibolite showing fold interference patterns comparable to D (65468). (J) A quartz schist showing an S4 crenulation. Field of view is approximately 10 cm wide. (65209). (K) Sheared and folded (D4) granodiorite of presumed Silurian age (Mao, Xiao, Fang et al., 2012; 2008), crosscut by epidote vein (64885). (L) Compositional layering and top-SE shear fabrics (D4) within a monzogranite, presumed to be of Silurian age (Mao, 2008) (60604). (M) South-directed D5 shear zone and drag fold (62114). (N) Close-up of a microstructure similar to G (65239). (O) Example of a F6 open fold, refolding F3 isoclinal folds; quartzite (60817).

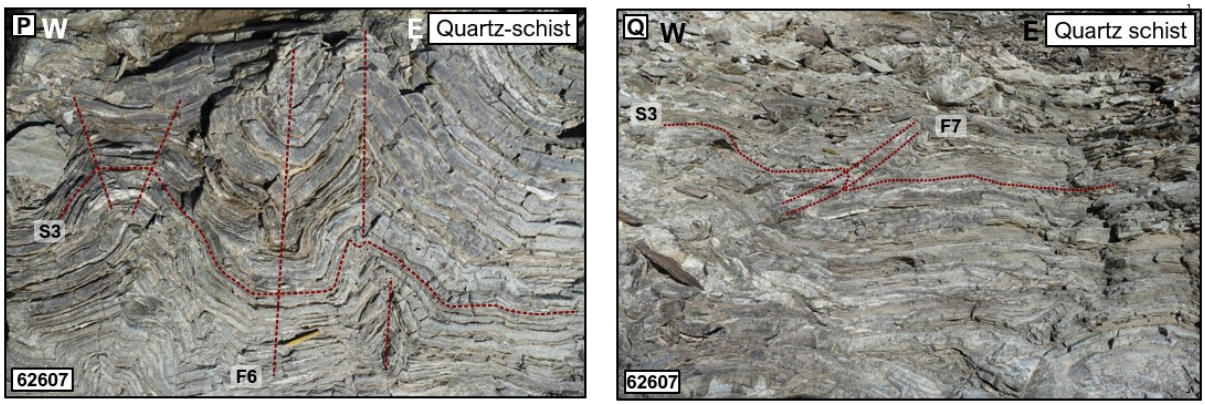

Figure 14, continued. (P) F6 folds in a quartz-schist (62607). (Q) F7 folds in a quartz schist, constituting refolded F6 box folds (62607).

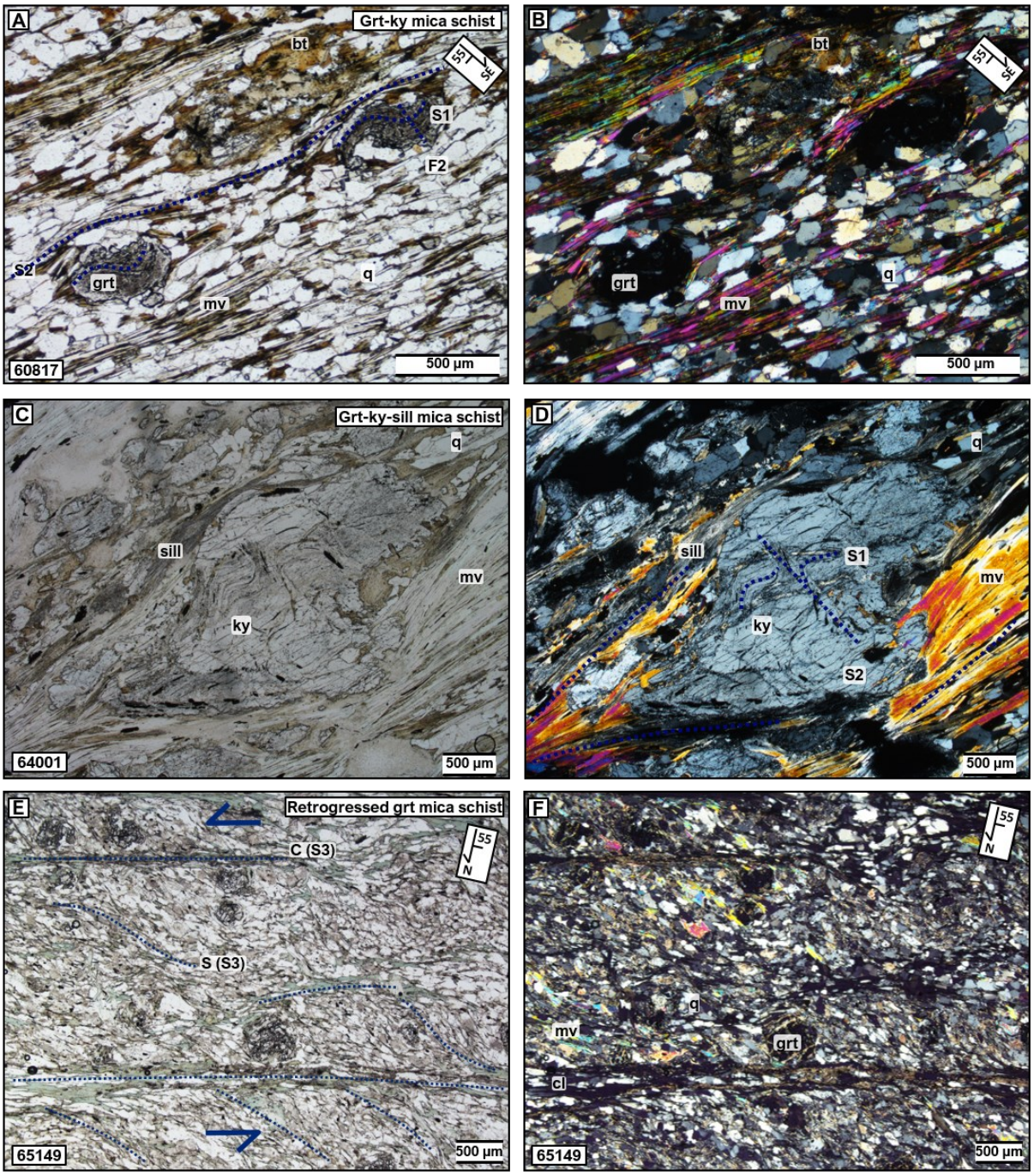

Figure 15. Overview of structures observed in thin section. (A-B) Garnet crystals with a folded internal foliation (S2), oriented sub-parallel to the S3 external foliation (60817). (C-D) Kyanite porphyroblast with a crenulated (S2) internal S1 foliation. The S2 is oriented perpendicular to the external S3 foliation, the S1 parallel (64001). (E-F) Mica schist with S3 S-C fabric, indicative of top-N displacement (65149); for mineral abbreviations, see **Figure 16**.

Chapter 6
Metamorphic architecture

The studied outcrops and thin sections cover the whole area, albeit with a higher sampling density in the vicinity of the eclogite.

Metasediment assemblages and index minerals

Optical petrography demonstrated a complex polymetamorphic history. Most metasediments were not pelitic enough to allow growth of high-grade metamorphic indicator minerals (such as aluminosilicates); most were quartzites or quartz-schists, which generally contained small amounts of white or brown mica and abundant quartz. Locally, garnet is visible. Only the mica schists regularly contained garnet and all three Al_2SiO_5 polymorphs, although the three have not been observed together in one single sample. Staurolite was found in a few samples as well.

No clear field gradient was recognised. Kyanite occurs in most domains except in domains A-C. However, that could be due to a sampling bias or a lack of suitable lithologies.

Garnet occurs as medium to large (≤ 1 cm) porphyroblasts, which sometimes have a small rim and/or infilled fractures with variable amounts of chlorite, muscovite, biotite and/or quartz (Figure 16A). Usually, garnet appears to be pre- to inter-tectonic with respect to the dominant foliation (S3): its internal foliation commonly does not align with the external S3 (Figure 15A-B). In several cases, the garnet appears to have grown over an earlier, crenulated foliation (S1 folded by F2) that is parallel to the current foliation (S3) (Figures 15A-B;16A). None of the observed garnets preserved an S2 foliation. Based on these observations, (part of the) garnet growth would have occurred at the onset of D2.

Kyanite forms small to very large (< 3 cm) square to rectangular subhedral porphyroblasts, that usually appear relatively fresh and have a pre- to syn-tectonic relationship to S3 (Figure 15C-D). Some crystals have an S1 internal foliation, which is folded into F2 folds with S2 crenulation cleavages (Figure 15C-D). In a few cases, kyanite contains garnet inclusions, suggesting (part of

the) kyanite growth post-dates initiation of garnet growth (Figure 16C). In another sample, garnet seems to be growing into a kyanite crystal (Figure 16D). These apparently contradicting relationships suggest both minerals grew, at least in part, coevally. Potentially, the contradicting relationships resulted from differences in rock bulk composition. At least (part of the) kyanite growth took place during D2 and before D3.

Sillimanite has only been observed as fibrolite. It is commonly found in association with kyanite, growing at their upper and lower grain boundaries, relative to S3 (Figure 15C-D). In other cases, it is found growing in close association with biotite, sometimes epitaxially growing onto it (Figure 16G-H). In this sample, both biotite and sillimanite were kinked and isoclinally folded during D3. These observations suggest that sillimanite formed before D3, during D2 or D1 and post-dates kyanite growth.

Staurolite was only found in a few samples, forming small- to medium-size inclusion-rich anhedral porphyroblasts. It always appeared syn-tectonic relative to S3 (Figure 15E-F). There are no rocks that contain both sillimanite and staurolite. Based on their relative relationships to S3, staurolite would have formed after sillimanite.

Andalusite occurs as <1.5 cm rectangular to squared subhedral crystals (Figure 16I). No chiastolitic texture has been observed. It frequently contains an S3 internal foliation (Figure 16I), suggesting andalusite growth occurred during or after D3. The growth relationship between staurolite and andalusite currently is unknown, but based on their relative relationship to S3, andalusite would either be coeval to staurolite or post-date it.

Lastly, white mica formed as part of S4 crenulation cleavages (Figure 16J). However, S4 has only been observed in rather unfertile quartz schists; additional minerals may be stable in more fertile rocks.

Thus, the indicator minerals would have formed in the following sequence: (I) garnet + kyanite; (II) sillimanite; (III) staurolite, andalusite; (IV) white mica.

Metabasite assemblages – Gubaoquan eclogite

At least five assemblages were observed in the eclogites. Based on overprinting relationships, omphacite-garnet-rutile is the oldest assemblage (1). It is rare and only present in a few samples (Figure 17A). This assemblage has no observable fabric associated with it (i.e. nearly isotropic).

In most samples, the omphacite was largely replaced by clinopyroxene and plagioclase symplectites (sym. I), with garnet preserved (Figure 17A-B). This represents assemblage 2.

Symplectite I and garnet commonly have rims of brown-green hornblende, which sometimes would occur as symplectites with quartz (sym. II) (Figure 17A-B) (assemblage 3). The hornblende-bearing symplectites are coarser than the clinopyroxene-plagioclase symplectites. The hornblende assemblages usually are weakly to strongly foliated, primarily defined by the preferential alignment of hornblende. This is the dominant foliation in the eclogites, which is oriented sub-parallel to S3 (Figure 17C). This suggests assemblage 3 is sub-coeval with D3.

The brownish green hornblende may in turn be rimmed by blue-green amphibole, which appears to constitute an assemblage with biotite and quartz. (Figure 17D-E). This constitutes assemblage 4. Biotite and quartz occasionally occur as a symplectite (sym. III; Figure 17E).
Lastly, a few samples have folded veins of prehnite, quartz, plagioclase and chlorite, which cut earlier assemblages (Figure 17F). This represents the fifth and final observed assemblage in the eclogites.

Metabasite assemblages and index minerals – other outcrops

The metabasites outside of the eclogite zone principally consist of a strongly foliated hornblende-plagioclase-quartz fabric (Figure 18B), frequently with garnet (Figure 18A), rutile and/or titanite. This fabric is oriented sub-parallel to S3 in the metasediments (Figure 18A), suggesting it formed broadly coevally. Garnet, if present, appears post-kinematic relative to the main foliation, in contrast to the pre-kinematic garnets found in the metasediments. Part of the garnet growth in the metabasites may therefore represent a different, later part of the metamorphic

cycle. The rutile appeared syn- to post-kinematic and occasionally is rimmed by titanite. S4 is associated with a similar assemblage as S3, but without garnet (Figure 18B)

A few samples bear a foliation that primarily consists of chlorite, epidote and/or actinolite, which would represent greenschist-facies conditions. This fabric crosscuts S3 and is commonly associated with D5 shear zones near the boundary with the Liuyuan ophiolite (Figure 14J). This suggests that these greenschist assemblages represent D5 metamorphic conditions.

Orthogneiss index minerals

The extensive dynamic recrystallisation of quartz and feldspar prevalent throughout the gneisses testifies to the elevated PT conditions they were subjected to. Metamorphic indicator minerals are rare in these rocks, except for a few samples with garnet. The garnets showed various growth relationships, but most often appeared syn-kinematic. Except for one sample from domain I, all garnet-bearing samples were sampled in domain H (Figure 7).

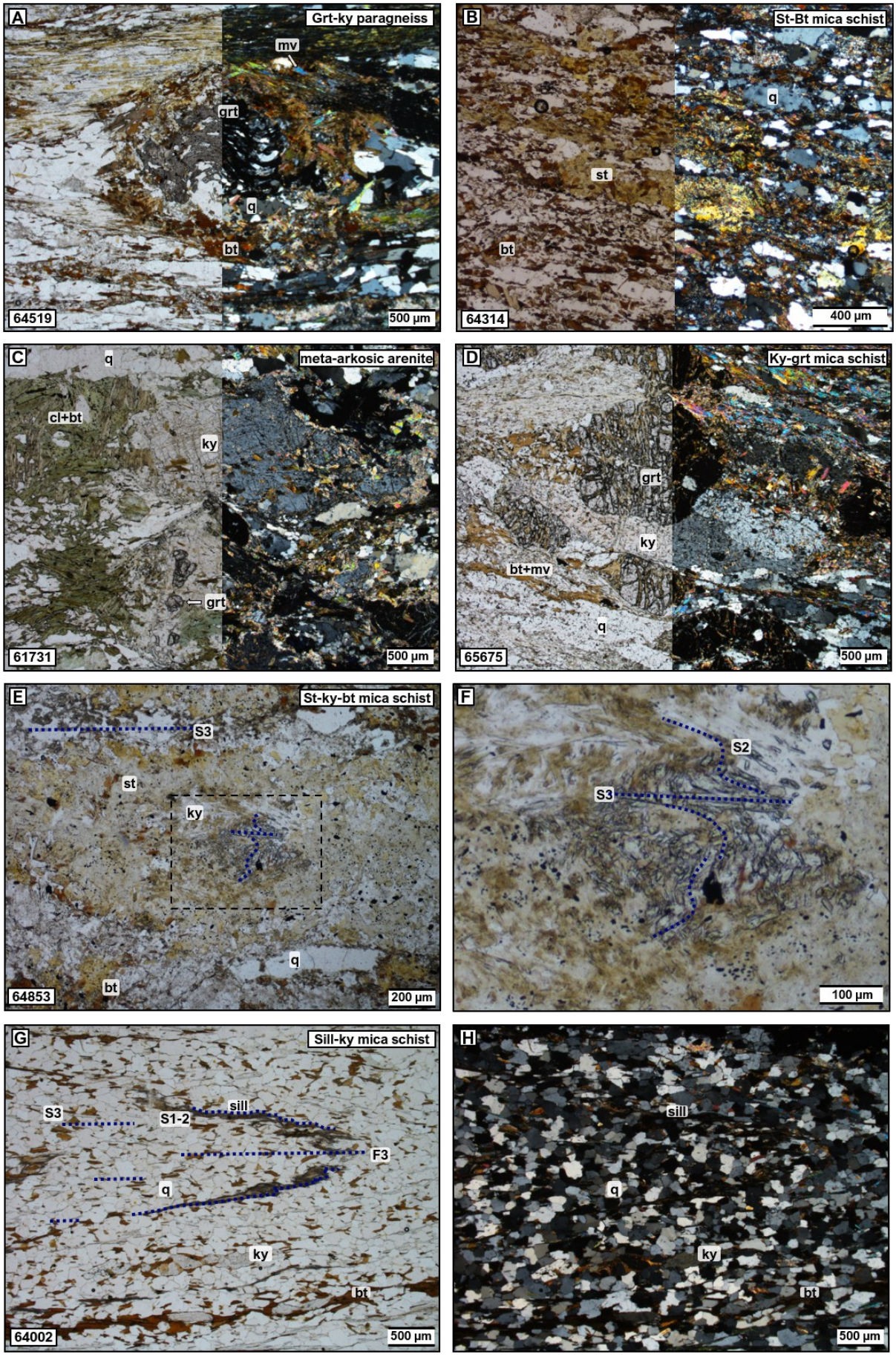
A
Grt-ky paragneiss
mv
grt
q
bt
64519
500 µm
B
St-Bt mica schist
q
st
bt
64314
400 µm
C
q
meta-arkosic arenite
cl+bt
ky
grt
61731
500 µm
D
Ky-grt mica schist
grt
ky
bt+mv
q
65675
500 µm
E
St-ky-bt mica schist
S3
st
ky
q
bt
64853
200 µm
F
S2
S3
100 µm
G
Sill-ky mica schist
S3
S1-2
sill
F3
q
ky
bt
64002
500 µm
H
sill
q
ky
bt
500 µm

Figure 16, previous page. Thin sections of metasedimentary rocks. (A) A garnet porphyroblast with a folded internal foliation, within a kyanite-bearing two-mica schist. The porphyroblast is mantled by a fine-grained assemblage of biotite, muscovite, quartz and chlorite (64519). (B) A syn-tectonic staurolite crystal within a biotite mica schist (64314). (C) A kyanite porphyroblast with garnet inclusions in a meta-arkosic arenite (61731). (D) A garnet crystal partially overgrowing a kyanite crystal, within a two-mica schist (65675). (E-F) Syn-tectonic staurolite crystal, that mantles a folded, kyanite-bearing S2 foliation that lies perpendicular to the external S3 foliation (64853). (G-H) A biotite-sillimanite-bearing S1-S2 foliation is kinked, isoclinally F3 folded and transposed parallel to S3 (64002).

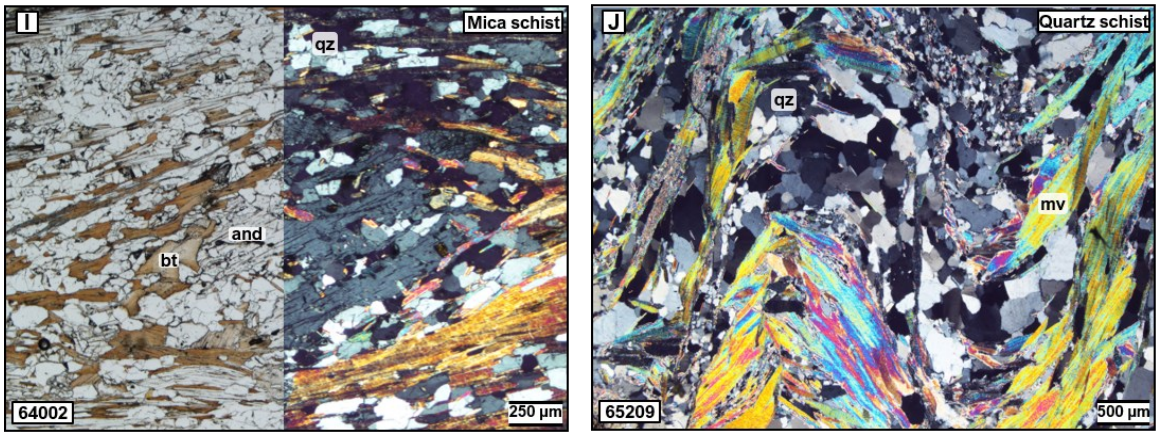

Figure 16, continued. (I) Andalusite porphyroblast in mica schist, syn- to inter-tectonic relative to the dominant S3 foliation (64002). (J) F4 folds in a quartz schist. A mv-qz-bearing S4 crenulation cleavage is starting to form; mineral abbreviations: grt = garnet, ky = kyanite, plg = plagioclase, bt = biotite / biotite, mv = white mica, sil = sillimanite, am = amphibole, q = quartz, tit = titanite, rut = rutile, st = staurolite, sym = symplectite, and = andalusite, omp = omphacite.

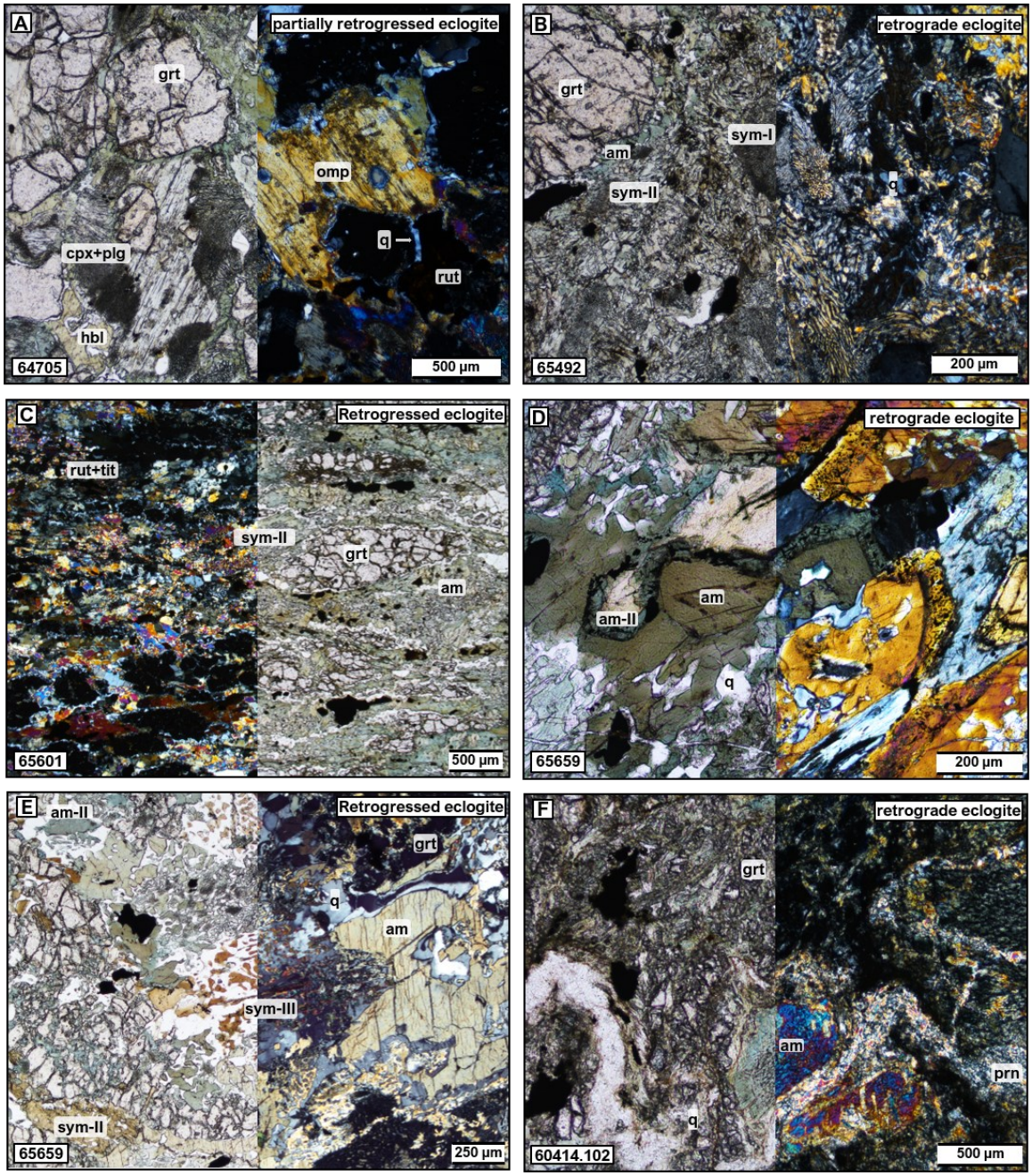

Figure 17. Thin sections of the Gubaoquan eclogite. (A) A partially retrogressed sample (ass. II), still preserving omphacite crystals (ass. I) (64705). (B) A retrogressed eclogite predominantly composed of ass. II and III, containing both sym. II (clinopyroxene and plagioclase) and III (amphibole and quartz) (65492). (C) Foliated (S3) retrogressed eclogite, predominantly composed of assemblage III (65601). (D) Retrograde eclogite with an older, brown-green amphibole (ass. III) being overgrown by a newer blue-green amphibole (ass. IV) (65659). (E) Retrograde eclogite with biotite-quartz symplectites (sym. III) (ass. IV). (F) Retrogressed eclogite predominantly composed of ass. II and III, crosscut by meandering veins predominantly composed of prehnite (ass. V) (60414.102). For mineral abbreviations, see **Figure 16**.

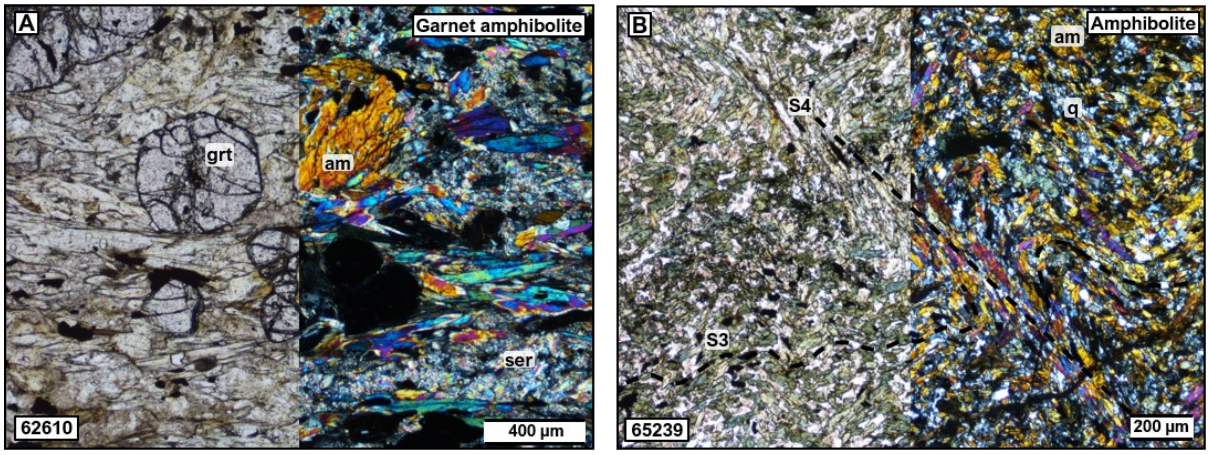

Figure 18. Thin sections of meta-igneous rocks. (A) Example of a garnet amphibolite, where the garnet appears to be late-tectonic (62610). (B) Amphibolite-facies S4 crenulation overprinting an earlier amphibolite-grade S3 foliation. For mineral abbreviations, see **Figure 16**.

Chapter 7
Geochronology

In total, four samples were analysed with SHRIMP. For the samples analysed using a 13 μm spot size, the Temora standard gave acceptable results, with 1 spot out of 17 rejected (Appendix C). Similarly, for the 24 μm spot size, 2 spots out of 33 were rejected (Appendix C). This indicates that the data are of sufficient quality for a reliable interpretation. All samples were plotted on Wetherill Concordia plots as the $^{206}Pb/^{238}U$ age was thought to be more suitable for the age range of the sample. All errors in the main text are given in 95% confidence intervals.

As for the main eclogite body (18LY60414), zircons from two samples were analysed: one from the freshest part (60414.101, from here-on referred to as .101; Figure 19A) and one from the amphibolitised rim (60414.102, from here-on referred to as .102; Figure 19B). This was done to verify whether any additional zircon had grown during retrogression or whether any resetting of earlier zircon growths had taken place (Carson et al., 2002). In thin section, the fresh sample (.101) had an assemblage transitional between assemblages 2 and 3, whereas the retrograde sample (.102) primarily consisted of assemblage 3 with vestiges of assemblage 2, overprinted by assemblages 4 and 5. In both samples, the zircons cores are highly resorbed and display complex growth zoning and occasionally are metamict, whereas the rims are homogeneous (Corfu et al., 2003) (Figures 20D;21D). The zircons have high Th/U ratios in the cores (0.11-0.36 for .101, 0.16-0.28 for .102) and low ratios (0.00-0.04 for both .101 and .102) in the rims (Tables 1;2). Zircons from sample .101 are approximately half the size of those from .102, on average.

In .101, one zircon rim yielded a Neoproterozoic $^{206}Pb/^{238}U$ age (8R; Table 1), whilst in .102 three did (1R, 2R, 9R; Table 2). These spots may have been non-zoned core domains or were almost immediately underlain by core zircon. Therefore, these were included in the zircon core data set.

The core age data set for .101 has a mean $^{206}Pb/^{238}U$ age of 836 ± 34 Ma (Figure 20B). Five spots (1C, 3C, 4C, 8R, 8C; Table 1) yielded relatively young ages (Figure 20A). These spots

are interpreted to be mixed domain ages and are therefore excluded. The resulting Concordia age is 874 ± 23 Ma (MSWD (of concordance) = 0.93; probability (of concordance) = 0.34) (Figure 20A).

.102's core data set has a mean $^{206}Pb/^{238}U$ age of 855 ± 23 Ma (Figure 21B). Two zircons (7C. 10C; Table 2) yielded relatively young ages. These are interpreted to represent mixed domain ages and are therefore excluded. One zircon (9C; Table 2) yielded a relatively old age. This is interpreted to be an inherited zircon and was excluded from the final age calculation. The resulting Concordia age is 872 ± 13 Ma (MSWD (of concordance) = 2,2; probability (of concordance) = 0.13) respectively (20A;21A) (Figure 21A).

The zircon rim spots in sample .101 have a mean $^{206}Pb/^{238}U$ age of 452 ± 30 Ma (Figure 20C). Two spots (2R, 7R: Table 1) have very large errors for $^{207}Pb/^{235}U$. These were rejected based on their low precision. The resulting Concordia age is 449 ± 23 Ma (MSWD (of concordance) = 2.3; probability (of concordance) = 0.13) (Figure 20A).

In sample .102, the zircon rims have a mean age of $^{206}Pb/^{238}U$ age of 451 ± 23 Ma (Figure 21C). Three zircon rims lie just above the chosen cluster (3R, 7R, 10R;Table 2; Figure 21A). Based upon the transmitted light images, all three may be underlain by core zircon. Thus, these might represent mixed domain ages and were therefore rejected. The resulting Concordia age is 436 ± 23 Ma (MSWD (of concordance) = 1.6; probability (of concordance) = 0.21) (Figure 21A).

A garnet-bearing gneissic tonalite (18LY63905, from here-on referred to as 63905) was sampled within domain H (Figure 7; Figure 19C). The gneiss occurred as a small lens within an area dominated by mica schists and is one of the most garnetiferous rocks except for the eclogite. In thin section, this sample was found to be a two-mica meta-tonalite with 15 vol-% garnet. The reason for selecting this sample was that no protolith ages yet existed for this lithological domain and that zircon rims from this unit could have grown during high-grade metamorphism. The zircons have resorbed cores with growth zoning or lengthwise parallel zoning and commonly have metamict areas (Figure 22D). Most zircons have one or several homogeneous rims. The cores generally have high Th/U ratios (0.18-0.68), except for two (5C, 7C: 0.02-0.06), while the rims have low ratios (0.00-0.02), except for one spot (5R: 0.51) (Table 3).

The ages were discordant, and a discordia line fitted to all data points was found to have lower and upper intercepts at 469 ±17 Ma and 1490 ± 19 Ma respectively (MSWD (of concordance) = 3.2) (Figure 22A-C). No zircons were excluded.

A highly sheared gneissic tonalite (Figure 19A) sample (18LY64501, from here-on referred to as 64501) was collected from domain F (Figure 7), with the intent of dating D3 deformation in this area. In thin section, the rock was found to be a leucocratic two-mica meta-tonalite. Its zircons have minimally resorbed cores that display complex growth zoning and lengthwise parallel zoning with minor metamict areas (Figure 23D). Most have thin, homogeneous rims that are too small for dating. The zircon cores show a wide range of Th/U ratios (0.10-0.67) (Table 4).

The zircons primarily yielded Neoproterozoic ages (Figure 23A). One spot at ~1.4 Ga (5; Table 4) probably represents an inherited zircon, which was therefore excluded. The resulting cluster has a Concordia age of 902.8 ± 6.5 Ma (MSWD (of concordance) = 1.4; probability (of concordance) = 0.24) (Figure 23A-C).

Spot	U	Th	Th/U	% $^{206}Pb_c$	$^{207}Pb^*/^{235}U$			$^{238}U/^{206}Pb$			$^{207}Pb^*/^{206}Pb^*$			ρ	$^{206}Pb/^{238}U$ age			$^{207}Pb/^{206}Pb$ age			%Disc.
~~1.C~~	~~31~~	~~5~~	~~0.18~~	~~0.00~~	~~1.214~~	~~±~~	~~7.0~~	~~8.20~~	~~±~~	~~2.8~~	~~0.0722~~	~~±~~	~~6.4~~	~~0.40~~	~~742~~	~~±~~	~~20~~	~~991~~	~~±~~	~~130~~	~~25~~
1.R	11	0	0.01	0.00	0.590	±	14	15.78	±	4.9	0.0676	±	13	0.35	396	±	19	855	±	280	54
2.C	338	80	0.24	0.00	1.393	±	2.2	6.819	±	1.3	0.0689	±	1.7	0.59	882	±	10	895	±	36	1
~~2.R~~	~~13~~	~~1~~	~~0.04~~	~~3.74~~	~~0.52~~	~~±~~	~~62~~	~~11.13~~	~~±~~	~~6.9~~	~~0.042~~	~~±~~	~~61~~	~~0.11~~	~~554~~	~~±~~	~~37~~	~~230~~	~~±~~	~~1500~~	~~341~~
~~3.C~~	~~22~~	~~2~~	~~0.11~~	~~0.00~~	~~1.21~~	~~±~~	~~9.2~~	~~7.58~~	~~±~~	~~3.3~~	~~0.0667~~	~~±~~	~~8.6~~	~~0.36~~	~~799~~	~~±~~	~~25~~	~~829~~	~~±~~	~~180~~	4
3.R	14	0	0.01	0.00	0.650	±	15	13.13	±	4.7	0.0619	±	14	0.32	473	±	21	671	±	300	30
~~4.C~~	~~25~~	~~4~~	~~0.15~~	~~1.24~~	~~1.19~~	~~±~~	~~15~~	~~7.37~~	~~±~~	~~3.3~~	~~0.0635~~	~~±~~	~~15~~	~~0.22~~	~~820~~	~~±~~	~~25~~	~~725~~	~~±~~	~~310~~	~~13~~
4.R	10	0	0.00	0.00	0.527	±	17	13.60	±	5.3	0.0519	±	17	0.31	458	±	24	282	±	380	-62
5.C	23	3	0.14	0.00	1.37	±	7.8	6.93	±	3.6	0.0687	±	6.9	0.47	869	±	30	891	±	140	2
5.R	11	0	0.00	0.00	0.560	±	15	13.09	±	5.3	0.0531	±	14	0.36	475	±	24	334	±	320	-42
6.C	25	4	0.15	0.00	1.279	±	7.2	7.01	±	3.1	0.0650	±	6.5	0.42	860	±	25	774	±	140	-11
6.R	9	0	0.01	0.00	0.87	±	16	12.51	±	6.2	0.079	±	15	0.38	496	±	30	1,166	±	300	58
7.C	29	4	0.13	0.00	1.304	±	7.2	7.01	±	3.3	0.0663	±	6.4	0.46	860	±	27	815	±	130	-6
~~7.R~~	~~12~~	~~0~~	~~0.00~~	~~5.19~~	~~0.36~~	~~±~~	~~94~~	~~14.96~~	~~±~~	~~6.6~~	~~0.039~~	~~±~~	~~94~~	~~0.07~~	~~417~~	~~±~~	~~27~~	~~420~~	~~±~~	~~2500~~	~~200~~
~~8.C~~	~~71~~	~~26~~	~~0.36~~	~~0.49~~	~~1.185~~	~~±~~	~~6.6~~	~~7.83~~	~~±~~	~~2.1~~	~~0.0673~~	~~±~~	~~6.2~~	~~0.31~~	~~774~~	~~±~~	~~15~~	~~847~~	~~±~~	~~130~~	~~9~~
~~8.R~~	~~28~~	~~4~~	~~0.13~~	~~0.00~~	~~1.307~~	~~±~~	~~7.0~~	~~7.41~~	~~±~~	~~3.0~~	~~0.0703~~	~~±~~	~~6.3~~	~~0.43~~	~~816~~	~~±~~	~~23~~	~~936~~	~~±~~	~~130~~	~~13~~
9.C	32	6	0.18	0.90	1.34	±	11	6.87	±	4.4	0.0669	±	10	0.39	876	±	36	836	±	220	-5
9.R	11	0	0.00	0.00	0.654	±	12	14.15	±	4.7	0.0671	±	12	0.38	440	±	20	842	±	240	48
10.C	26	4	0.14	0.00	1.486	±	5.4	7.12	±	2.8	0.0768	±	4.7	0.52	847	±	22	1,115	±	93	24
10.R	12	0	0.01	0.00	0.562	±	12	13.65	±	4.8	0.0556	±	11	0.39	456	±	21	436	±	250	-5

Table 1: geochronological data for sample 60414.101. Errors are given in one sigma percentages, except for the ages, which are given in one sigma absolutes. Rejected ages are struck through; spots part of the older cluster are underscored; the remaining spots constitute the younger cluster. Abbreviations: Pb_c = common lead, Pb* = radiogenic lead.

Spot	U	Th	Th/U	% $^{206}Pb_c$	$^{207}Pb^*/^{235}U$		$^{238}U/^{206}Pb$		$^{207}Pb^*/^{206}Pb^*$		ρ	$^{206}Pb/^{238}U$ age		$^{207}Pb/^{206}Pb$ age		%Disc.
1.C	27	5	0.18	3.45	1.397±	5.6	6.72±	2.8	0.0681±	4.8	0.49	895±	23	871±	100	-3
1.R	34	6	0.17	4.36	1.441±	5.1	6.75±	2.5	0.0705±	4.4	0.50	890±	21	944±	90	6
2.C	54	10	0.18	6.78	1.418±	4.6	6.91±	3.1	0.0710±	3.3	0.68	872±	25	958±	68	9
2.R	36	7	0.20	4.29	1.508±	6.2	7.23±	2.9	0.0791±	5.5	0.46	836±	22	1,173±	110	29
3.C	23	4	0.18	2.82	1.54±	6.8	6.97±	3.2	0.0778±	6.0	0.48	865±	26	1,143±	120	24
~~3.R~~	~~8~~	~~0~~	~~0.01~~	~~0.522~~	~~0.711±~~	~~13~~	~~12.65±~~	~~5.1~~	~~0.0653±~~	~~12~~	~~0.38~~	~~491±~~	~~24~~	~~783±~~	~~260~~	~~37~~
4.C	608	110	0.18	75.2	1.353±	1.5	6.942±	1.2	0.06810±	1.0	0.76	867.5±	10	872±	21	0
4.R	5	0	0.00	0.330	0.60±	17	14.20±	6.1	0.0617±	16	0.37	439±	26	663±	330	34
5.C	32	9	0.27	4.02	1.477±	6.3	6.79±	4.7	0.0727±	4.2	0.74	886±	39	1,007±	85	12
5.R	9	0	0.02	0.551	0.537±	14	13.70±	4.8	0.0534±	13	0.36	454±	21	346±	290	-31
6.C	28	6	0.23	3.52	1.432±	5.3	6.80±	2.7	0.0706±	4.6	0.51	885±	22	946±	94	6
6.R	10	0	0.01	0.603	0.535±	13	14.59±	4.5	0.0566±	12	0.36	427±	19	476±	260	10
~~7.C~~	~~36~~	~~6~~	~~0.16~~	~~4.03~~	~~1.212±~~	~~5.1~~	~~7.79±~~	~~2.5~~	~~0.0684±~~	~~4.5~~	~~0.48~~	~~779±~~	~~18~~	~~881±~~	~~92~~	~~12~~
~~7.R~~	~~9~~	~~0~~	~~0.04~~	~~0.559~~	~~0.74±~~	~~14~~	~~13.30±~~	~~5.8~~	~~0.0716±~~	~~13~~	~~0.42~~	~~467±~~	~~26~~	~~975±~~	~~260~~	~~52~~
8.C	25	4	0.18	3.07	1.375±	5.8	6.89±	2.8	0.0687±	5.1	0.49	874±	23	890±	110	2
8.R	15	0	0.01	0.912	0.668±	11	14.47±	4.1	0.0701±	10	0.38	431±	17	931±	210	54
~~9.C~~	~~27~~	~~6~~	~~0.22~~	~~3.66~~	~~1.524±~~	~~5.6~~	~~6.28±~~	~~2.8~~	~~0.0694±~~	~~4.8~~	~~0.49~~	~~952±~~	~~24~~	~~912±~~	~~100~~	~~4~~
9.R	28	4	0.15	3.33	1.304±	5.5	7.10±	2.7	0.0671±	4.8	0.49	850±	21	841±	100	-1
~~10.C~~	~~266~~	~~59~~	~~0.22~~	~~31.1~~	~~1.288±~~	~~3.0~~	~~7.367±~~	~~1.3~~	~~0.0688±~~	~~2.7~~	~~0.44~~	~~820.5±~~	~~10~~	~~893±~~	~~55~~	~~8~~
~~10.R~~	~~8~~	~~0~~	~~0.00~~	~~0.542~~	~~0.724±~~	~~13~~	~~12.99±~~	~~5.2~~	~~0.0682±~~	~~12~~	~~0.40~~	~~478±~~	~~24~~	~~876±~~	~~250~~	~~45~~

Table 2: geochronological data for sample 60414.102. Errors are given in one sigma percentages, except for the ages, which are given in one sigma absolutes. Rejected ages are struck through; spots part of the older cluster are underscored; the remaining spots constitute the younger cluster. Abbreviations: Pb_c = common lead, Pb* = radiogenic lead.

Spot	U	Th	Th/U	% $^{206}Pb_c$	$^{207}Pb^*/^{235}U$	$^{238}U/^{206}Pb$	$^{207}Pb^*/^{206}Pb^*$	ρ	$^{206}Pb/^{238}U$ age	$^{207}Pb/^{206}Pb$ age	%Disc.
11.R	2134	8	0.00	0.04	0.6192 ± 1.6	12.65 ± 1.4	0.05681 ± 0.70	0.90	490.4 ± 7	484 ± 15	-1
10.R	1385	5	0.00	0.05	0.61 ± 1.7	12.59 ± 1.4	0.05558 ± 0.91	0.84	492.6 ± 7	436 ± 20	-13
9.R	704	14	0.02	0.00	0.71 ± 1.9	11.98 ± 1.5	0.06142 ± 1.2	0.78	516.7 ± 7	654 ± 25	21
9.C	206	104	0.52	0.32	2.98 ± 2.0	4.246 ± 1.6	0.0917 ± 1.3	0.76	1363 ± 19	1,462 ± 25	7
8.R	89	0	0.00	0.49	0.64 ± 5.3	12.35 ± 1.8	0.0574 ± 5	0.35	501.9 ± 9	508 ± 110	1
8.C	139	25	0.18	--	1.65 ± 2.5	6.86 ± 1.7	0.0822 ± 1.8	0.68	877 ± 14	1,250 ± 36	30
7.R	1075	5	0.00	--	0.62 ± 1.8	12.9 ± 1.4	0.05797 ± 0.99	0.83	481.4 ± 7	529 ± 22	9
7.C	717	15	0.02	0.00	0.63 ± 1.9	13.32 ± 1.5	0.06052 ± 1.3	0.76	466.6 ± 7	622 ± 27	25
6.R	817	8	0.01	--	0.66 ± 1.8	12.28 ± 1.5	0.05891 ± 1.1	0.79	504.5 ± 7	564 ± 25	10
6.C	305	166	0.56	--	2.61 ± 1.8	4.825 ± 1.5	0.09143 ± 1	0.83	1214 ± 17	1,456 ± 19	17
5.R	219	108	0.51	0.03	2.97 ± 1.9	4.203 ± 1.6	0.09053 ± 1	0.84	1376 ± 19	1,437 ± 19	4
5.C	1055	65	0.06	--	0.7 ± 1.7	12.2 ± 1.4	0.06215 ± 0.85	0.86	507.9 ± 7	679 ± 18	25
4.C	319	155	0.50	--	2.72 ± 1.8	4.569 ± 1.5	0.09025 ± 0.87	0.87	1276 ± 18	1,431 ± 17	11
3.R	534	2	0.00	0.00	0.59 ± 2.0	13.39 ± 1.5	0.05723 ± 1.3	0.74	464.1 ± 7	501 ± 29	7
3.C	388	256	0.68	0.00	2.87 ± 2.0	4.349 ± 1.7	0.09055 ± 1	0.85	1334 ± 20	1,437 ± 20	7
2.R	443	2	0.00	0.17	0.58 ± 2.2	13.35 ± 1.5	0.05624 ± 1.6	0.68	465.6 ± 7	462 ± 36	-1
2.C	245	123	0.52	0.13	2.7 ± 1.8	4.597 ± 1.5	0.08997 ± 0.99	0.84	1269 ± 18	1,425 ± 19	11
1.R	492	2	0.00	0.00	0.57 ± 2.2	13.75 ± 1.5	0.05642 ± 1.6	0.69	452.4 ± 7	469 ± 34	4
1.C	203	105	0.54	--	2.84 ± 1.9	4.41 ± 1.6	0.09088 ± 1	0.83	1318 ± 18	1,444 ± 20	9
4.R	1024	3	0.00	--	0.63 ± 2.0	12.51 ± 1.5	0.05715 ± 1.3	0.75	495.9 ± 7	498 ± 29	0.322

Table 3: geochronological data for sample 63905B. Errors are given in one sigma percentages, except for the ages, which are given in one sigma absolutes. Abbreviations: Pb_c = common lead, Pb* = radiogenic lead.

Spot	U	Th	Th/U	% $^{206}Pb_c$	$^{207}Pb^*/^{235}U$	$^{238}U/^{206}Pb^*$	$^{207}Pb^*/^{206}Pb^*$	ρ	$^{206}Pb/^{238}U$ age	$^{207}Pb/^{206}Pb$ age	%Disc.
1	430	63	0.15	55.7	1.427 ± 2.0	6.623 ± 1.2	0.0686 ± 1.6	0.61	906 ± 10	886 ± 33	-2
2	597	382	0.64	76.1	1.419 ± 1.8	6.752 ± 1.2	0.06950 ± 1.4	0.65	890.3 ± 10	914 ± 28	3
3	1510	131	0.09	200	1.467 ± 1.5	6.485 ± 1.1	0.06902 ± 1.0	0.72	924.4 ± 9	899 ± 21	-3
14	690	125	0.18	88.2	1.417 ± 1.9	6.711 ± 1.2	0.06897 ± 1.4	0.64	895 ± 10	898 ± 29	0
15	866	89	0.10	115	1.499 ± 1.7	6.444 ± 1.2	0.07005 ± 1.2	0.69	930 ± 10	930 ± 25	0
4	388	111	0.29	50.6	1.437 ± 2.5	6.581 ± 1.2	0.0686 ± 2.1	0.50	912 ± 11	886 ± 44	-3
~~5~~	~~346~~	~~117~~	~~0.34~~	~~74.8~~	~~3.036 ± 1.7~~	~~3.975 ± 1.2~~	~~0.0875 ± 1.2~~	~~0.72~~	~~1447 ± 16~~	~~1,372 ± 23~~	~~-5~~
6	441	183	0.42	55.8	1.388 ± 1.9	6.786 ± 1.2	0.0683 ± 1.5	0.63	886 ± 10	878 ± 31	-1
7	647	432	0.67	82.6	1.387 ± 1.7	6.733 ± 1.1	0.06774 ± 1.3	0.67	892.6 ± 10	861 ± 26	-4
8	322	48	0.15	41.9	1.471 ± 2.7	6.597 ± 1.3	0.0704 ± 2.3	0.48	910 ± 11	940 ± 48	3
9	456	59	0.13	59.5	1.457 ± 2.2	6.572 ± 1.2	0.0694 ± 1.9	0.54	913 ± 10	911 ± 38	0
10	1420	221	0.16	182	1.412 ± 1.4	6.694 ± 1.1	0.06856 ± 0.87	0.79	897.5 ± 9	885 ± 18	-1
11	364	61	0.17	46.9	1.406 ± 2.5	6.67 ± 1.9	0.0680 ± 1.6	0.76	900 ± 16	870 ± 34	-3
12	437	77	0.18	58.1	1.495 ± 2.3	6.442 ± 1.3	0.0699 ± 1.9	0.56	930 ± 11	924 ± 38	-1
13	755	127	0.17	95.1	1.388 ± 1.6	6.829 ± 1.1	0.06877 ± 1.2	0.68	880.9 ± 9	892 ± 25	1

Table 4: geochronological data for sample 64501. Errors are given in one sigma percentages, except for the ages, which are given in one sigma absolutes. Rejected ages are struck through. Abbreviations: Pb_c = common lead, Pb* = radiogenic lead.

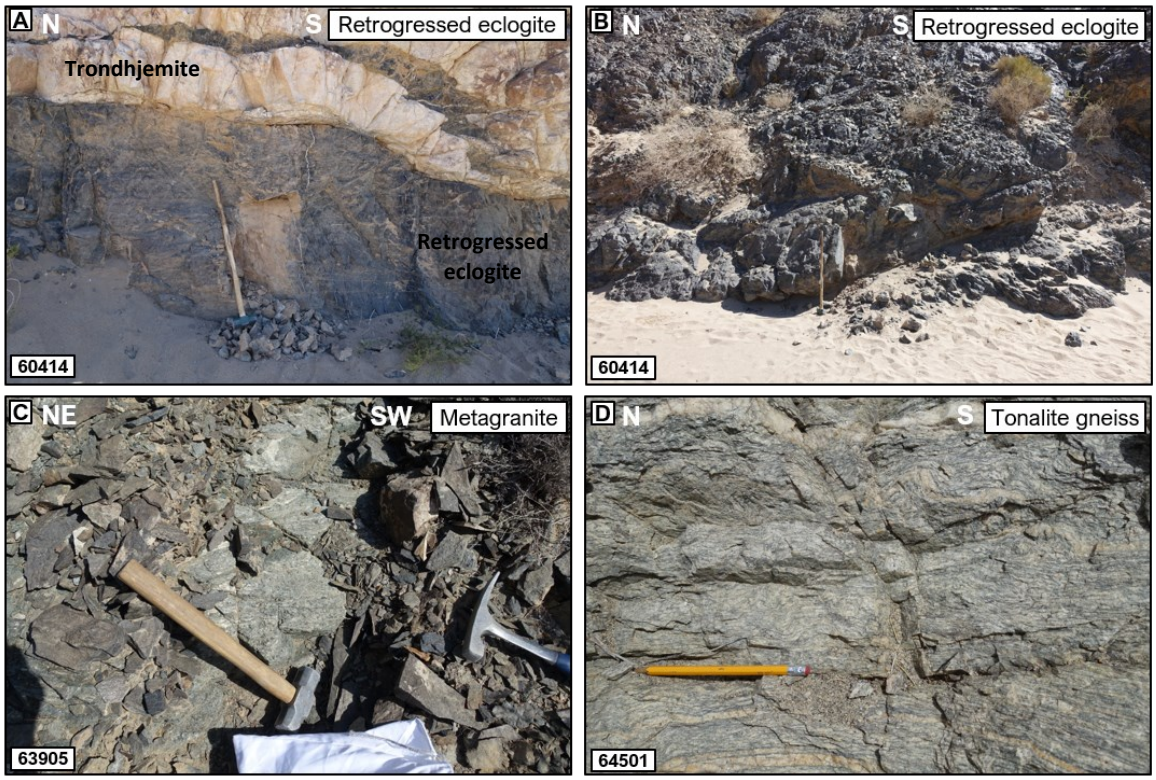

Figure 19. Outcrop photos of sampling locations. (A) Least retrogressed eclogite (60414), sledgehammer marks sampling location. (B) Amphibolitised eclogite (60414), sledgehammer marks sampling location. (C) Garnetiferous tonalite gneiss (63905), layers in middle of photo were sampled. (D) Tonalite gneiss (64877), sampled close to photographed area. Lineation dips into photo, degree of deformation may not be as apparent.

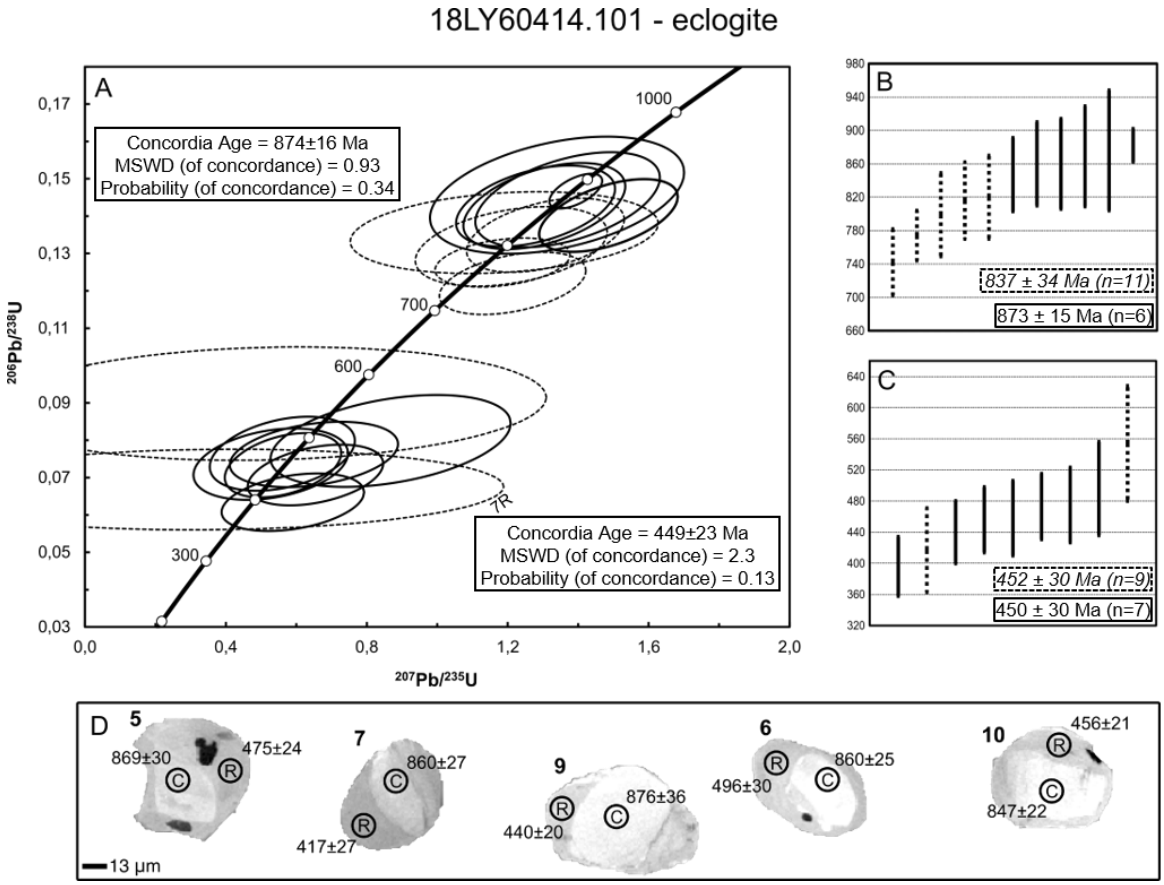

Figure 20. Geochronological data for 60414.101 (eclogite). Errors ellipses and error bars are 2σ. Errors of ages for individual spots are 1σ, whereas errors for Concordia and average ages are 95% confidence intervals. For the Concordia age, this includes the decay constant error. (A) Wetherill Concordia diagram with ages for main clusters. Solid ellipses were included in age determination, dotted ellipses were excluded. (B) $^{206}Pb/^{238}U$ age for spots from the upper cluster. Solid bars were included in age determination, dotted bars were excluded. Age in italics is $^{206}Pb/^{238}U$ age for all spots, age in regular font is $^{206}Pb/^{238}U$ age for selected spots (C) $^{206}Pb/^{238}U$ age for spots from the lower cluster. Solid bars were included in age determination, dotted bars were excluded. Age in italics is $^{206}Pb/^{238}U$ age for all spots, age in regular font is $^{206}Pb/^{238}U$ age for selected spots (D) Representative zircons with $^{206}Pb/^{238}U$ age (in Ma) for each spot; spots are 13 µm in diameter.

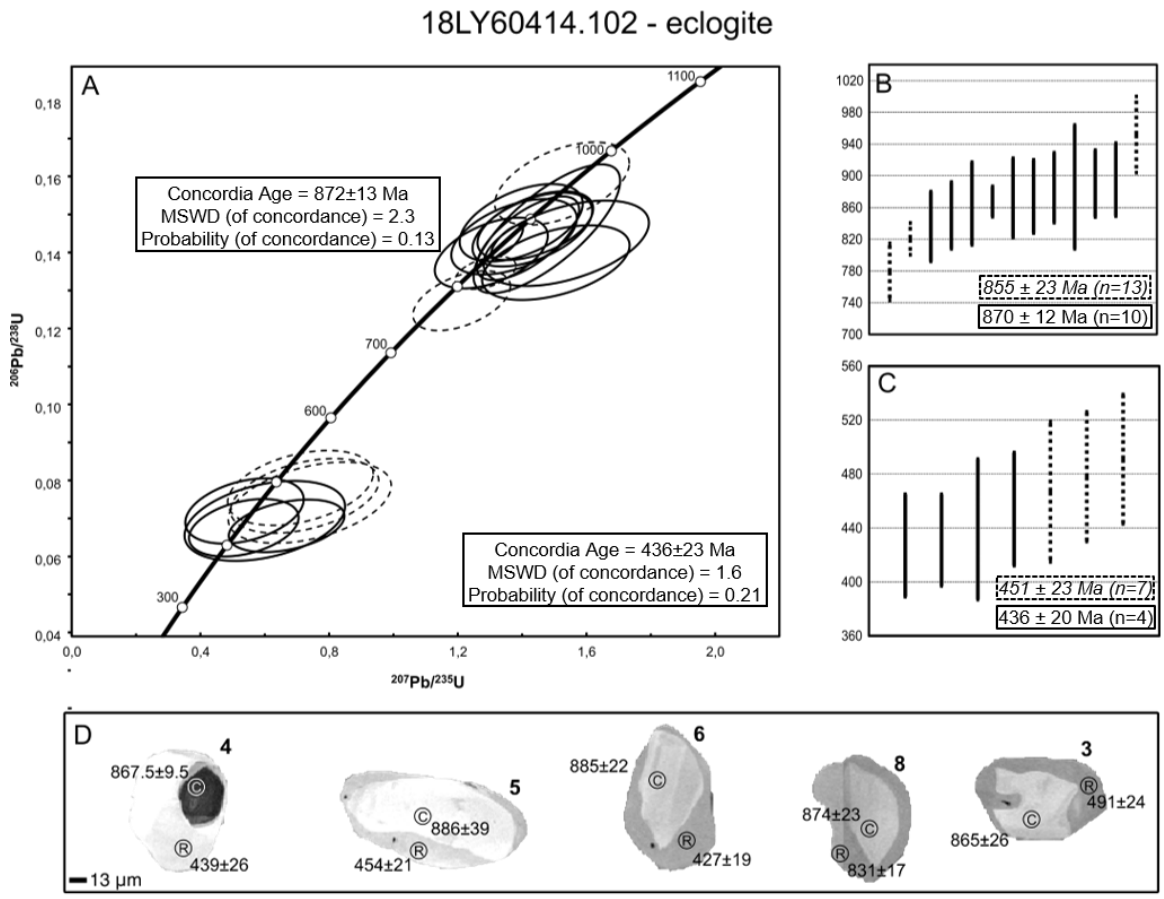

Figure 21. Geochronological data for 60414.102 (eclogite). Errors ellipses and error bars are 2σ. Errors of ages for individual spots are 1σ, whereas errors for Concordia and average ages are 95% confidence intervals. For the Concordia age, this includes the decay constant error. (A) Wetherill Concordia diagram with ages for main clusters. Solid ellipses were included in age determination, dotted ellipses were excluded (B) $^{206}Pb/^{238}U$ age for spots from the upper cluster. Solid bars were included in age determination, dotted bars were excluded. Age in italics is $^{206}Pb/^{238}U$ age for all spots, age in regular font is $^{206}Pb/^{238}U$ age for selected spots (C) $^{206}Pb/^{238}U$ age for spots from the lower cluster. Solid bars were included in age determination, dotted bars were excluded. Age in italics is $^{206}Pb/^{238}U$ age for all spots, age in regular font is $^{206}Pb/^{238}U$ age for selected spots. (D) Representative zircons with $^{206}Pb/^{238}U$ age for each spot (in Ma); spots are 13 µm in diameter.

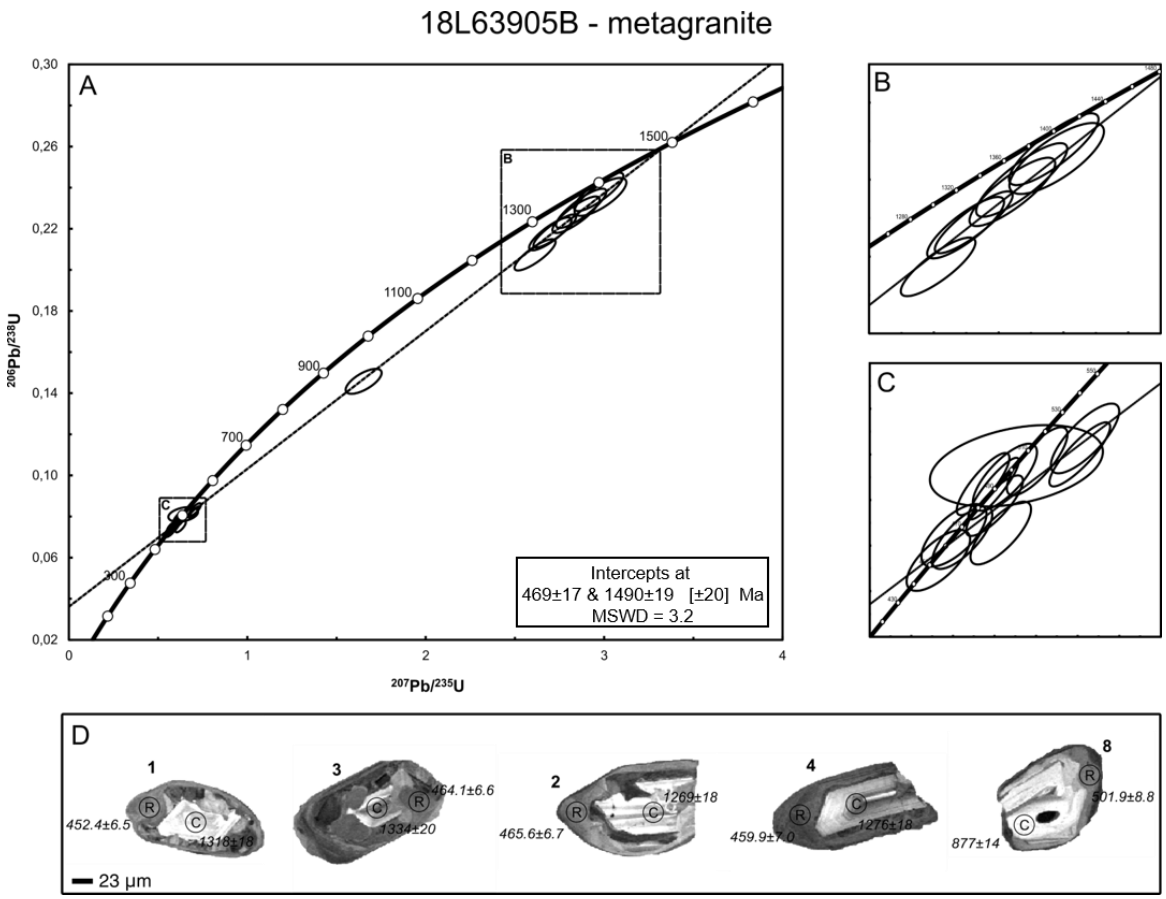

Figure 22. geochronological data for 63905B (granite gneiss). Errors ellipses are 2σ, whereas the errors of ages for individual spots are 1σ. The errors of the intercept ages are 95% confidence intervals. (A) Wetherill Concordia diagram with discordia line and intercept ages given. All spots were included for the age determination. (B) Close-up of upper cluster. (C) Close-up of lower cluster. (D) Representative zircons with $^{206}Pb/^{238}U$ age (in Ma) for each spot; spots are 24 µm in diameter.

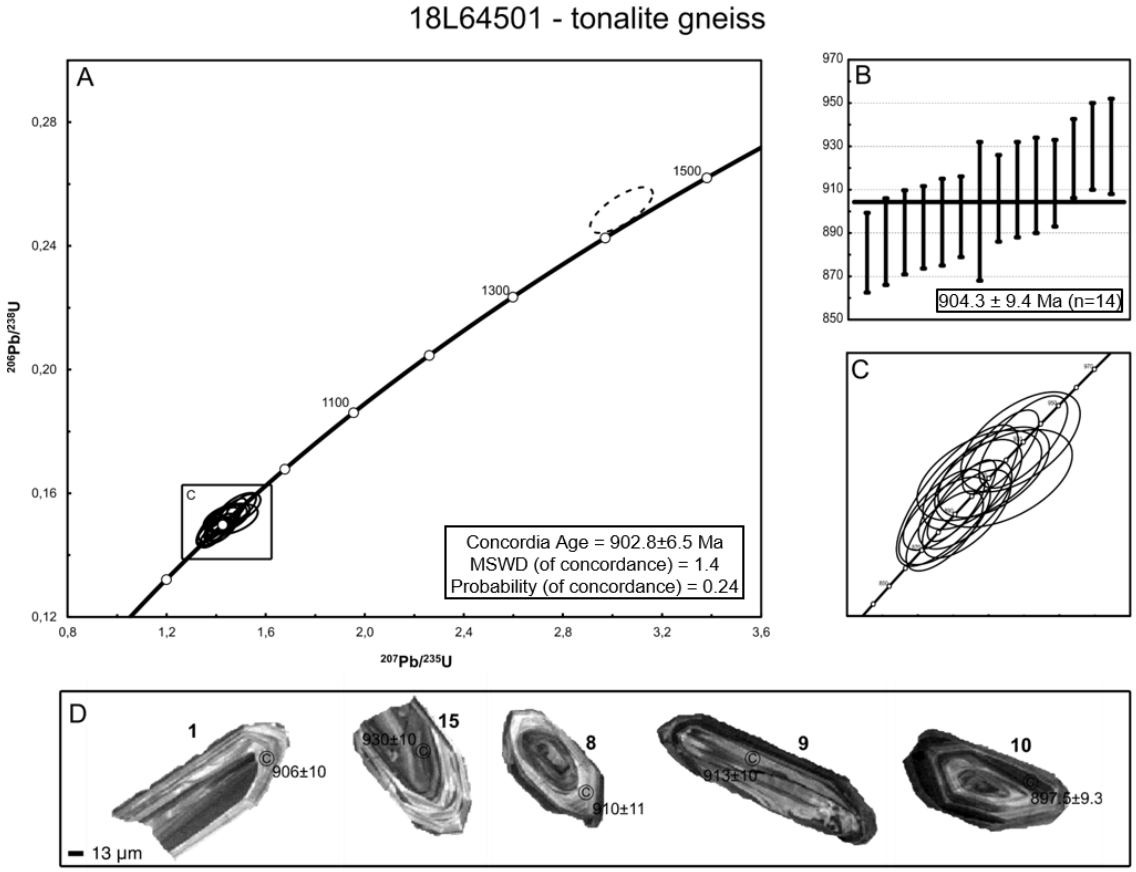

Figure 23. Geochronological data for 64501 (tonalite gneiss). Errors ellipses and error bars are 2σ. Errors of ages for individual spots are 1σ, whereas errors for Concordia and average ages are 95% confidence intervals. For the Concordia age, this includes the decay constant error. (A) Wetherill Concordia diagram with ages for main clusters. Solid ellipses were included in age determination, dotted ellipses were excluded. (B) $^{206}Pb/^{238}U$ age for selected spots from main cluster. (C) Close-up of main cluster. (D) Representative zircons with $^{206}Pb/^{238}U$ age (in Ma) for each spot; spots are 13 µm in diameter.

Chapter 8
Discussion

The structural and metamorphic evidence and available time constraints discussed herein are integrated in this chapter to reconstruct a P-T-D-t path. This process relies on the interpretation of the SHRIMP Zircon U-Pb ages and comparison with existing ages in the literature, to better understand the emplacement and deposition of the protoliths of the rocks in the metamorphic tectonite belt.

D5-D7 structures occur in Permian units, postdate Carboniferous-Permian basal conglomerate deposition and hence, correspond to a different tectonic event than the preceding structures. Therefore, the remainder of the discussion will be limited to D1-D4.

8.1 Integration of structural and metamorphic observations

8.1.1 *D1*

Little is known about S1 and it is unclear whether any of the assemblages in the eclogites formed coeval with D1. D1 could be coeval to assemblage 1 or 2 in the eclogites and represent (near-)peak-metamorphic or early retrogressive conditions, because D2 represents a retrogressive stage and is (sub-)coeval with assemblage 3 in the eclogites. This needs to be confirmed with further analyses of S1 inclusion trails.

8.1.2 *D2*

Based on optical petrography, D2 structures are approximately coeval with kyanite + garnet (+ rutile; Soldner, Štípská et al., 2020) as well as sillimanite, which formed after kyanite + garnet (Figure 24). Kyanite + garnet (+ rutile) is the highest-grade metamorphic assemblage observed in the metasedimentary rocks. These minerals may have initially formed during eclogite-facies metamorphism, but Solder, Štípská et al.'s (2020) pseudosection indicates that this assemblage and garnet's core and rim compositions rather correspond to upper amphibolite-facies conditions, at 8-

8.5 kbars, ~670 °C (Figure 25). These PT conditions approximately coincide with the lowest possible PT conditions under which this assemblage would be stable in an average metapelite composition (Yakymchuk et al., 2017). These conditions would be broadly equivalent to those estimated for assemblage 3 in the eclogites (Soldner, Štípská et al., 2020). Soldner, Štípská et al. (2020) furthermore indicated the existence of a ~8-13 Ma time-gap between assemblage 1 in the eclogites and the peak assemblage in the metasedimentary rocks. Therefore, the peak assemblage observed in the metasedimentary rocks is probably not contemporaneous with assemblage 1 in the eclogites, although garnet and kyanite may have already existed under eclogite-facies conditions.

The presence of syn-D2 sillimanite suggests D2 is either associated with conditions at the kyanite-sillimanite phase boundary, or with a transition across this boundary. As the former is rather rare (Whitney, 2002), it is more likely that D2 deformation is related to a large decrease in pressure and a small decrease in temperature (Figure 25). This is consistent with the abundance of symplectites in assemblage 3 of the eclogites, which commonly are interpreted as decompression indicators (Martin and Duchêne, 2015).

8.1.3 *D3*

Staurolite is consistently syn-D3, whereas andalusite is syn- to post-D3. For an average metapelite composition (Yakymchuk et al., 2017), these minerals do not occur together (Figure 25). This suggests that D3 is associated with a change in metamorphic conditions. Considering the clockwise trajectory indicated by the preceding assemblages and the relative growth relationships of staurolite and andalusite to S3, this most likely indicates a drop in temperature and to a lesser extent in pressure from the staurolite to andalusite stability field (Figure 25): from approximately 550-600 °C and 2-4 kbars to 500-550 °C and 2-3 kbars. This is consistent with Soldner, Štípská et al.'s (2020) PT estimates for their andalusite-bearing assemblage.

In order to fully interpret D3 structures, the F4 folds need to be unfolded. Since F4 folds are very tight, non-cylindrical, asymmetric (Figure 8) and since they may have undergone hinge

rotation, the orientations of D4 structures could not be unfolded on a stereonet. S4 crenulation cleavages generally dip north (Figure 8), which indicates that F4 folds were overturned to the south due to top-S shearing. L4 lineations predominantly have a north-north-westerly plunge (Figure 7) – these should lie in the plane folded by F4. Therefore, S3 would approximately be NNE-SSW-trending and NNW-dipping prior to F4 folding. F3 folds would be south-verging. F3 hinge lines would be shallowly plunging, with easterly and westerly plunge directions. Shearing indicators on D3 would predominantly indicate top-S, up-dip displacement, with some areas of top-N, down-dip displacement. This suggests that D3 was associated with an N-S compressive environment.

8.1.4 *D4*

D4 fabrics have only been observed in quartz schists and metabasites. In these rocks, S4 is not associated with any clear metamorphic index minerals but broadly indicates garnet-free, lower amphibolite to greenschist-facies conditions. This corresponds to <550 °C and <3 kilobars in an average metapelite (Figure 25).

8.2 Interpretation of geochronology

8.2.1 *Core and upper intercept ages*

Sample 63905B's upper intercept of 1490 ± 19 Ma is consistent with other Mesoproterozoic ages from this domain: He et al. (2018) documented a U-Pb zircon age of ~1550 Ma in granite gneiss, whereas Soldner, Yuan et al. (2020) describe a metagreywacke with an upper intercept age of 1461 ± 44 Ma. Many younger igneous units appear to have Mesoproterozoic inherited ages (this study; Soldner, Yuan et al., 2020). This reinforces the idea that parts of the metamorphic tectonite belt – primarily the metasedimentary rocks, as well as some of the metabasites and felsic orthogneiss - represent Mesoproterozoic crust. However, thus far only samples from domains G-I have been dated. It remains to be determined whether these observations are applicable to the metamorphic tectonite belt as a whole.

Sample 64501's Neoproterozoic age is consistent with ages determined for felsic orthogneiss elsewhere in the metamorphic tectonite belt (Soldner, Yuan et al., 2020; Saktura et al., 2017; Liu et al., 2011). As all earlier published ages were obtained in domain I and this study's sample is from domain G, these ages are compatible with models where these domains are one and the same, lying on either limb of an F4 fold (Figure 7). The protolith of the felsic orthogneiss in domain E, which is comparable to the gneisses in domains G and I, may have been emplaced during the same Neoproterozoic event. This is consistent with earlier models where the BOC is located at the Rodinian margin, either adjacent to the Tarim or Central Tianshan blocks (Soldner, Yuan et al., 2020 and references therein). Convergence-related rocks with similar ages are found in the Cathaysia block (Huang et al., 2019; Wang et al., 2013), the Central Tianshan (Huang et al., 2019; Zong et al., 2017) and the Yili block (Huang et al., 2019). In all these terranes, the early Neoproterozoic rocks were also interpreted as being related to the final stages of Rodinia's assembly, when these areas were situated at or near the peri-Rodinian margin. Notably, these areas would have recorded some of the last convergent activity during the assembly of Rodinia (e.g. Li et al., 2008).

The core ages of the eclogitic samples (874 ± 23 Ma; 872 ± 13 Ma) are consistent with zircon core ages from earlier studies (Soldner, Yuan et al., 2020; Saktura et al., 2017; Liu et al., 2011). These ages are compatible with models in which the felsic orthogneiss acted as a host for the eclogite's mafic protolith.

The eclogite samples and sample 63905B, which occurred in close association with an amphibolite, suggest that the metabasites in the tectonite belt may have at least two different protoliths: Mesoproterozoic and Neoproterozoic. Similarly, samples 63905B and 64501 indicate that the same applies to the felsic orthogneiss. However, there appears to be a clear distinction between the domains dominated by felsic orthogneiss and those dominated by metasedimentary rocks and metabasites: the former primarily yielded Neoproterozoic protolith ages, the latter Mesoproterozoic.

8.2.2 *Rim and lower intercept ages*

As for the rim ages, populations are very small and error margins are rather large, considering the small age differences between different PT stages. The results were not correlated with trace element geochemistry or *in-situ* observations. Thus, these inferences are only preliminary and insufficient for reliably separating different metamorphic stages. The rim ages will be discussed in order of decreasing age.

The 469 ± 17 Ma lower intercept of the granite gneiss (63905B) from domain H, lastly, appears rather old relative to earlier estimates of 453.5 ± 2.7 Ma and 452.8 ± 3.0 Ma (Soldner, Štípská et al., 2020) on near-peak-metamorphism in domain I. The error range of 63905B's lower intercept overlaps with this estimate, hence these two ages could still represent the same metamorphic event. However, this age is closer to Lu-Hf ages (461.9 ± 1.6 Ma and 462.0 ± 6.2 Ma) in Soldner, Štípská et al. (2020), interpreted as reflecting the onset of garnet growth during prograde metamorphism. Therefore, this age can either represent zircon growth or re-equilibration during prograde or peak-metamorphism.

The U-Pb zircon rim age of 449 ± 23 Ma in sample .101 is comparable to zircon rim ages obtained by Soldner, Yuan et al. (2020) and Saktura et al. (2017), as well as the Lu-Hf ages. The latter study interpreted their zircon rim ages as representing the onset of garnet growth, whereas peak metamorphism would have been represented by a ~453 Sm-Nd age. This interpretation would imply that these zircon rims grew or re-equilibrated during prograde metamorphism, which is common (Rubatto, 2017; Beckmann & Möller, 2018).

As .102 was largely retrogressed to amphibolite-facies assemblages (D3-D4), its slightly younger age than .101 of 436 ± 23 Ma may indicate zircon growth or re-equilibration during retrograde metamorphism. This is consistent with *in-situ* U-Pb monazite ages for retrograde metamorphism in the host rock (Soldner, Štípská et al., 2020). Their monazites are included in biotite and plagioclase, along with staurolite and kyanite inclusions. The monazite rims were in equilibrium with garnet rims and equilibrated at 500-600 °C, whereas the cores were in equilibrium with the garnet cores and equilibrated at 600-700 °C. Based on this textural relationship and

temperature estimates, this study is consistent with Soldner, Štípská et al.'s (2020) interpretation: the core age approximately represents this study's D2, whereas the rim age represents this study's D3. The garnet rims may have re-equilibrated during D3. The comparable P-T-t estimates for retrograde metamorphism in the eclogite and its host are compatible with models involving (I) tectonic juxtaposition of the eclogite with its present host before or during D3 or (II) *in-situ* eclogitisation. Both scenarios will be discussed below.

8.3 Tectonic implications

8.3.1 *Protolith*

The observed crosscutting field relationships are consistent with the zircon U-Pb ages in this study. Combined, they suggest that the metasedimentary rocks and most metabasites represent Mesoproterozoic crust that most likely formed part of Rodinia (Soldner, Yuan et al., 2020). During the amalgamation of Rodinia, these rocks would have constituted the host rocks for the protoliths of the felsic orthogneiss and the mafic protoliths of the eclogites (Soldner, Yuan et al., 2020). The eclogite most likely represents mafic dyke(s) or sill(s) emplaced not long after the emplacement of the felsic orthogneiss's protoliths. The eclogites cannot represent xenoliths brought up by the intruding protolith of the felsic orthogneiss, since they are hosted by both meta-igneous and meta-sedimentary rocks. Furthermore, the emplacement age postdates that of the felsic orthogneiss's protolith. As the eclogites define a single trail of closely spaced small, elongated bodies along the dominant S3 foliation, the eclogite may comprise one single, boudinaged dyke or sill. Soldner, Štípská et al. (2020) claim they observed several additional amphibolitised eclogitic boudins positioned perpendicular to the strike from the main trail of eclogite bodies. If correct, this would suggest that the extent of eclogite may have been wider and larger than discussed herein.

8.3.2 *Prograde metamorphism*

Since D3 fabrics are preserved in the eclogites and its host, any potential unshared structural history must have occurred S3 formation. However, there currently is no evidence for structural juxtaposition along shear zones or through melanging (breaking up and mixing of rock units through structural activity such as transposition and shearing) during D1 or D2. Because the distribution of units and layering remained coherent and continuous on the scale of the mapping area, significant structural mixing through upright, crustal scale folding and transposition is considered unlikely, as was postulated by Soldner, Štípská et al. (2020). An alternative scenario involving major uplift of the eclogite with respect to the host rocks by means of narrow shear zones and/or a mega-scale isoclinal antiform (Soldner, Štípská et al., 2020; Štípská et al., 2004), such that the eclogite was juxtaposed with its immediate lower-grade country rocks is also difficult to conceive, considering the structural evidence reported in this study, which has not identified any of the required structures. Thus, there is no evidence for a structural incorporation of the eclogite into the orthogneiss and meta-pelitic host rocks (scenario I). This suggests that the eclogite-facies fabrics were developed in situ (scenario II). If correct, amphibolite lenses within domain G & I represent fully retrogressed eclogites or may not have had suitable compositions for developing eclogite-facies assemblages. Similarly, the metasedimentary lenses within domain G & I thus probably were also fully retrogressed. However, there currently is no evidence for eclogite-facies metamorphism in any domains other than G & I; the other domains either are fully re-equilibrated / retrogressed or have different metamorphic histories until their eventual structural juxtaposition with the eclogite-hosting domains.

8.3.3 *Retrograde history*

No evidence exists for differential return flow of the eclogite. Such a process would have been initiated by choking the subduction channel and driving differential uplift of rocks within it, following the progressive subduction of the continental terrane. The entrance of a buoyant terrane

into the subduction channel is commonly associated with slab break-off or the delamination of parts of the lithospheric mantle (Garzanti et al., 2018 and references therein).

This study has not identified any major tectonostratigraphic discontinuities that could represent a suture in the studied area, hence all rocks should have been situated on the same plate during convergence. Furthermore, D3 and D4 fabrics are found across the area. It is unlikely that the area represents the base of the overlying plate: in this case, these rocks would likely have undergone partial melting due to isotherm relaxation and would commonly not have undergone rapid decompression. Therefore, the whole metamorphic tectonite belt represents part of the down-going plate. This whole area would have undergone a clockwise PT path, characterised by a large decrease in pressure and a small temperature decrease. This was followed by uplift and exhumation along a relatively hot geotherm. After D4, the area is situated at a depth of <3 kbars pressure, corresponding to a position in the upper crust.

Deformation stages D2-D4 all relate to the eclogite's uplift and exhumation. D1 may also relate to this, but this is uncertain until confirmed by S1i inclusion analysis. During D2, shortening was sub-parallel to compositional layering, whereas D3 & D4 are consistent with N-S shortening, sub-perpendicular to compositional layering. Without clear refolding relationships, it is unclear whether F3 folds may have refolded F2 folds. Shearing probably happened after the F3 folds locked up and strain became more localised, locally forming north-normal and south-reverse narrow shear zones.

D4 structures are south-verging, whereas D3 structures are south-verging prior to refolding (Figure 5). Folds and shear zones in a subduction channel generally are oriented sub-parallel to the orientation of the subduction channel and have a vergence opposite to the dip of the subduction channel (e.g. Lamont et al., 2020; Guillot et al., 2009 and references therein; Ernst, 2005). Therefore, D3 & D4 folding suggests that the down-going plate was being subducted towards the north during the Ordovician-Devonian (Figure 26). The upper plate would be represented by the northern parts of the Huaniushan-Shuangyingshan terrane (Figure 2). This implicates a suture north of the eclogite, which has not been observed by this study. The location of this suture should be constrained through further mapping.

Multiple tectonic processes have been invoked for eclogite exhumation, including core complexes (e.g. Baldwin et al., 2004), diapirism (e.g. Chatterjee & Jagoutz, 2015; Little et al., 2011), vertical extrusion (Štípská et al., 2004; Skrzypek, Štípská et al., 2011) and wedge extrusion (Kurz and Froitzheim, 2002; Möller et al., 2015). Testing and invoking any of these models requires a larger, orogen-wide consideration of all observations and relationships, which this study does not cover. At smaller scales, many of these models may produce similar structures, which leave them difficult to separate without additional evidence. Furthermore, the small-scale kinematic observations made by this study may not necessarily reflect large scale geodynamic processes. For example, uplift in an extruding wedge may be associated with local extensional structures in a regional compressive setting (Searle et al., 2004).

However, certain models are not supported by the present observations. Diapirism necessitates a density inversion, for example through the obduction of an ophiolite above the subducted margin (Little et al., 2011). No such juxtaposition has been observed in the Gubaoquan area. A core complex model is unlikely, since these are associated with sub-horizontal fabrics and regional extension during exhumation, which have not been documented in this study (Baldwin et al., 2004). No evidence exists for exhumation by ductile spreading and mid-crustal thinning following vertical extrusion by means of crustal-scale upright folding (Štípská et al., 2004), as this is associated with sub-horizontal fabrics. Furthermore, both D3 & D4 are associated with inclined folding and the observed lateral continuity of compositional layering and units renders the structural juxtaposition of layers from different depth along small-scale structures unlikely in general (c.f. Skrzypek, Štípská et al., 2011).

The widespread compressive fabrics (D3, D4) and local extensional fabrics (D2, D3) could be consistent with an extrusion wedge (Figure 26). However, this model necessitates observing two coevally active bounding faults, which juxtapose a higher-grade wedge with lower-grade rocks on either side (Kurz and Froitzheim, 2002; Möller et al., 2015). Such relationships have not been observed by this study and hence, this model cannot be invoked with certainty.

Regardless, all tectonic models necessitate erosion and/or structural extension for exhumation to occur. The observed PT-t-D path of a large pressure and small temperature decrease

during D2-D3 requires removal of part of the overburden during deformation. As D3 shearing indicates local extension, exhumation may have been partially achieved through this (e.g. detachment faulting). No syn-tectonic Late Ordovician-Silurian sedimentary deposits have been observed in the area. Further studies on the regional tectonic evolution should better constrain the responsible mechanisms.

Both D4 & D5 are associated with greenschist-facies conditions, suggesting most of the area was situated at these conditions until the next tectonic stage. The Permian conglomerate observed in this study and Carboniferous-Triassic deposits observed elsewhere (Li, 2019; Cleven et al., 2018) suggest exhumation to surface conditions of the rocks in this area at this time. This is consistent with detrital zircons in a Permian-Triassic quartzite from the northern parts of the Shuangyingshan-Huaniushan unit, which nearly exclusively yielded Ordovician-Silurian ages (Cleven et al., 2018).

8.3.4 *Ordovician-Silurian magmatism*

The abundance of hornblende and mafic enclaves suggests that these granitoids are I type granites and that they (partially) have a mantle source (Barbarin, 2005; Chappel & White, 2001; Clemens et al., 2011; Niu et al., 2013; Pearce, 1996)). This is consistent with geochemical data on this intrusion from Mao, Xiao, Fang et al (2020), which indicate that these rocks have consistent I-type geochemical characteristics (Na > 3.2 wt-%, A/CNK < 1.1 m-%; Chappel & White, 2001). The D4 fabrics in the intrusions suggest that the rocks were emplaced in an active compressive tectonic environment. Their published emplacement ages (~424-442 Ma; Mao 2008; Mao, Xiao, Fang et al., 2012; Saktura et al., 2017) indicate they intruded over a protracted period. Their oldest emplacement age (~442 Ma) contradicts with the observed crosscutting relationships, as these indicate that the intrusions postdate D3 (~436-429 Ma). This suggests that the emplacement of the intrusion may have started during D3, whereas the present crosscutting relationship with D4 could have been established at the end of emplacement. However, Mao's (2008) age may not be reliable (see Lithostratigraphic architecture). Additional geochronology should resolve this.

The observed relationships put the present arc interpretations of these granitoids into question. If they were arc granitoids (Saktura et al., 2017; Mao et al., 2012b; Liu et al., 2011), one would expect a substantial gap in location to exist between the site of the arc granitoids and the exhumation site of the eclogite and enveloping rocks of the subduction complex, corresponding to the initial arc-trench gap, which could be hundreds of kilometres (Dickinson, 1973). To have arc granitoids intruding the eclogite-bearing rocks, the arc had to have migrated towards the trench, due to slab rollback or terrane accretion with subduction step-back, after the eclogite was incorporated into the now abandoned, early part of the subduction complex and partially exhumed. A new subduction complex would have formed further outboard of the migrated arc. No evidence of such a process is preserved. A post-collisional setting (Soldner, Štípská et al., 2020 and references therein) is also unlikely since the rocks are strongly deformed in places.

Instead, a scenario of slab break-off related magmatism is proposed. Slab break-off is often associated with continental subduction followed by bimodal syn-tectonic, linear intrusions that are emplaced close to the suture, parallel to the structural grain of the orogen (Whalen et al., 2006; von Blanckenburg and Davies, 1995; Davies and von Blanckenburg, 1995). These intrusions have at least in part a mantle component (Whalen et al., 2016). The Ordovician-Silurian intrusions have all these characteristics (see Lithostratigraphic architecture; Mao, Xiao, Fang et al, 2012). However, further petrographic, geochemical and isotopic analysis should confirm this.

8.3.5 *Silurian-Devonian magmatism*

The Silurian-Devonian intrusions are only slightly younger than the Ordovician-Silurian intrusions. They do have I-type granite characteristics but are post-tectonic. These granites represent the last major event in this area, until the area was (partially) exhumed in the late Carboniferous, early Permian. Hence, these granites probably are unrelated and represent a different tectonic setting than the preceding magmatism. Understanding their petrogenesis and setting needs further petrographic, geochemical and isotopic analysis combined with studies of the regional tectonic evolution.

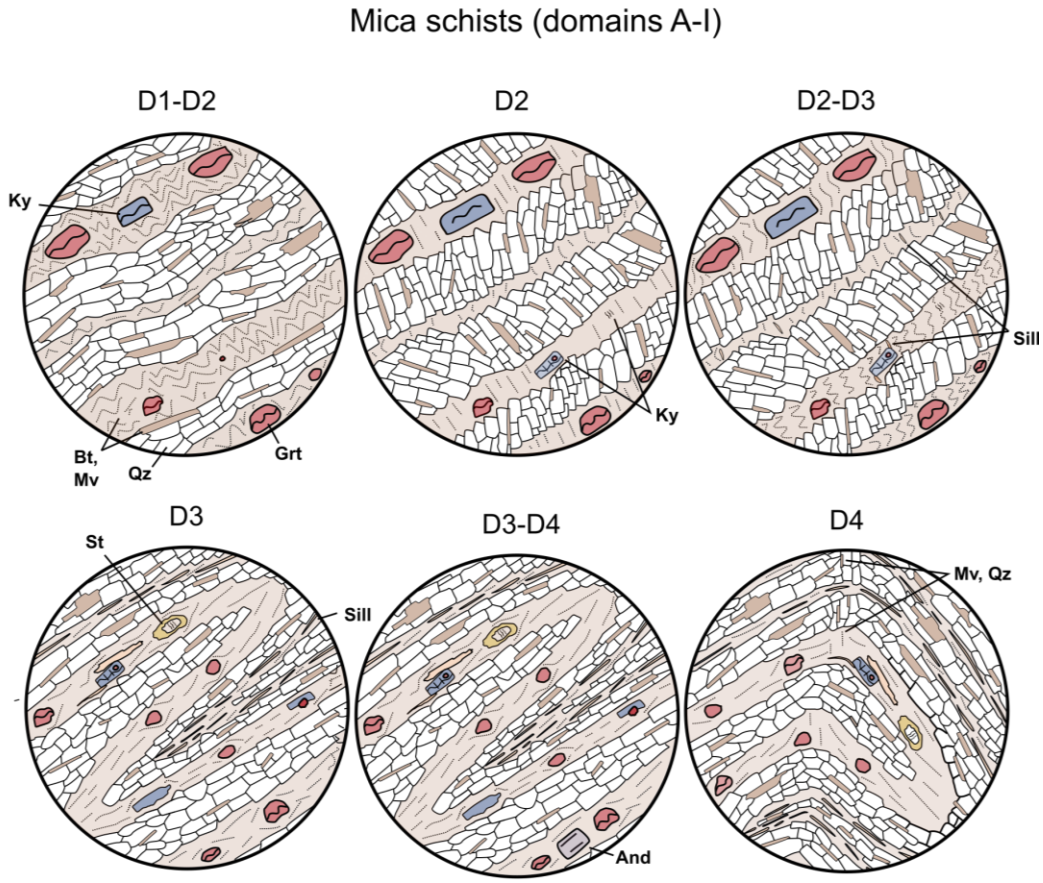
Mica schists (domains A-I)
D1-D2
D2
D2-D3
Ky
Ky
Sill
Bt,
Mv
Qz
Grt
D3
D3-D4
D4
St
Sill
Mv, Qz
And

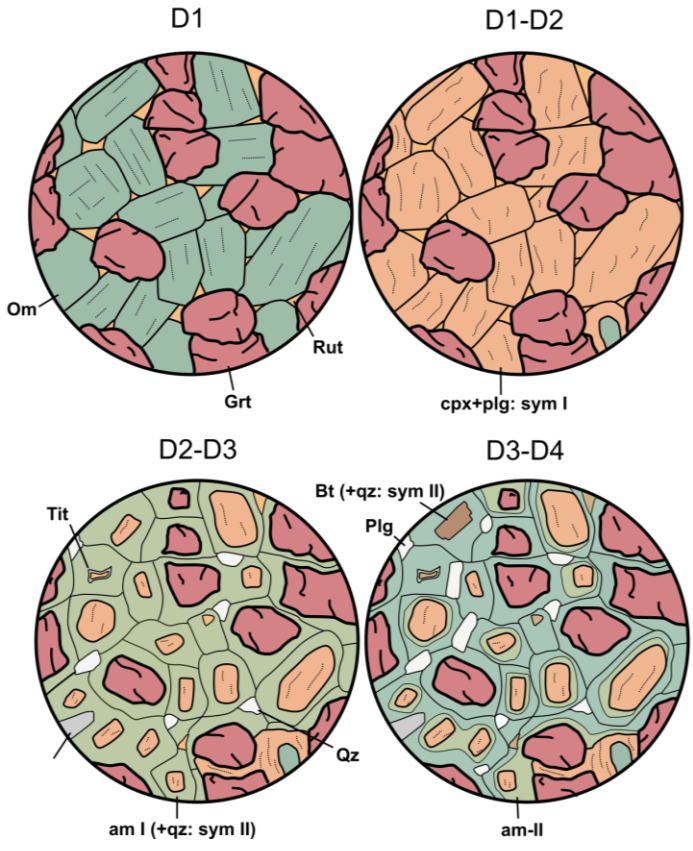
Eclogites (domain I)
D1
D1-D2
Om
Rut
Grt
cpx+plg: sym I
D2-D3
D3-D4
Bt (+qz: sym II)
Tit
Plg
Qz
am I (+qz: sym II)
am-II

Figure 24, previous page: summative diagram of the structures and metamorphic assemblages observed in thin section and in the field, for A: the eclogite in domain I and B: the metasediments across all domains. In the metasediments, garnet and kyanite developed pre- to syn-D2; sillimanite syn- to post-D2, staurolite syn-D3, andalusite syn- to post-D3 and white mica syn-D4. The eclogites show how eclogite-facies assemblages are retrogressed to clinopyroxene-, amphibole-, biotite-and quartz-bearing assemblages, but generally develop little to no fabric.

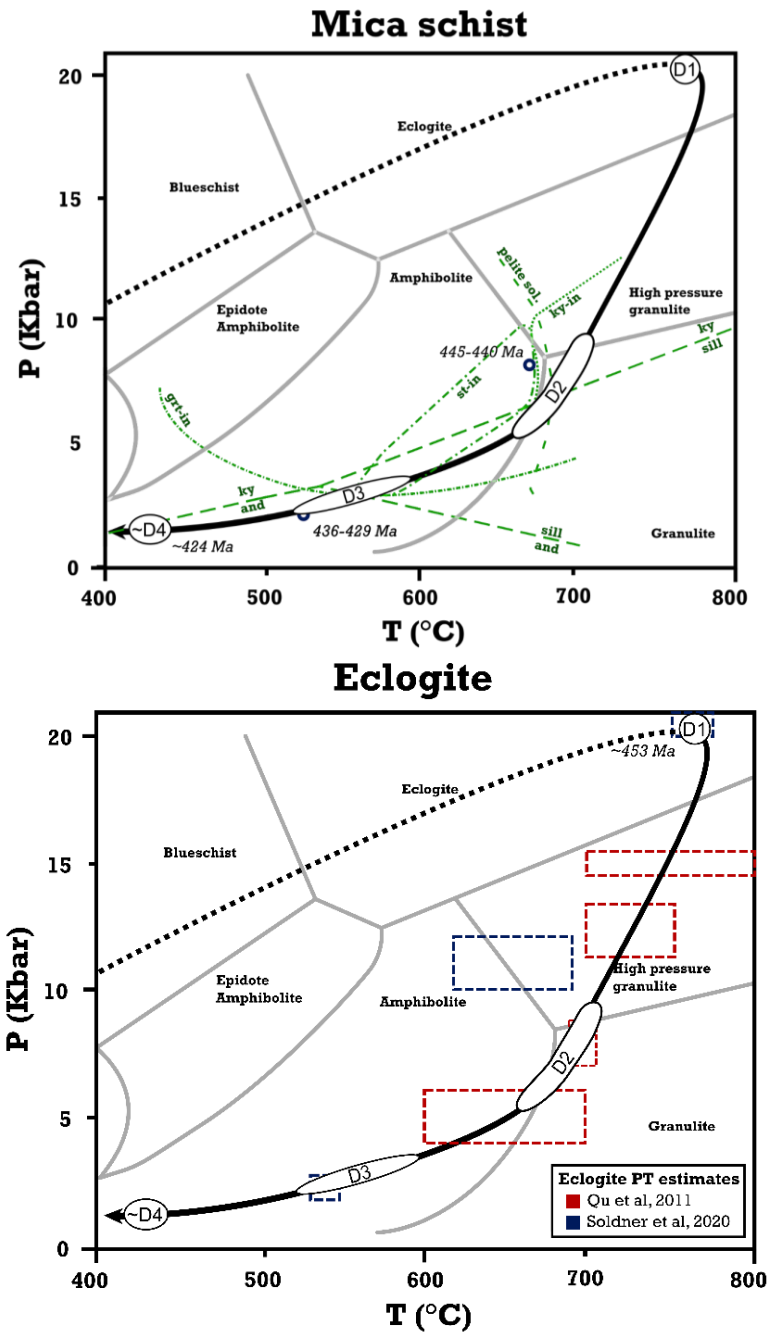

Figure 25: P-T-t-D diagrams for A: the metasediments across all domains and B: the eclogites in domain I. The eclogite and its host underwent a clockwise metamorphic path, associated with prograde metamorphism along a cold geotherm, up to eclogite-facies conditions. Subsequently, the area underwent a rapid decrease in pressure and a limited decrease in temperature, leading to HT-LP amphibolite-facies conditions. At D4, the area was under greenschist-metamorphic conditions. All mineral observations are from this study. Ages for deformation stages from Soldner, Štípská et al., 2020; average metapelite mineral stability & solidus data (green) from Yakymchuk et al. (2017); eclogite PT estimates in red from Qu et al. (2011) and in blue from Soldner, Štípská et al. (2020); facies boundaries from Sajeev & Santosh (2006).

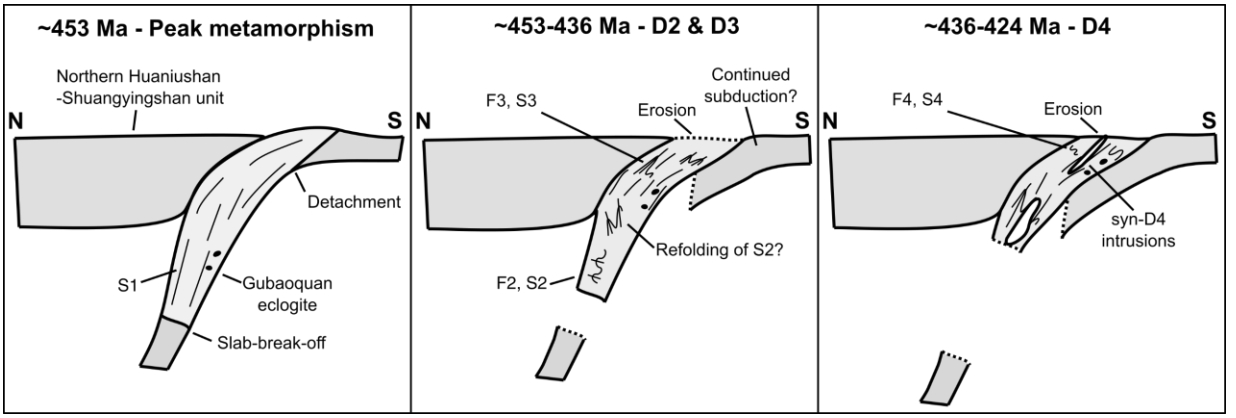

Figure 26: summative diagram of the suggested tectonic model. After slab break-off at ~453 Ma, the eclogite was uplifted and exhumed in an extruding-wedge-type setting, associated with a major pressure decrease and a limited temperature decrease. D2 and D3 developed, whilst the area was under HT-LP amphibolite-facies conditions. After further uplift and exhumation, the eclogite and its host reached greenschist-facies conditions. Several syn-tectonic I-type intrusions were emplaced during D4.

Chapter 9
Conclusion

The metamorphic tectonite belt hosting the Gubaoquan eclogites consists of several domains that are separated by shear zones and/or intrusions. Two types of domains can be identified, based on the relative dominance of either felsic orthogneiss or metasediments and metabasites. Preliminary U-Pb geochronology results suggest that the protoliths of the felsic orthogneiss were largely emplaced during the Neoproterozoic, whereas the metasediments and metabasites primarily have Mesoproterozoic protolith ages. The protolith of the Gubaoquan eclogite is comprised of one or several boudinaged Neoproterozoic mafic dykes or sills, hosted in a structural domain mainly composed of felsic orthogneiss. The mafic protolith of the Gubaoquan eclogite underwent *in-situ* eclogite-facies metamorphism.

The area has been subjected to a complicated, multi-stage deformation history, which led to significant N-S shortening and local extension. The area is strongly deformed and dominated by a steeply N-dipping E-W-trending S3 fabric. F3 folds were asymmetric, such that the distribution of units and layering was preserved on map-scale. D3 fabrics nearly entirely obliterated D2 and D1 structures and metamorphic assemblages, except in F3 fold hinges (S2) or as inclusion trails and mineral inclusions in porphyroblasts (S1, S2). Subsequent E-W-trending, steeply N-inclined, doubly plunging F4 folds refold F3 folds (Figure 24).

The metamorphic tectonite belt underwent a clockwise PT trajectory between ~470-420 Ma, characterised by eclogite-facies peak metamorphism, a large decrease in pressure and small decrease in temperature leading to amphibolite-facies conditions, followed by greenschist-facies metamorphism (Figure 25). Most eclogite was overprinted by retrograde assemblages, except in the cores of certain boudins. The S1 fabric in the metasediment might represent (near-)peak-metamorphic conditions. However, this needs to be confirmed with further analyses of S1 inclusion trails.

These observations indicate that the metamorphic tectonite belt hosting the Gubaoquan eclogite represents Meso-/Neo-Proterozoic crust that underwent Ordovician-Silurian, north-directed subduction to various depths and collision-related tectonism (Figure 26). This was followed by detachment from

the down-going slab, probably due to slab break-off, and incorporation into an orogenic wedge. Slab break-off was associated with the emplacement of several syn-tectonic granitoids with I-type characteristics. Extruding-wedge-type exhumation and overburden removal uplifted and exhumed the area to <3 kbars, or greenschist-facies conditions. Continental subduction possibly continued until the emplacement of the Silurian-Devonian granitoids. Afterwards, the area was relatively tectonically quiescent until the Carboniferous-Triassic, when the area was exhumed to the surface.

Lastly, this study demonstrated the importance of extensive fieldwork and optical petrography. Without, many of the structural relationships in this study would have gone unnoticed, leading to false assumptions and incorrect tectonic models. This is particularly important in largely retrogressed areas such as Gubaoquan and other continental eclogites, where insights into an area's deformation history may have only been preserved in porphyroblasts. This also implies that many retrogressed areas may have a more intricate P-T-t-D history than is presently known.

References

Agrawal, S., Guevara, M., & Verma, S. P. (2008). Tectonic discrimination of basic and ultrabasic volcanic rocks through log-transformed ratios of immobile trace elements. *International Geology Review*, 50(12), 1057-1079.

Ao, S. J., Xiao, W. J., Han, C. M., Li, X. H., Qu, J. F., Zhang, J. E., ... & Tian, Z. H. (2012). Cambrian to early Silurian ophiolite and accretionary processes in the Beishan collage, NW China: implications for the architecture of the Southern Altaids. *Geological Magazine*, 149(4), 606-625.

Baldwin, S. L., Monteleone, B. D., Webb, L. E., Fitzgerald, P. G., Grove, M., & Hill, E. J. (2004). Pliocene eclogite exhumation at plate tectonic rates in eastern Papua New Guinea. *Nature*, 431(7006), 263-267.

Barbarin, B., 2005. Mafic magmatic enclaves and mafic rocks associated with some granitoids of the central Sierra Nevada batholith, California: nature, origin, and relations with the hosts. *Lithos* 80, 155–177.

Beckman, V., & Möller, C. (2018). Prograde metamorphic zircon formation in gabbroic rocks: The tale of microtextures. *Journal of Metamorphic Geology*, 36(9), 1221-1236.

Black, L. P., Kamo, S. L., Allen, C. M., Aleinikoff, J. N., Davis, D. W., Korsch, R. J., & Foudoulis, C. (2003). TEMORA 1: a new zircon standard for Phanerozoic U–Pb geochronology. *Chemical geology*, 200(1-2), 155-170.

von Blanckenburg, F., & Davies, J. H. (1995). Slab breakoff: a model for syncollisional magmatism and tectonics in the Alps. *Tectonics*, 14(1), 120-131.

Carson, C. J., Ague, J. J., Grove, M., Coath, C. D., & Harrison, T. M. (2002). U–Pb isotopic behaviour of zircon during upper-amphibolite facies fluid infiltration in the Napier Complex, east Antarctica. *Earth and Planetary Science Letters*, 199(3-4), 287-310.

Chatterjee, N., & Jagoutz, O. (2015). Exhumation of the UHP Tso Morari eclogite as a diapir rising through the mantle wedge. *Contributions to Mineralogy and Petrology*, 169(1), 3.

Chappell, B. W., & White, A. J. (2001). Two contrasting granite types: 25 years later. *Australian journal of earth sciences*, 48(4), 489-499.

Clemens, J. D., Stevens, G., & Farina, F. (2011). The enigmatic sources of I-type granites: the peritectic connexion. *Lithos*, 126(3-4), 174-181.

Cleven, N., Lin, S., Davis, D. W., Xiao, W., & Guilmette, C. (2016). Elucidating tectonic events and processes from variably tectonized conglomerate clast detrital geochronology: Examples from the

Permian Hongliuhe Formation in the southern Central Asian orogenic Belt, NW China. *Tectonics*, 35(7), 1626-1641.

Cleven, N., Lin, S., Guilmette, C., Xiao, W., & Davis, B. (2015). Petrogenesis and implications for tectonic setting of Cambrian suprasubduction-zone ophiolitic rocks in the central Beishan orogenic collage, Northwest China. *Journal of Asian Earth Sciences*, 113, 369-390.

Cleven, N. R., Lin, S., Xiao, W., Davis, D. W., & Davis, B. (2018). Successive arc accretion in the southern Central Asian orogenic belt, NW China: Evidence from two Paleozoic arcs with offset magmatic periods. *GSA Bulletin*, 130(3-4), 537-557.

Cooke, R. A., & O'Brien, P. J. (2001). Resolving the relationship between high P–T rocks and gneisses in collisional terranes: an example from the Gföhl gneiss–granulite association in the Moldanubian Zone, Austria. *Lithos*, 58(1-2), 33-54.

Corfu, F., Hanchar, J. M., Hoskin, P. W., & Kinny, P. (2003). Atlas of zircon textures. *Reviews in mineralogy and geochemistry*, 53(1), 469-500.

Davies, J. H., & von Blanckenburg, F. (1995). Slab breakoff: a model of lithosphere detachment and its test in the magmatism and deformation of collisional orogens. *Earth and Planetary Science Letters,* 129(1-4), 85-102.

Dickinson, W. R. (1973). Widths of modern arc-trench gaps proportional to past duration of igneous activity in associated magmatic arcs. *Journal of Geophysical Research*, 78(17), 3376-3389.

Downey, M. W., Lin, S., Böhm, C. O., & Rayner, N. M. (2009). Timing and kinematics of crustal movement in the Northern Superior superterrane: Insights from the Gull Rapids area of the Split Lake Block, Manitoba. *Precambrian Research*, 168(1-2), 134-148.

Ernst, W. G. (2005). Alpine and Pacific styles of Phanerozoic mountain building: subduction-zone petrogenesis of continental crust. *Terra Nova*, 17(2), 165-188.

Gansu Bureau of Geology and Mineral Resources (Gansu BGMR) (1966). *Regional Geology of the Gansu Jiuquan Region*. Geological Publishing House, Beijing, p.157 (in Chinese with English abstract)

Garzanti, E., Radeff, G., & Malusà, M. G. (2018). Slab breakoff: A critical appraisal of a geological theory as applied in space and time. *Earth-Science Reviews*, 177, 303-319.

Gillespie, J., Glorie, S., Xiao, W., Zhang, Z., Collins, A. S., Evans, N., ... & De Grave, J. (2017). Mesozoic reactivation of the Beishan, southern Central Asian Orogenic Belt: Insights from low-temperature thermochronology. *Gondwana Research*, 43, 107-122.

Govindaraju, K. (1995). 1995 working values with confidence limits for twenty-six CRPG, ANRT and IWG-GIT geostandards. *Geostandards Newsletter*, 19, 1-32.

Guillot S., Hattori K., Agard P., Schwartz S., Vidal O. (2009) Exhumation Processes in Oceanic and Continental Subduction Contexts: A Review. In: Lallemand S., Funiciello F. (eds) *Subduction Zone Geodynamics. Frontiers in Earth Sciences.* Springer, Berlin, Heidelberg.

He, Z. Y., Klemd, R., Yan, L. L., & Zhang, Z. M. (2018). The origin and crustal evolution of microcontinents in the Beishan orogen of the southern Central Asian Orogenic Belt. *Earth-Science Reviews*, 185, 1-14.

Hong, D., Zhang, J., Wang, T., Wang, S., & Xie, X. (2004). Continental crustal growth and the supercontinental cycle: evidence from the Central Asian Orogenic Belt. *Journal of Asian Earth Sciences*, 23(5), 799-813.

Huang, Z., Yuan, C., Long, X., Zhang, Y., & Du, L. (2019). From Breakup of Nuna to Assembly of Rodinia: A Link Between the Chinese Central Tianshan Block and Fennoscandia. *Tectonics*, 38(12), 4378-4398

Janoušek, V., Farrow, C. M. & Erban, V. 2006. Interpretation of whole-rock geochemical data in igneous geochemistry: introducing Geochemical Data Toolkit (GCDkit). *Journal of Petrology* 47(6):1255-1259

Kröner, A., Alexeiev, D. V., Hegner, E., Rojas-Agramonte, Y., Corsini, M., Chao, Y., ... & Tretyakov, A. A. (2012). Zircon and muscovite ages, geochemistry, and Nd–Hf isotopes for the Aktyuz metamorphic terrane: evidence for an Early Ordovician collisional belt in the northern Tianshan of Kyrgyzstan. *Gondwana Research*, 21(4), 901-927.

Kröner, A., Kovach, V., Alexeiev, D., Wang, K. L., Wong, J., Degtyarev, K., & Kozakov, I. (2017). No excessive crustal growth in the Central Asian Orogenic Belt: Further evidence from field relationships and isotopic data. *Gondwana Research*, 50, 135-166.

Kröner, A., Kovach, V., Belousova, E., Hegner, E., Armstrong, R., Dolgopolova, A., ... & Sun, M. (2014). Reassessment of continental growth during the accretionary history of the Central Asian Orogenic Belt. *Gondwana Research*, 25(1), 103-125.

Kovalenko, V. I., Yarmolyuk, V. V., Kovach, V. P., Kotov, A. B., Kozakov, I. K., Salnikova, E. B., & Larin, A. M. (2004). Isotope provinces, mechanisms of generation and sources of the continental crust in the Central Asian mobile belt: geological and isotopic evidence. *Journal of Asian Earth Sciences*, 23(5), 605-627.

Kurz, W., & Froitzheim, N. (2002). The exhumation of eclogite-facies metamorphic rocks—a review of models confronted with examples from the Alps. *International Geology Review*, 44(8), 702-743.

Lamont, T. N., Searle, M. P., Gopon, P., Roberts, N. M., Wade, J., Palin, R. M., & Waters, D. J. (2020). The Cycladic Blueschist Unit on Tinos, Greece: Cold NE subduction and SW directed extrusion of the Cycladic continental margin under the Tsiknias Ophiolite. *Tectonics*, 39(9), e2019TC005890.

Li, J. (2019). *A structural and stratigraphic study in Liuyuan area, Southern Beishan orogenic collage, Northwest China* [Master's thesis, University of Waterloo]. UWSpace.

Li, Z. X., Bogdanova, S. V., Collins, A. S., Davidson, A., De Waele, B., Ernst, R. E., ... & Karlstrom, K. E. (2008). Assembly, configuration, and break-up history of Rodinia: a synthesis. *Precambrian research*, 160(1-2), 179-210

Li, S., Wang, T., Wilde, S. A., Tong, Y., Hong, D., & Guo, Q. (2012). Geochronology, petrogenesis and tectonic implications of Triassic granitoids from Beishan, NW China. *Lithos*, 134, 123-145.

Li, S., Wilde, S. A., He, Z., Jiang, X., Liu, R., & Zhao, L. (2014). Triassic sedimentation and postaccretionary crustal evolution along the Solonker suture zone in Inner Mongolia, China. *Tectonics*, 33(6), 960-981.

Little, T. A., Hacker, B. R., Gordon, S. M., Baldwin, S. L., Fitzgerald, P. G., Ellis, S., & Korchinski, M. (2011). Diapiric exhumation of Earth's youngest (UHP) eclogites in the gneiss domes of the D'Entrecasteaux Islands, Papua New Guinea. *Tectonophysics*, 510(1-2), 39-68.

Liu, X., Chen, B., Jahn, B. M., Wu, G., & Liu, Y. (2011). Early Paleozoic (ca. 465 Ma) eclogites from Beishan (NW China) and their bearing on the tectonic evolution of the southern Central Asian Orogenic Belt. *Journal of Asian Earth Sciences*, 42(4), 715-731.

Ludwig, K. R. (2012*). Isoplot 3.75: A geochronological toolkit for Microsoft Excel.* Berkeley Geochronology Center Special Publication, 5.

Mao, Q. (2008) *Paleozoic to Early Mesozoic Accretionary and Collisional Tectonics of the Beishan and Adjacent Area, Northwest China* [Unpublished PhD thesis]. Institute of Geology and Geophysics, Chinese Academy of Sciences, Beijing.

Mao, Q., Xiao, W., Fang, T., Wang, J., Han, C., Sun, M., & Yuan, C. (2012). Late Ordovician to early Devonian adakites and Nb-enriched basalts in the Liuyuan area, Beishan, NW China: implications for early Paleozoic slab-melting and crustal growth in the southern Altaids. *Gondwana Research*, 22(2), 534-553.

Mao, Q., Xiao, W., Windley, B. F., Han, C., Qu, J., Ao, S., ... & Guo, Q. (2012). The Liuyuan complex in the Beishan, NW China: a Carboniferous–Permian ophiolitic fore-arc sliver in the southern Altaids. *Geological Magazine*, 149(3), 483-506.

Martin, C., & Duchêne, S. (2015). Residual water in hydrous minerals as a kinetic factor for omphacite destabilization into symplectite in the eclogites of Vårdalsneset (WGR, Norway). *Lithos*, 232, 162-173.

Masago, H., Omori, S., & Maruyama, S. (2010). Significance of retrograde hydration in collisional metamorphism: a case study of water infiltration in the Kokchetav ultrahigh-pressure metamorphic rocks, northern Kazakhstan. *Gondwana Research*, 18(1), 205-212.

Mei, H., Yu, H., Li, Q., Lu, S., Li, H., Zuo, Y., D., Ye & Liu, J. (1999). The first discovery of eclogite and Palaeoproterozoic granitoids in the Beishan area, northwestern Gansu Province, China. *Chinese Science Bulletin*, 44(4), 356-361.

Middlemost, E. A. (1994). Naming materials in the magma/igneous rock system. *Earth-Science Reviews*, 37(3-4), 215-224.

Miyashiro, A. (1974). Volcanic rock series in island arcs and active continental margins. *American journal of science*, 274(4), 321-355.

Möller, C., Andersson, J., Dyck, B., & Lundin, I. A. (2015). Exhumation of an eclogite terrane as a hot migmatitic nappe, Sveconorwegian orogen. *Lithos*, 226, 147-168.

Natural Resources Canada. (1995). *Certificate of Analysis, SY-4 Diorite Gneiss.* https://www.nrcan.gc.ca/sites/www.nrcan.gc.ca/files/mineralsmetals/pdf/mms-smm/tect-tech/ccrmp/cer-cer/sy-4-eng.pdf

Niu, Y., Zhao, Z., Zhu, D. C., & Mo, X. (2013). Continental collision zones are primary sites for net continental crust growth—a testable hypothesis. *Earth-Science Reviews*, 127, 96-110.

Pearce, J. A. (1996). A user's guide to basalt discrimination diagrams. Trace element geochemistry of volcanic rocks: applications for massive sulphide exploration. *Geological Association of Canada, Short Course Notes*, 12(79), 113.

Pearce, J. A., Harris, N. B., & Tindle, A. G. (1984). Trace element discrimination diagrams for the tectonic interpretation of granitic rocks. *Journal of petrology*, 25(4), 956-983.

Peterman, E. M., Hacker, B. R., & Baxter, E. F. (2009). Phase transformations of continental crust during subduction and exhumation: Western Gneiss Region, Norway. *European Journal of Mineralogy*, 21(6), 1097-1118.

Qu, J. F., Xiao, W. J., Windley, B. F., Han, C. M., Mao, Q. G., Ao, S. J., & Zhang, J. E. (2011). Ordovician eclogites from the Chinese Beishan: implications for the tectonic evolution of the southern Altaids. *Journal of Metamorphic Geology*, 29(8), 803-820.

Ramsay, J. G. (1967). *Folding and Fracturing of Rocks*. McGraw-Hill, New York.

Ross, P. S., & Bédard, J. H. (2009). Magmatic affinity of modern and ancient subalkaline volcanic rocks determined from trace-element discriminant diagrams. *Canadian Journal of Earth Sciences*, 46(11), 823-839.

Rubatto, D. (2017). Zircon: the metamorphic mineral. *Reviews in mineralogy and geochemistry*, 83(1), 261-295.

Rumble D, Liou JG, and Jahn BM (2003) Continental crust subduction and ultrahigh pressure metamorphism. In: Rudnick RL (ed.) *Treatise on Geochemistry, Vol. 3: The Crust* (pp. 293–319). Oxford: Elsevier.

Searle, M. P., Warren, C. J., Waters, D. J., & Parrish, R. R. (2004). Structural evolution, metamorphism and restoration of the Arabian continental margin, Saih Hatat region, Oman Mountains. *Journal of Structural Geology*, 26(3), 451-473.

Saktura, W. M., Buckman, S., Nutman, A. P., Belousova, E. A., Yan, Z., & Aitchison, J. C. (2017). Continental origin of the Gubaoquan eclogite and implications for evolution of the Beishan Orogen, Central Asian Orogenic Belt, NW China. *Lithos*, 294, 20-38.

Şengör, A. M. C., Natal'In, B. A., & Burtman, V. S. (1993). Evolution of the Altaid tectonic collage and Palaeozoic crustal growth in Eurasia. *Nature*, 364(6435), 299.

Skrzypek, E., Schulmann, K., Štípská, P., Chopin, F., Lehmann, J., Lexa, O., & Haloda, J. (2011). Tectono-metamorphic history recorded in garnet porphyroblasts: insights from thermodynamic modelling and electron backscatter diffraction analysis of inclusion trails. *Journal of Metamorphic Geology*, 29(4), 473-496.

Skrzypek, E., Štípská, P., Schulmann, K., Lexa, O., & Lexova, M. (2011). Prograde and retrograde metamorphic fabrics–a key for understanding burial and exhumation in orogens (Bohemian Massif). *Journal of Metamorphic Geology*, 29(4), 451-472.

Smye, A. J., Greenwood, L. V., & Holland, T. J. B. (2010). Garnet–chloritoid–kyanite assemblages: eclogite facies indicators of subduction constraints in orogenic belts. *Journal of Metamorphic Geology*, 28(7), 753-768.

Soldner, J., Štípská, P., Schulmann, K., Yuan, C., Anczkiewicz, R., Sala, D., ... & Wang, X. (2020). Coupling of P–T–t–D histories of eclogite and metagreywacke—Insights to late Ordovician–Silurian crustal folding events recorded in the Beishan Orogen (NW China). *Journal of Metamorphic Geology*, 38(6), 555-591.

Soldner, J., Yuan, C., Schulmann, K., Štípská, P., Jiang, Y., Zhang, Y., & Wang, X. (2020). Grenvillean evolution of the Beishan Orogen, NW China: Implications for development of an active Rodinian margin. *GSA Bulletin*, 132(7-8), 1657-1680.

Song, D., Xiao, W., Han, C., Li, J., Qu, J., Guo, Q., ... & Wang, Z. (2013). Progressive accretionary tectonics of the Beishan orogenic collage, southern Altaids: insights from zircon U–Pb and Hf isotopic data of high-grade complexes. *Precambrian Research*, 227, 368-388.

Štípská, P., Pitra, P., & Powell, R. (2006). Separate or shared metamorphic histories of eclogites and surrounding rocks? An example from the Bohemian Massif. *Journal of Metamorphic Geology*, 24(3), 219-240.

Štípská, P., Schulmann, K., & Kröner, A. (2004). Vertical extrusion and middle crustal spreading of omphacite granulite: a model of syn-convergent exhumation (Bohemian Massif, Czech Republic). *Journal of Metamorphic Geology*, 22(3), 179-198.

Sun, S. S., & McDonough, W. F. (1989). Chemical and isotopic systematics of oceanic basalts: implications for mantle composition and processes. *Geological Society, London, Special Publications*, 42(1), 313-345.

Tian, Z., Xiao, W., Sun, J., Windley, B. F., Glen, R., Han, C., ... & Song, D. (2015). Triassic deformation of Permian Early Triassic arc-related sediments in the Beishan (NW China): last pulse of the accretionary orogenesis in the southernmost Altaids. *Tectonophysics*, 662, 363-384.

Wang, Y. U., Luo, Z., Santosh, M., Wang, S., & Wang, N. A. (2017). The Liuyuan Volcanic Belt in NW China revisited: evidence for Permian rifting associated with the assembly of continental blocks in the Central Asian Orogenic Belt. *Geological Magazine*, 154(2), 265-285.

Wang, X., Yuan, C., Zhang, Y., Long, X., Sun, M., Wang, L., ... & Lin, Z. (2018). S-type granite from the Gongpoquan arc in the Beishan Orogenic Collage, southern Altaids: implications for the tectonic transition. *Journal of Asian Earth Sciences*, 153, 206-222.

Wang, Y., Zhang, A., Cawood, P. A., Fan, W., Xu, J., Zhang, G., & Zhang, Y. (2013). Geochronological, geochemical and Nd–Hf–Os isotopic fingerprinting of an early Neoproterozoic arc–back-arc system in South China and its accretionary assembly along the margin of Rodinia. *Precambrian Research*, 231, 343-371.

Whalen, J. B., McNicoll, V. J., van Staal, C. R., Lissenberg, C. J., Longstaffe, F. J., Jenner, G. A., & van Breeman, O. (2006). Spatial, temporal and geochemical characteristics of Silurian collision-zone magmatism, Newfoundland Appalachians: an example of a rapidly evolving magmatic system related to slab break-off. *Lithos*, 89(3-4), 377-404.

Whitney, D. L. (2002). Coexisting andalusite, kyanite, and sillimanite: Sequential formation of three Al2SiO5 polymorphs during progressive metamorphism near the triple point, Sivrihisar, Turkey. *American Mineralogist*, 87(4), 405-416.

Willner, A. P., Krohe, A., & Maresch, W. V. (2000). Interrelated PTtd paths in the Variscan Erzgebirge dome (Saxony, Germany): Constraints on the rapid exhumation of high-pressure rocks from the root zone of a collisional orogen. *International Geology Review*, 42(1), 64-85.

Wilson, S. (2010) *Certificate of analysis, Syenite, Table Mountain, STM-2*. Denver, Colorado: USGS

Windley, B. F., Alexeiev, D., Xiao, W., Kröner, A., & Badarch, G. (2007). Tectonic models for accretion of the Central Asian Orogenic Belt. *Journal of the Geological Society*, 164(1), 31-47.

Xiao, W., Han, C., Liu, W., Wan, B., Zhang, J. E., Ao, S., ... & Luo, J. (2014). How many sutures in the southern central Asian orogenic belt: insights from east Xinjiang–west Gansu (NW China)?. *Geoscience Frontiers*, 5(4), 525-536.

Xiao, W. J., Mao, Q. G., Windley, B. F., Han, C. M., Qu, J. F., Zhang, J. E., ... & Shan, Y. H. (2010). Paleozoic multiple accretionary and collisional processes of the Beishan orogenic collage. *American Journal of Science*, 310(10), 1553-1594.

Xiao, W., Windley, B. F., Han, C., Liu, W., Wan, B., Zhang, J. E., ... & Song, D. (2018). Late Paleozoic to early Triassic multiple roll-back and oroclinal bending of the Mongolia collage in Central Asia. *Earth-Science Reviews*, 186, 94-128.

Xiao, W., Windley, B. F., Sun, S., Li, J., Huang, B., Han, C., ... & Chen, H. (2015). A tale of amalgamation of three Permo-Triassic collage systems in Central Asia: oroclines, sutures, and terminal accretion. *Annual review of earth and planetary sciences*, 43, 477-507.

Xiao, W., Windley, B. F., Hao, J., & Zhai, M. (2003). Accretion leading to collision and the Permian Solonker suture, Inner Mongolia, China: Termination of the central Asian orogenic belt. *Tectonics*, 22(6).

Yakubchuk, A. (2004). Architecture and mineral deposit settings of the Altaid orogenic collage: a revised model. *Journal of Asian Earth Sciences*, 23(5), 761-779.

Yakymchuk, C., Clark, C., & White, R. W. (2017). Phase relations, reaction sequences and petrochronology. *Reviews in Mineralogy and Geochemistry*, 83(1), 13-53.

Young, D. J., & Kylander-Clark, A. R. C. (2015). Does continental crust transform during eclogite facies metamorphism?. *Journal of Metamorphic Geology*, 33(4), 331-357.

Zachariah, J. K., Hanson, G. N., & Rajamani, V. (1995). Postcrystallization disturbance in the neodymium and lead isotope systems of metabasalts from the Ramagiri schist belt, southern India. *Geochimica et Cosmochimica Acta*, 59(15), 3189-3203.

Zhang, Y., Yuan, C., Sun, M., Long, X., Xia, X., Wang, X., & Huang, Z. (2015). Permian doleritic dikes in the Beishan Orogenic Belt, NW China: asthenosphere–lithosphere interaction in response to slab break-off. *Lithos*, 233, 174-192.

Zhao, G., Wang, Y., Huang, B., Dong, Y., Li, S., Zhang, G., & Yu, S. (2018). Geological reconstructions of the East Asian blocks: From the breakup of Rodinia to the assembly of Pangea. *Earth-Science Reviews*, 186, 262-286.

Zhu, J., Lv, X., & Peng, S. (2016). U-Pb zircon geochronology, geochemistry and tectonic implications of the early Devonian granitoids in the Liuyuan area, Beishan, NW China. *Geosciences Journal*, 20(5), 609-625.

Zong, K., Klemd, R., Yuan, Y., He, Z., Guo, J., Shi, X., ... & Zhang, Z. (2017). The assembly of Rodinia: the correlation of early Neoproterozoic (ca. 900 Ma) high-grade metamorphism and continental arc formation in the southern Beishan Orogen, southern Central Asian Orogenic Belt (CAOB). *Precambrian Research*, 290, 32-48.

Appendix A

Coordinate list of samples discussed in thesis

Figure		Locality	Latitude	Longitude
3		60414	40.9874397	95.0387132
9	A	64901	41.0709777	95.1593926
9	B	62603	41.0272981	95.089617
9	C	61005	41.0002798	95.0845973
9	D	65497	41.0085489	95.1739129
9	E	65177	41.0118909	95.2139424
10	A	65600	40.9889681	95.0424052
10	B	65356	41.0115	95.1963303
10	C	65609	40.9864184	95.0472687
11	A	65398	41.005045	95.1596369
11	B	65206	41.0229157	95.2048884
12	A	60414	40.9874397	95.0387132
12	B	65638	40.9822906	95.0647705
12	C	65662	40.9864872	95.0436299
13	A	64866	41.067327	95.0299705
13	B	65025	41.1047332	95.0344964
13	C	62803	41.0091779	95.1131832
13	D	62803	41.0091779	95.1131832
14	A	65600	40.9889681	95.0424052
14	B	64004	41.0253904	95.0655918
14	C	65404	40.9800929	95.0593205
14	D	64834	40.9958114	95.0766683
14	E	60817	41.0252738	95.0743056
14	F	65616	40.9845338	95.0491111
14	G	65628	40.9843485	95.0323335
14	H	65401	40.9854708	95.0736283
14	I	65469	41.0188882	95.2263457
14	J	65209	41.0205909	95.206064
14	K	64885	41.0703432	95.0580407
14	L	60604	41.0060822	95.0301021
14	M	62114	40.9908978	95.1053411
14	N	65239	41.024179	95.2250242
14	O	60817	41.0252738	95.0743056
14	P	62607	41.0287936	95.0878252
14	Q	62607	41.0287936	95.0878252
15	A-B	60817	41.0252738	95.0743056
15	C-D	64001	41.0257834	95.0659825
15	E-F	65149	41.0696046	95.128125
16	A	64519	41.0227142	95.0762848
16	B	64314	41.0062895	95.0932703
16	C	61731	41.0020388	95.0427423
16	D	65675	40.9866754	95.0486269
16	E-F	64853	41.1126062	95.0105769
16	G-H	64002	41.0256138	95.0658815
16	I	64002	41.0256138	95.0658815
16	J	65209	41.0205909	95.206064
17	A	64705	40.9882988	95.0401975
17	B	65492	40.9860136	95.0432946
17	C	65601	40.9884598	95.0422386
17	D-E	65659	40.9862599	95.0433386
17	F	60414	40.9874397	95.0387132
18	A	62610	41.0295927	95.0883326
18	B	65239	41.024179	95.2250242
19	A-B	60414	40.9874397	95.0387132
19	C	63905B	40.9895107	95.0673962
19	D	64877	41.0213538	95.076687
19	D	64501	41.0213115	95.0765836

Appendix B

Cross-sections of study area

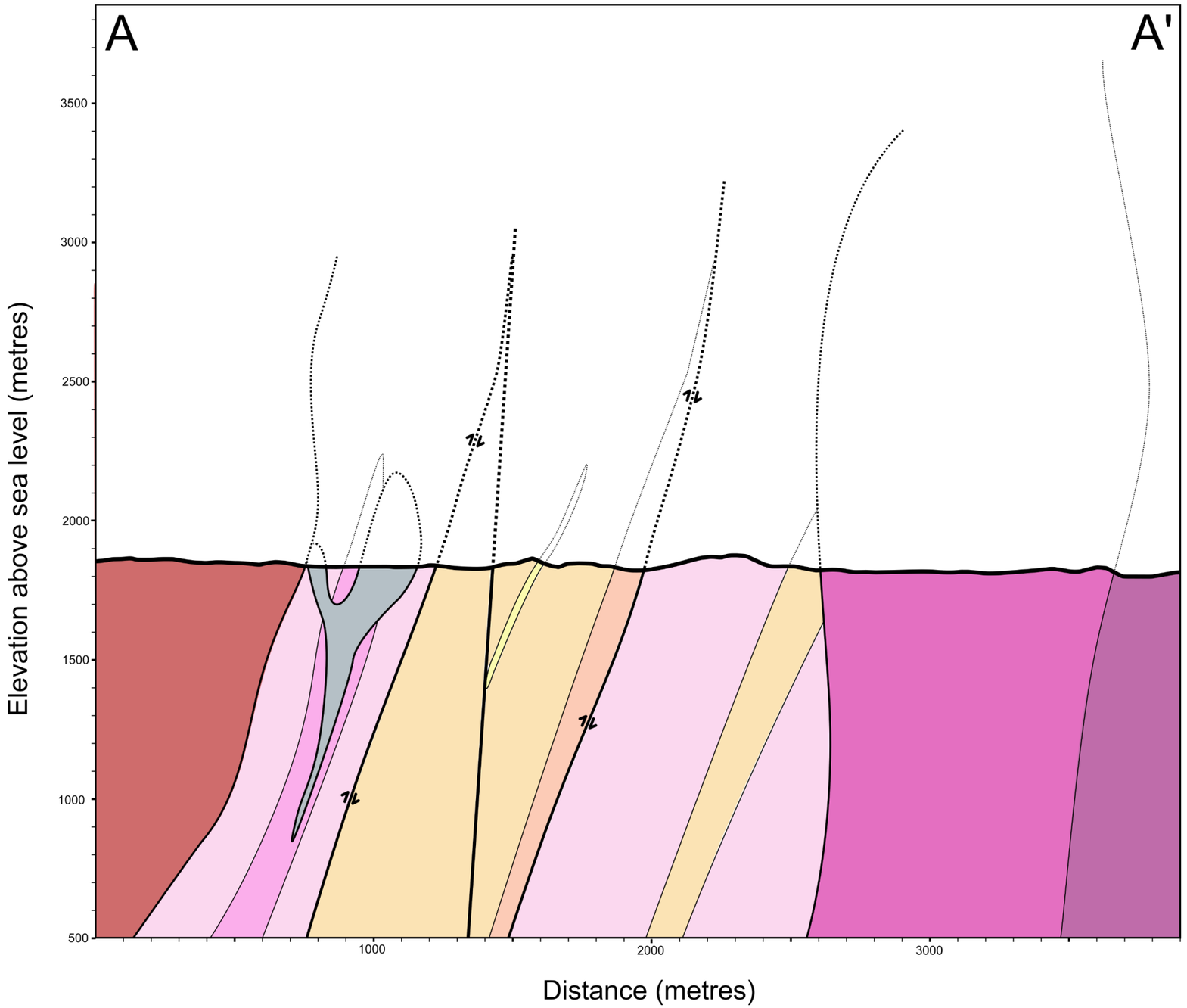

Figure 27. Cross-section along transect A-A'-A'', as marked on map. Colours correspond to those used in map.

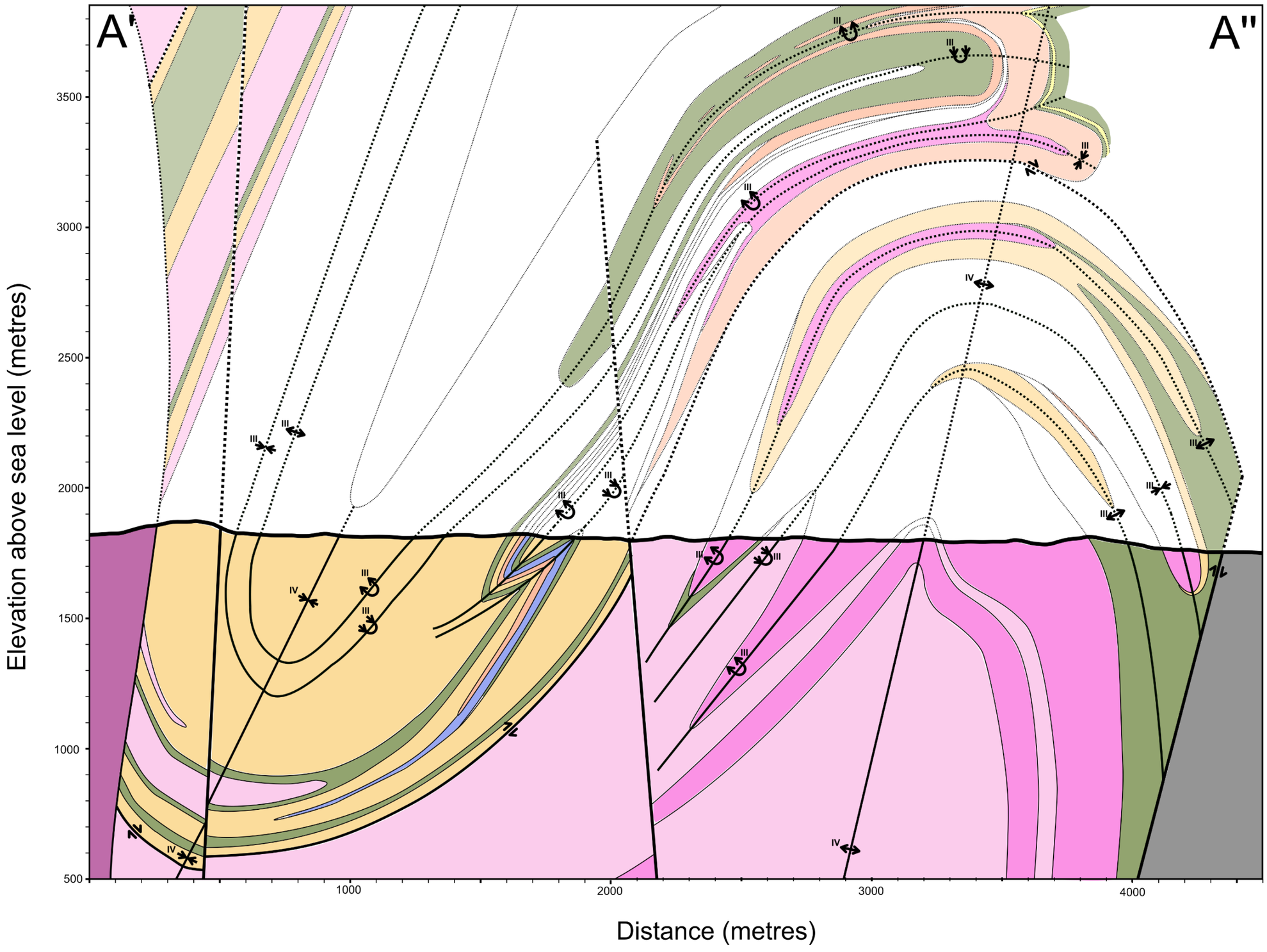

Figure 27, continued.

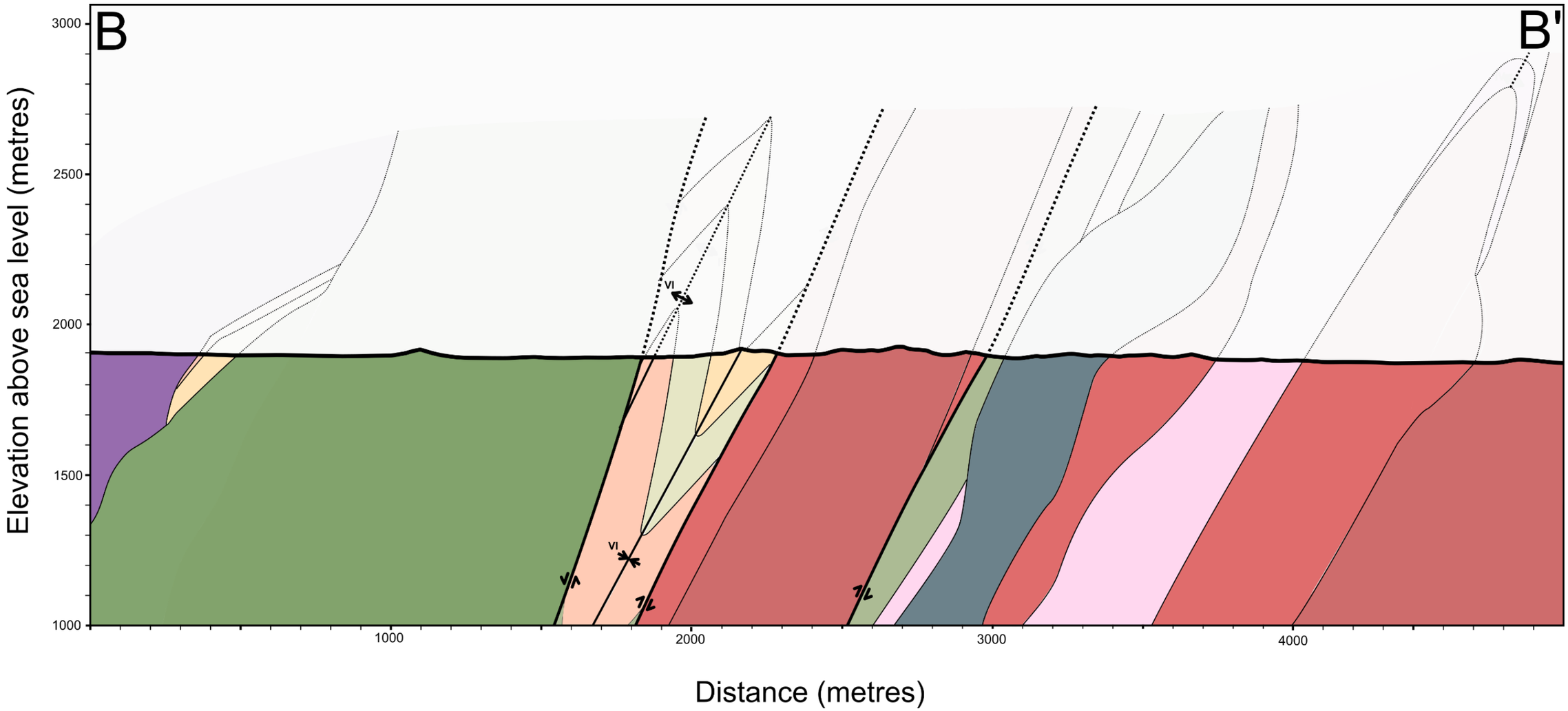

Figure 28. Cross-section along transect B-B', as marked on map. Colours correspond to those used in map.

Appendix C

Geochronological standard data

Spot	U	Th	Th/U	$\%^{206}Pb_c$	^{238}U / ^{206}Pb*		$^{207}Pb^*$ / $^{206}Pb^*$		^{206}Pb / ^{238}U age	
1	340	151	0.45	0.32	0.145	2.92	0.057	2.89	418.0	4.3
2	343	173	0.51	0.00	0.163	2.34	0.055	2.79	417.5	5.9
3	219	118	0.54	0.24	0.177	2.91	0.056	3.57	414.8	5.2
4	291	143	0.49	0.41	0.166	2.52	0.056	3.02	418.0	4.5
5	291	128	0.44	-0.54	0.141	2.75	0.054	3.11	426.9	4.6
6	2652	1643	0.62	0.04	0.202	0.93	0.055	1.00	426.1	2.4
7	105	33	0.31	1.35	0.100	5.35	0.063	4.78	421.2	7.1
8	135	57	0.42	0.00	0.141	4.06	0.054	4.59	409.4	6.8
9	304	152	0.50	0.00	0.161	2.66	0.055	3.69	409.6	7.9
10	158	87	0.55	0.00	0.188	3.54	0.060	4.24	403.3	10.4
11	1367	904	0.66	0.00	0.211	1.06	0.056	1.42	419.1	2.7
12	211	97	0.46	0.00	0.157	3.00	0.058	2.86	409.6	4.7
~~13~~	~~120~~	~~54~~	0.45	~~0.00~~	~~0.165~~	~~4.75~~	~~0.056~~	~~3.77~~	~~397.7~~	~~6.4~~
14	235	50	0.22	0.00	0.075	3.97	0.055	2.72	411.5	4.4
15	290	151	0.52	0.00	0.178	2.38	0.056	2.44	412.2	4.0
16	423	218	0.52	0.00	0.169	2.03	0.056	2.03	417.5	3.6
17	444	126	0.28	0.00	0.092	2.71	0.057	2.00	412.4	3.5

Table 5. Geochronological measurements on Temora zircons (416.8±1.1 Ma; Black et al., 2003), for samples measured with 13 μm spot size (60414.101, 60414.102, 64501). Rejected spots are struck through.

Spot	U	Th	Th/U	$\%^{206}Pb_c$	^{238}U / ^{206}Pb*	$^{207}Pb^*$ / $^{206}Pb^*$	^{206}Pb / ^{238}U age
1	140	63	0.45	0.50	0.152 ± 2.28	0.058 ± 2.59	423.1 ± 3.8
2	247	112	0.45	-0.13	0.144 ± 1.78	0.057 ± 2.00	422.3 ± 2.9
3	459	162	0.35	0.20	0.113 ± 1.48	0.056 ± 1.49	416.0 ± 2.2
4	142	37	0.26	0.31	0.082 ± 3.16	0.053 ± 2.78	418.8 ± 3.8
5	412	171	0.42	0.08	0.132 ± 3.19	0.056 ± 1.58	421.2 ± 3.6
6	256	61	0.24	-0.25	0.081 ± 2.38	0.055 ± 2.05	425.7 ± 3.0
7	357	148	0.41	0.08	0.137 ± 1.61	0.055 ± 1.78	411.8 ± 2.5
8	202	61	0.30	0.36	0.097 ± 2.54	0.056 ± 2.37	406.2 ± 5.7
9	255	62	0.24	-0.17	0.078 ± 2.51	0.054 ± 2.15	419.3 ± 3.0
10	102	31	0.31	0.21	0.101 ± 3.46	0.057 ± 3.28	402.8 ± 4.6
11	271	79	0.29	-0.05	0.096 ± 2.20	0.055 ± 2.08	415.3 ± 2.8
12	405	209	0.52	0.15	0.168 ± 1.38	0.055 ± 1.68	413.3 ± 2.4
13	306	186	0.61	-0.16	0.201 ± 1.47	0.055 ± 1.95	411.6 ± 2.7
~~14~~	~~209~~	~~106~~	~~0.51~~	~~-0.10~~	~~0.164 ± 1.95~~	~~0.056 ± 2.37~~	~~397.9 ± 3.2~~
15	134	65	0.49	0.10	0.158 ± 2.44	0.056 ± 2.87	415.9 ± 4.0
16	58	18	0.32	-0.69	0.099 ± 4.51	0.055 ± 4.30	427.5 ± 5.9
17	150	50	0.33	-0.47	0.117 ± 2.60	0.055 ± 2.70	410.9 ± 3.7
19	274	135	0.49	0.07	0.159 ± 1.63	0.057 ± 1.91	419.4 ± 3.1
20	235	108	0.46	0.32	0.151 ± 1.86	0.054 ± 2.19	413.2 ± 3.0
~~21~~	~~408~~	~~99~~	~~0.24~~	~~-0.02~~	~~0.076 ± 2.06~~	~~0.056 ± 1.71~~	~~390.0 ± 2.3~~
22	183	51	0.28	1.43	0.109 ± 2.49	0.061 ± 2.37	414.1 ± 3.5
23	192	49	0.26	0.32	0.078 ± 2.80	0.049 ± 2.72	420.4 ± 3.3
24	191	72	0.38	0.44	0.127 ± 2.62	0.051 ± 2.89	409.3 ± 3.8
25	1150	509	0.44	-0.02	0.138 ± 1.35	0.050 ± 2.24	407.9 ± 2.5
26	96	30	0.31	-0.32	0.096 ± 4.53	0.051 ± 6.21	411.3 ± 4.6
27	170	91	0.53	-0.21	0.160 ± 2.31	0.049 ± 2.74	407.3 ± 5.5
28	257	154	0.60	-0.34	0.194 ± 1.63	0.056 ± 2.11	418.7 ± 3.1
31	225	108	0.48	-0.27	0.157 ± 1.98	0.055 ± 2.35	420.8 ± 4.9
32	259	66	0.26	-0.14	0.079 ± 2.48	0.057 ± 2.10	418.4 ± 3.0
33	267	158	0.59	0.05	0.197 ± 1.59	0.055 ± 2.09	429.8 ± 3.1
34	73	22	0.30	-2.63	0.107 ± 5.26	0.058 ± 4.29	427.0 ± 6.6
35	319	144	0.45	0.00	0.144 ± 1.82	0.056 ± 2.06	415.9 ± 3.0
36	2262	1618	0.72	-0.05	0.231 ± 0.53	0.056 ± 0.74	423.7 ± 1.5

Table 6. Geochronological measurements on Temora zircon (416.8±1.1 Ma; Black et al., 2003), for samples measured with 24 μm spot size (63905B). Rejected spots are struck through.

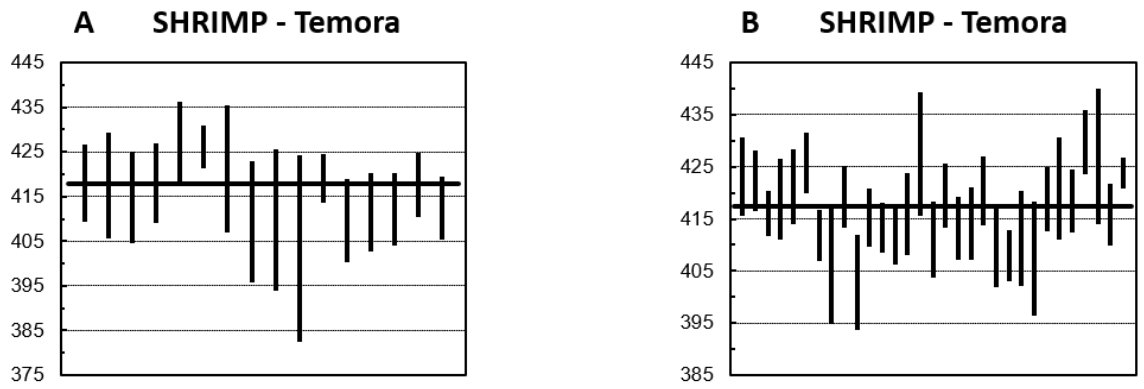

Figure 29. 206Pb/238U ages for the TEMORA (416.8±1.1 Ma; Black et al., 2003) primary standard, used for the calibration of the SHRIMP U-Pb ages. Measurements are ordered by time of collection. Rejected ages are not displayed (spot 13 for A, spots 14 and 21 for B; **Tables 5;6**). Black horizontal line depicts average of measurements, to give an indication of the standard performance relative to the commonly accepted age for TEMORA (Black et al., 2003); (A) standard for samples measured with 13 μm spot size (60414.101, 60414.102, 64501). (B) standard for samples measured with 24 μm spot size (63905)**.**

Appendix D

Geochemistry

Group	Felsic orthogneiss			Eclogite		(garnet) amphibolite		
Sample	61003	63802	63905B	60414.20.1	60414.20.2	62610	64015	63905
Latitude	40.99436	41.00713	40.98951	40.98744	40.98744	41.02959	41.01584	40.98951
Longitude	95.08137	95.05065	95.06740	95.03871	95.03871	95.08833	95.05605	95.06740
major element (wt%):								
SiO2	75.1	73.5	72.6	51	47.7	45.1	51.5	49
Al2O3	13.85	14.8	11.4	11.95	12.8	16.4	12.7	12.15
Fe2O3	0.25	0.25	6.85	14.55	17.1	16.5	16.25	17.05
CaO	0.85	0.96	1.14	7.25	10.5	7.31	8.02	8.79
MgO	0.15	0.09	1.9	6.33	6.98	6.96	5.04	5.93
Na2O	3.36	3.01	3.35	2.13	1.9	0.68	2.42	1.62
K2O	5.65	5.91	0.47	0.68	0.19	2.32	1.17	0.86
Cr2O3	<0.002	<0.002	<0.002	0.014	0.021	0.024	0.006	0.017
TiO2	0.02	0.03	0.49	1.71	1.73	1.66	2.2	2.64
MnO	<0.01	<0.01	0.16	0.23	0.25	0.37	0.23	0.23
P2O5	<0.01	0.02	0.07	0.13	0.14	0.15	0.23	0.4
SrO	0.02	0.02	0.01	0.01	<0.01	0.04	0.01	0.01
BaO	0.09	0.16	0.02	0.01	<0.01	0.06	0.03	0.01
LOI	0.81	1.51	1.45	4.56	1.17	2.4	0.99	1.44
Total	100.15	100.26	99.91	100.55	100.48	99.97	100.8	100.15

Table 7. Major element data for metamorphic samples

Group	Felsic orthogneiss			Eclogite		(garnet) amphibolite		
Sample	61003	63802	63905B	60414.20.1	60414.20.2	62610	64015	63905
Trace element and rare earth element (ppm):								
Ag	<0.5	<0.5	<0.5	<0.5	<0.5	<0.5	<0.5	<0.5
As	<5	<5	<5	5	<5	<5	<5	<5
Cd	<0.5	<0.5	<0.5	<0.5	<0.5	0.6	0.8	0.9
Co	1	<1	7	50	48	44	44	52
Cu	3	3	3	61	67	7	24	196
Li	<10	<10	10	20	10	10	10	10
Mo	<1	<1	<1	1	1	<1	<1	<1
Ni	<1	<1	4	85	60	58	46	79
Pb	44	58	7	3	<2	6	13	4
Sc	1	1	11	35	46	42	36	41
Tl	<10	<10	<10	<10	<10	<10	<10	<10
Zn	7	4	63	121	138	91	130	147
Ba	742	1445	202	47	17.2	527	241	117.5
Ce	1.4	3.7	122	12.7	17.4	36.4	36.5	38.8
Cr	<10	<10	10	100	140	170	40	120
Cs	0.6	1.31	0.33	2.48	0.19	1.81	1.8	0.2
Dy	0.34	0.38	15.85	5.52	5.61	5.9	7.25	7.62
Er	0.25	0.38	9.37	3.14	3.72	3.54	3.84	4.53
Eu	0.09	0.35	3.64	1.66	1.17	1.47	1.73	2.06
Ga	18.1	13.3	20.7	16.9	17.3	17.7	20.1	20.8
Gd	0.23	0.28	15.2	5.17	4.75	5.33	7.35	7.59
Hf	2.1	0.8	19.6	2	2.4	3.6	4.2	5.2
Ho	0.07	0.09	3.12	1.06	1.05	1.18	1.38	1.52
La	0.7	2.2	54.3	4.4	6.2	16.5	14.7	16.5
Lu	0.04	0.09	1.41	0.41	0.43	0.5	0.52	0.6
Nb	3.5	1.8	46.7	6.6	7.9	9.6	12.7	14.3
Nd	0.6	1.5	66	10.5	13.3	18.8	23.1	25.6
Pr	0.15	0.4	15.7	1.99	2.61	4.66	4.98	5.43
Rb	103	146.5	15.8	48.4	5.5	121	45.7	19.4
Sm	0.18	0.28	15.1	3.94	4.16	4.64	5.8	6.74
Sn	<1	1	5	2	4	2	3	2
Sr	161.5	199.5	70	78.6	34.3	325	111.5	74.1
Ta	0.4	0.2	3.3	0.4	0.5	0.7	0.9	1
Tb	0.05	0.05	2.27	0.83	0.82	0.89	1.07	1.18
Th	0.17	0.49	13.55	0.05	0.07	4.02	3.52	2.58
Tm	0.04	0.06	1.32	0.43	0.43	0.45	0.56	0.64
U	0.8	0.49	3.83	0.13	0.37	0.91	0.96	0.67
V	5	<5	19	425	473	383	485	490
W	<1	<1	3	3	2	1	2	3
Y	2.5	2.9	79.8	26.9	27.6	29.1	35.6	38.3
Yb	0.25	0.55	9.14	2.59	3.06	3.49	3.74	4.03
Zr	47	31	851	68	88	129	157	206

Table 8. Minor and trace element data for the metamorphic samples.

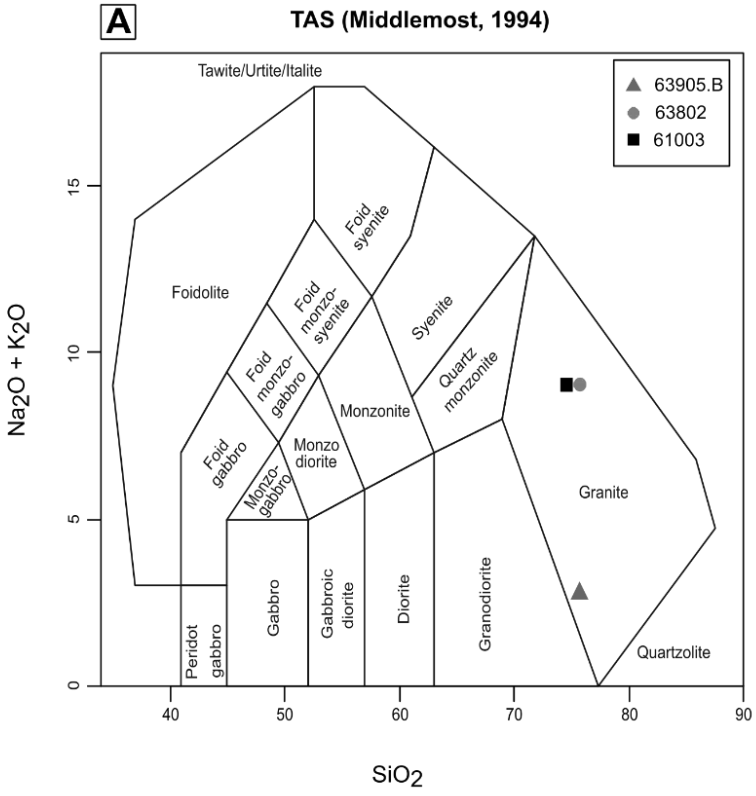
A
TAS (Middlemost, 1994)
Tawite/Urtite/Italite
63905.B
63802
61003
Foidolite
Foid syenite
Foid monzo-syenite
Foid monzo-gabbro
Foid gabbro
Monzo-gabbro
Monzo diorite
Monzonite
Syenite
Quartz monzonite
Granite
Peridot gabbro
Gabbro
Gabbroic diorite
Diorite
Granodiorite
Quartzolite
Na2O + K2O
SiO2

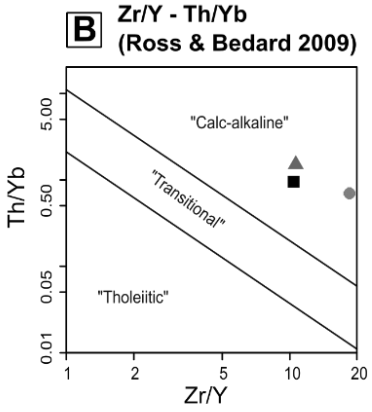
B
Zr/Y - Th/Yb
(Ross & Bedard 2009)
"Calc-alkaline"
"Transitional"
"Tholeiitic"
Th/Yb
Zr/Y

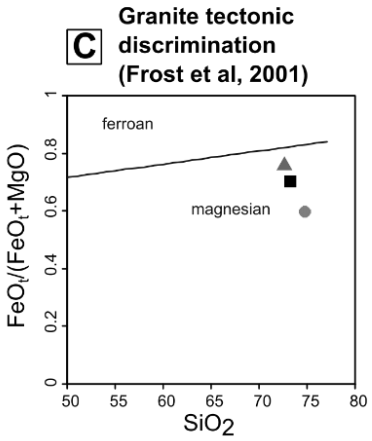
C
Granite tectonic discrimination
(Frost et al, 2001)
ferroan
magnesian
FeOt/(FeOt+MgO)
SiO2

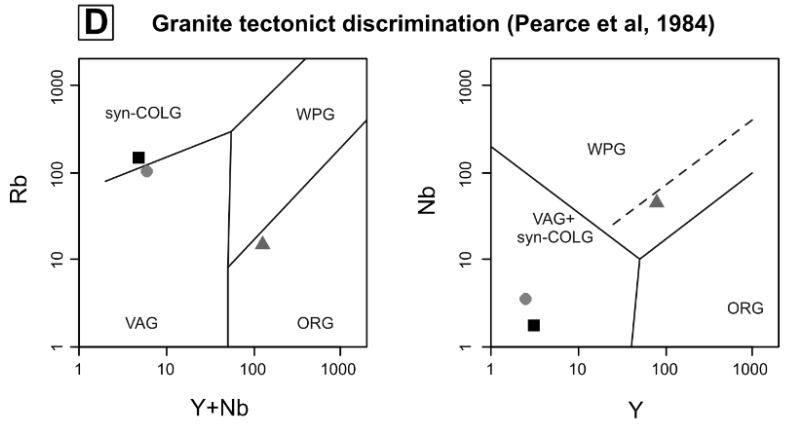
D
Granite tectonict discrimination (Pearce et al, 1984)
syn-COLG
WPG
VAG
ORG
Rb
Y+Nb
WPG
VAG+
syn-COLG
ORG
Nb
Y

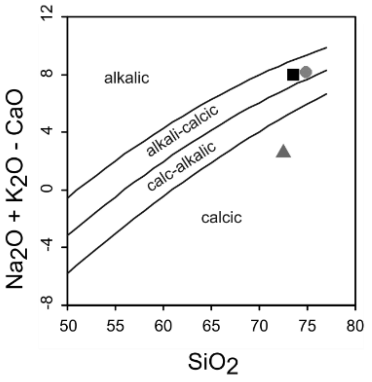
alkalic
alkali-calcic
calc-alkalic
calcic
Na2O + K2O - CaO
SiO2

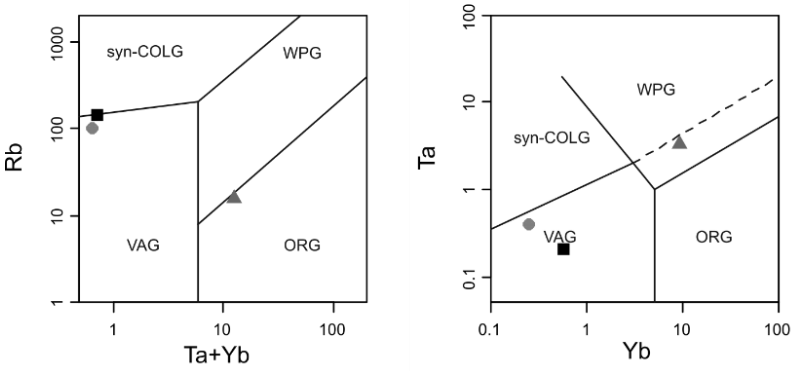
syn-COLG
WPG
VAG
ORG
Rb
Ta+Yb
WPG
syn-COLG
VAG
ORG
Ta
Yb

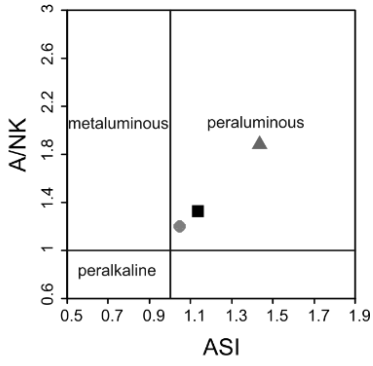
metaluminous
peraluminous
peralkaline
A/NK
ASI

Figure 30, previous page. Geochemistry of felsic metamorphic rocks; A: TAS diagram (Middlemost, 1994); B: calc-alkaline / tholeiitic series determination (Ross & Bedard, 2009); C: granite tectonic discrimination (Frost et al., 2001); D: granite tectonic discrimination (Pearce et al., 1984); abbreviations used: COLG = collisional granite, VAG = volcanic arc granite, WPG = within-plate granite, ORG = orogenic granite.

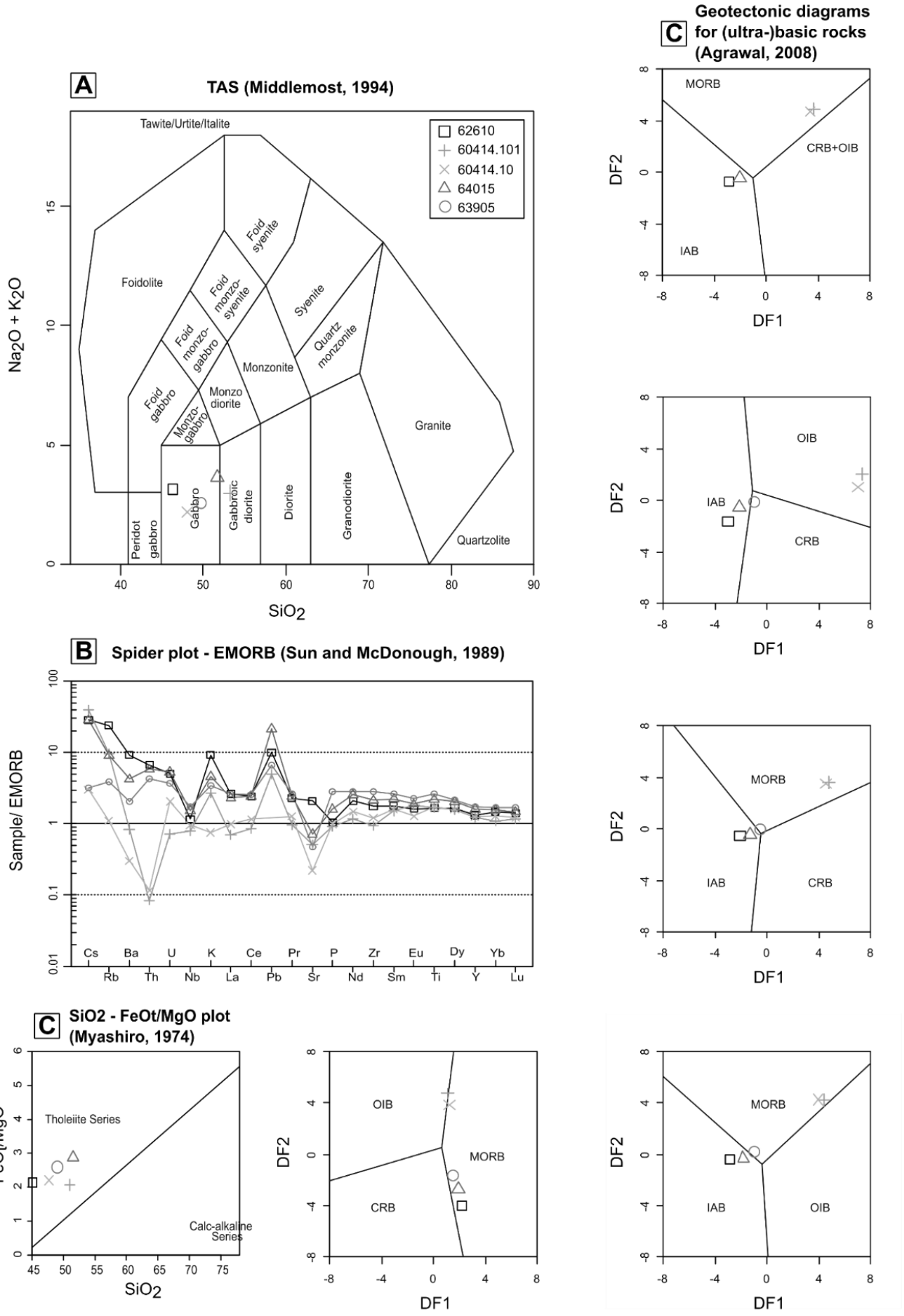
A
TAS (Middlemost, 1994)
Tawite/Urtite/Italite
62610
60414.101
60414.10
64015
63905
Foidolite
Foid syenite
Foid monzo-syenite
Syenite
Quartz monzonite
Foid monzo-gabbro
Monzonite
Foid gabbro
Monzo diorite
Monzo-gabbro
Granite
Gabbro
Gabbroic diorite
Diorite
Granodiorite
Peridot gabbro
Quartzolite
Na2O + K2O
SiO2
B
Spider plot - EMORB (Sun and McDonough, 1989)
Sample/ EMORB
Cs Rb Ba Th U Nb K La Ce Pb Pr Sr P Nd Zr Sm Eu Ti Dy Y Yb Lu
C
SiO2 - FeOt/MgO plot (Myashiro, 1974)
FeOt/MgO
Tholeiite Series
Calc-alkaline Series
SiO2
C
Geotectonic diagrams for (ultra-)basic rocks (Agrawal, 2008)
MORB
CRB+OIB
IAB
DF2
DF1
OIB
CRB
MORB
IAB
CRB
OIB
MORB
CRB
MORB
IAB
OIB

Figure 31, previous page. Geochemistry of mafic metamorphic rocks; A: TAS diagram (Middlemost, 1994); B: spider plot, normalised to E-MORB (Sun and McDonough, 1989); C: calc-alkaline / tholeiitic series determination (Miyashiro, 1974); D: tectonic discrimination of (ultra)mafic rocks (Agrawal, 2008); abbreviations used: (E)MORB = (Enriched) Mid-Oceanic Ridge Basalt, IAB = Island Arc Basalt, OIB = oceanic island basalt, CRB = continental ridge basalt

Description of the geochemistry of the metamorphic samples

The Hebei Geology and Mineral Resources Bureau Langfang Laboratory prepared the crushed powders for geochemical analysis. Geochemical analyses were done by the Vancouver ALS Chemex lab. Major and trace element analysis was performed through acid digestion and ICP-MS on lithium-borate fused beads. For selected samples, base metal concentrations were determined through four-acid digestion and ICP-AES. An STM-2 syenite, an SY-4 diorite gneiss and a BE-N basalt were used as known standards; two out of a total of 34 samples were duplicated. Of these, eight samples were metamorphic rocks, the others igneous.

The duplicates gave nearly identical results to their sibling samples. For standard SY-4, approximately half of the major elements yielded concentrations within the 95% confidence interval specified by the certificate (Natural Resources Canada, 1995). The results for trace elements were less accurate, with more than half lying outside the 95% confidence interval. For BE-N, all major elements fall within two standard deviations (Govindaraju, 1995), whilst only a few trace elements did not . Lastly, for STM-2 all major and trace (except two) elements lied within the certified confidence interval (Wilson, 2010). For some of the base metals in the standards, the certified concentration was unknown. Altogether, the quality of the geochemical data was less than what is expected for a robust interpretation of the data.

A total of eight metamorphic samples were analysed for their geochemistry. Three of the analysed samples were felsic: one metatrondhjemite (18LY61003), one gneissic granite (18LY63905B) and one pegmatitic trondhjemite (18LY63802). The first analysed sample was fresh, whereas the latter two showed slight alteration. The first two samples were garnetiferous. Based on their major element concentrations, all are magnesian and peraluminous granites, whereas 63905B is calcic and the others alkali-calcic (Middlemost, 1994; Frost et al., 2001). All units have a calc-alkaline signature based on the trace elements (Ross & Bedard, 2009). In terms of tectonic setting, 61003 and 63802 have signatures

indicative of volcanic arc and syn-collisional granite, whereas 63905B plots either as a within-plate granite or an oceanic ridge granite (Pearce et al., 1984).

Two eclogites, one fresh sample (60414.20.2) with an assemblage transitional between 2 and 3, and one retrogressed sample (60414.20.1) with assemblage 3, as well as three amphibolites (62610, 64015, 63905) were analysed. All five samples had a gabbroic/basaltic signature except for 60414.20.2, which plots as a gabbroic diorite / basaltic andesite (Middlemost, 1994), based on the major elements. All have tholeiitic compositions (Miyashiro, 1974).

The amphibolites are enriched relative to an average E-MORB (Enriched Mid-Ocean Ridge Basalt) trace element composition (Sun and McDonough, 1989), with broadly sloped profiles characterised by more enrichment in incompatible elements compared to more compatible elements.

They all have negative Nb troughs relative to the overall trend. The eclogites, in contrast, are barely enriched, have a broadly linear profile relative to E-MORB and show a deep trough for Th. Except for the fresh eclogite, all samples show peaks for Pb and K. None of the samples show a significant Eu anomaly. All samples show a trough for Sr except 62610.

On Agrawal's (2008) tectonic discrimination diagrams, the eclogites plot as MORBs or OIBs (Ocean Island Basalt), whereas the amphibolites cluster together but often lie at or near discrimination boundaries. Therefore, 63905 and 64015 plot as island arc basalts or MORB, whilst 62610 plots as MORB or CRB (Continental Rift Basalt).

In addition, numerous igneous samples from this area were also analysed, but these are not directly relevant to this thesis. Their data is included as an appendix.

Discussion of the geochemistry of the metamorphic samples

The observed differences in geochemical composition between the eclogitic mafic rocks could imply open-system behaviour during eclogite-facies metamorphism and subsequent retrogression, or more probable that there are at least two different protoliths. The two identified mafic rocks differ both in incompatible and compatible element concentrations. As large age differences were determined between felsic meta-igneous units, similar age gaps may exist between the metabasites.

There is no clear difference in normalised Eu concentrations – usually a marker of plagioclase-free, eclogite-facies conditions - between the amphibolites and eclogites: neither show a significant anomaly. All eclogitic samples do show a clear Th trough, which may be due to eclogite-facies metamorphism (Saktura et al., 2017 and references therein). However, this alone is not sufficient to argue for a difference in metamorphic history between the amphibolites and eclogites.

The geochemistry of the felsic metamorphic rocks is compatible with Soldner, Yuan et al.'s (2020) suggestion that the metamorphic tectonite belt has various protoliths emplaced or deposited in various tectonic environments. 63905B's composition, in combination with its Mesoproterozoic upper zircon U-Pb intercept, agrees with Soldner, Yuan et al.'s (2020) idea that the area was relatively tectonically quiescent at this time. Sample 61003 and 63802 could represent more active tectonic phases, potentially of arc magmatism, such as the Neoproterozoic (Soldner, Yuan et al., 2020).

Lithology	Basalt	Trondhjemite	Lamprophyre	Granodiorite	Basalt	Gabbro	Tonalite	Leucotonalite	Tonalite	Basalt	Basalt	Tonalite	Felsic dyke
Locality	60414	60414.9	60522	60809	60814	60819	60820	61301	61301.2	61416	61501	61705	62307
	40.98744	40.98744	40.97962	41.00470	41.01187	41.03064	41.03262	41.01785	41.01785	41.00692	40.99853	41.01501	40.96855
Location	95.03871	95.03871	95.04245	95.07641	95.07644	95.07223	95.07363	95.07406	95.07406	95.06377	95.05314	95.04296	95.02346
Major elements (wt-%):													
SiO2	48.7	77.1	51.8	66.5	49.9	51	60.4	67.7	57.9	58	58	62.1	75.8
Al2O3	14.15	13.1	13.6	14.85	12.05	16.05	16.2	14.95	16.8	16.6	16.55	15.75	13.45
Fe2O3	13.05	0.39	13.55	4.4	16.95	11.2	5.77	2.81	7.24	6.39	6.64	5.73	0.98
CaO	11.05	1.47	8.17	3.38	8.92	7.85	5.17	3.23	6.26	6.04	6.14	4.86	1.3
MgO	6.45	0.15	5.24	1.57	4.41	6.22	2.79	1.17	3.21	4.58	4.1	2.67	0.24
Na2O	2.41	6.13	3.57	3.71	2.85	2.6	3.84	4.7	4.19	4.07	3.85	3.25	3.12
K2O	0.65	0.76	0.8	2.43	0.28	1.47	1.88	1.29	1.16	1.82	1.38	2.06	5.2
Cr2O3	0.027	<0.002	0.017	0.002	0.003	0.006	0.003	<0.002	<0.002	0.014	0.007	0.005	<0.002
TiO2	1.99	0.05	2.19	0.78	3.17	1.36	0.75	0.37	1.23	0.89	0.99	0.78	0.12
MnO	0.18	<0.01	0.23	0.07	0.26	0.12	0.08	0.04	0.11	0.1	0.1	0.09	0.01
P2O5	0.2	0.02	0.4	0.13	0.37	0.32	0.2	0.1	0.2	0.11	0.15	0.17	0.02
SrO	0.01	0.01	0.02	0.02	0.01	0.07	0.06	0.02	0.04	0.02	0.04	0.03	0.02
BaO	0.01	0.01	0.01	0.04	0.01	0.03	0.06	0.02	0.03	0.02	0.02	0.03	0.07
LOI	2.03	1.39	1.93	1.59	1.56	2.15	0.91	3.94	1.64	2.22	3.17	1.89	0.53
Total	100.91	100.58	101.53	99.47	100.74	100.45	98.11	100.34	100.01	100.87	101.14	99.42	100.86
Trace and rare earth elements (ppm):													
Ag	<0.5	<0.5	<0.5	<0.5	<0.5	<0.5	<0.5	<0.5	<0.5	<0.5	<0.5	<0.5	<0.5
As	<5	<5	6	5	6	<5	<5	6	<5	<5	<5	<5	<5
Cd	1	<0.5	0.7	<0.5	1.1	<0.5	<0.5	<0.5	0.5	<0.5	<0.5	<0.5	<0.5
Co	47	1	34	9	40	39	16	5	21	23	24	18	2
Cu	66	1	39	15	38	61	43	9	23	30	28	45	7
Li	10	<10	10	10	10	20	20	10	10	10	20	10	10
Mo	1	5	<1	1	<1	<1	1	<1	1	<1	1	<1	<1
Ni	66	1	50	5	14	28	16	6	11	73	41	13	1
Pb	4	2	6	15	<2	7	14	5	13	6	5	12	39
Sc	38	2	30	10	36	30	12	5	14	14	14	12	2
Tl	<10	<10	10	<10	<10	<10	<10	<10	<10	<10	<10	<10	<10
Zn	94	5	110	57	146	102	72	44	87	80	64	108	15
Ba	68.7	76.8	82	368	51.8	267	529	144.5	282	199	155	278	629
Ce	15.4	20.1	40.4	56.9	30	65.9	44.7	20.6	41.5	22.6	30.6	59.8	26.7
Cr	190	<10	130	10	20	40	30	20	20	100	50	40	<10
Cs	0.28	0.48	1.17	4.27	1.99	1.36	3.17	1.1	0.81	2.17	0.57	2.73	1.28
Dy	7.32	3.45	14.45	5.95	12.4	7.43	2.63	2.01	6.16	3.64	4.92	5.46	1.46
Er	4.87	2.28	9.08	3.65	7.85	4.02	1.35	1.29	3.55	2.13	2.81	3.27	1.15
Eu	1.6	0.26	2.96	0.99	2.64	1.49	0.92	0.65	1.53	1.01	1.21	1.15	0.29
Ga	18.7	13.2	23	18.1	22.4	22.6	20.2	15.4	19.6	17.6	18.6	21.2	16.6
Gd	6.7	2.13	12.9	5.95	11.3	7.5	3.19	2.54	6.46	3.53	4.83	5.65	1.41
Hf	3.9	1.5	9.1	6.1	7	4.4	4.2	3.6	5.6	3.9	4.1	5.4	2.4
Ho	1.74	0.68	3.14	1.22	2.79	1.42	0.46	0.41	1.24	0.78	0.96	1.06	0.31
La	5.2	8.9	13.7	26.5	10.2	23.7	23.3	9.4	18.3	9.9	13.3	30	15.3
Lu	0.66	0.34	1.3	0.46	1.12	0.54	0.19	0.2	0.52	0.27	0.34	0.47	0.23
Nb	2.1	9.1	6.1	9.2	4.4	12.5	9.4	3.8	6.9	3.4	5.2	14.4	8.5
Nd	13	7.4	30.8	27	23.4	39.8	19.9	10	23.4	12.4	17	28.4	9.3
Pr	2.5	2.08	6.3	6.64	4.7	9.29	4.93	2.53	5.39	2.93	3.82	7.06	2.65
Rb	35.1	32	48.7	99.8	9	70.8	61.1	62.6	36.9	116	70.6	97.2	127.5
Sm	5.12	1.86	10.1	6.68	8.67	9.39	3.79	2.27	6.08	3.61	4.66	6.04	1.66
Sn	<1	<1	1	6	1	6	2	1	3	<1	2	5	1
Sr	126.5	120.5	191	218	119	557	569	191	294	246	336	302	204
Ta	0.2	2.6	0.6	0.9	0.5	0.8	0.6	0.3	0.6	0.4	0.5	1.2	1.1
Tb	1.16	0.43	2.27	0.91	1.9	1.17	0.47	0.35	1.01	0.62	0.73	0.84	0.22
Th	0.66	13.85	1.85	11.35	1.51	4.86	9.24	1.77	5.24	2.57	3.72	13.45	13.95
Tm	0.68	0.37	1.33	0.51	1.13	0.62	0.2	0.2	0.54	0.29	0.38	0.48	0.2
U	0.57	8.34	0.48	3.03	0.4	1.28	3.5	0.69	1.81	0.83	1.24	3.68	7
V	352	10	257	56	439	265	134	40	90	119	131	107	13
W	1	1	1	1	<1	1	<1	1	<1	1	1	<1	<1
Y	43.4	19.5	80.6	32.8	71.2	39	13.2	12.2	33.6	20.2	24.8	29.4	9.5
Yb	4.74	2.45	8.86	3.44	7.69	3.82	1.2	1.33	3.48	2.1	2.34	3.02	1.58
Zr	129	31	340	235	246	172	155	143	226	144	163	197	76

Table 9. Geochemical data of igneous samples.

Lithology	Rhyolite	Qz Diorite	Rhyolite	Gabbro	Granodiorite	Gabbro	Diorite	Basalt	Gabbro	Leucogranite	Tonalite	Diorite	Basalt
Locality	62803	62901	63103	63201	63205	63207	63301	63401	63601	63702	63803	64113	64418
	41.00918	41.01180	41.00950	40.98124	41.04530	41.05387	41.00473	40.99055	40.97781	41.03642	41.00678	40.96838	41.03359
Location	95.11318	95.11033	95.10773	95.03667	95.03567	95.03947	95.07069	95.03300	95.09473	95.06303	95.05038	95.03440	95.11065
Major elements (wt-%):													
SiO2	77.5	63	77.3	49.4	66.1	58.9	55	51.3	48.5	77	66.6	47.7	64.2
Al2O3	12.3	15.25	11.9	15.4	15.3	16.55	17.2	12.85	14.6	13.35	14.1	15.5	14.25
Fe2O3	0.57	6.32	0.35	10.65	3.79	7.23	7.22	15.55	12.4	0.5	2.57	10.8	5.38
CaO	1.32	3.76	2.87	11	3.58	5.96	8.07	7.96	9.96	1.3	3.91	11.6	3.29
MgO	0.08	1.94	0.07	7.22	1.78	3.54	4.52	4.55	6.97	0.05	1.07	7.74	1.5
Na2O	4.07	3.95	2.36	2.53	3.84	3.33	3.93	3.53	2.91	3.29	3.42	2.42	4.12
K2O	3.11	2.56	2.56	0.18	3.01	2.58	0.6	0.82	0.74	4.95	1.71	0.14	2.31
Cr2O3	<0.002	0.003	<0.002	0.036	0.003	0.004	0.004	0.006	0.038	<0.002	0.002	0.042	0.002
TiO2	0.06	0.85	0.07	1.52	0.5	0.94	1.38	2.7	1.85	0.04	0.31	1.49	0.76
MnO	<0.01	0.1	0.01	0.17	0.05	0.1	0.14	0.26	0.19	<0.01	0.02	0.17	0.07
P2O5	<0.01	0.24	<0.01	0.16	0.14	0.25	0.16	0.45	0.18	<0.01	0.08	0.11	0.23
SrO	<0.01	0.03	<0.01	0.02	0.07	0.07	0.03	0.01	0.02	0.03	0.02	0.01	0.02
BaO	0.07	0.04	0.05	<0.01	0.09	0.07	0.01	0.01	0.01	0.04	0.03	<0.01	0.04
LOI	2.03	2.2	3.44	1.98	0.81	1.14	1.04	1.49	1.84	0.37	4.78	1.45	2.29
Total	101.11	100.24	100.98	100.27	99.06	100.66	99.3	101.49	100.21	100.92	98.62	99.17	98.46
Trace and rare earth elements (ppm):													
Ag	<0.5	<0.5	<0.5	<0.5	<0.5	<0.5	<0.5	<0.5	<0.5	<0.5	<0.5	<0.5	<0.5
As	51	<5	150	<5	<5	6	<5	<5	<5	<5	<5	<5	<5
Cd	<0.5	<0.5	<0.5	<0.5	<0.5	<0.5	0.6	0.9	0.8	<0.5	<0.5	0.8	<0.5
Co	<1	10	1	40	9	22	27	36	42	1	5	45	10
Cu	35	6	3	62	9	28	4	33	67	3	4	79	15
Li	10	20	<10	10	20	30	10	10	10	<10	10	10	20
Mo	1	<1	1	1	1	1	<1	1	<1	<1	1	<1	<1
Ni	<1	4	<1	103	12	20	19	24	74	<1	9	116	3
Pb	7	17	94	2	20	18	12	5	4	26	5	<2	7
Sc	3	12	2	34	6	15	19	33	42	1	4	37	12
Tl	<10	<10	<10	<10	<10	<10	<10	<10	<10	<10	<10	<10	<10
Zn	6	76	9	85	60	87	74	138	74	5	21	91	62
Ba	620	335	404	32.8	824	574	110	81	58.3	391	231	16.7	405
Ce	34.7	68.1	54.5	15.1	40.8	49.6	24.2	34.9	15.3	3.7	33.8	9.8	64.4
Cr	<10	20	<10	250	30	40	40	50	270	<10	20	300	20
Cs	1.07	1.77	1.69	0.74	1.82	3.75	1.27	0.79	1.15	2.66	1.69	0.59	0.85
Dy	9.2	7.24	8.15	5.63	1.6	3.24	4.19	12.9	6.27	0.55	2.61	5.04	7.46
Er	5.72	4.02	5.08	3.56	0.91	1.9	2.32	8.18	3.85	0.38	1.42	3.21	4.17
Eu	0.8	1.71	0.87	1.27	0.76	1.05	1.08	2.74	1.58	0.26	0.64	1.27	1.72
Ga	16.3	19.5	12.4	16.9	19.3	19.7	18.5	21.8	18.5	17.2	15	17.7	18.5
Gd	7.76	7.63	7.96	4.72	2.24	3.89	3.69	11.75	5.59	0.44	2.96	3.94	7.55
Hf	4.8	9.3	4.8	2.9	3.3	4.1	3	7.7	2.9	1.9	4.3	2.2	8.8
Ho	1.86	1.44	1.76	1.21	0.3	0.63	0.75	2.9	1.27	0.09	0.53	1.03	1.42
La	14.6	31.1	23.7	5.6	19.9	24	10.4	12.2	5.3	2.4	16.7	3	28.7
Lu	0.77	0.63	0.63	0.49	0.11	0.25	0.28	1.17	0.54	0.13	0.18	0.44	0.5
Nb	10.5	9.7	8.3	2.5	7.9	8.9	6	5.1	2.8	2.5	4.5	1.2	9.5
Nd	21	34.6	28.5	12.7	17.3	22.7	15	27	13.1	1.5	14.5	10	33.5
Pr	4.87	8.55	6.96	2.4	4.65	5.85	3.32	5.58	2.44	0.43	3.84	1.71	7.92
Rb	110.5	108.5	100.5	7.9	84.6	95.7	21.2	46.6	35.4	139	76.9	4.9	82.6
Sm	6.53	7.54	7.38	3.92	3.31	4.83	3.62	9.73	4.43	0.41	3.2	3.54	7.57
Sn	1	4	3	1	1	2	2	1	1	1	1	1	4
Sr	63.9	249	82	155	602	527	292	146	204	241	165	162.5	199.5
Ta	1	0.8	1	0.2	0.7	0.6	0.5	0.5	0.4	0.6	0.5	0.1	0.9
Tb	1.4	1.2	1.26	0.79	0.32	0.61	0.64	2	0.91	0.07	0.46	0.71	1.14
Th	12.95	9.54	14.3	0.97	7.02	8.22	2.15	1.62	0.54	12.2	5.57	0.23	9.99
Tm	0.78	0.64	0.68	0.5	0.11	0.24	0.32	1.19	0.55	0.08	0.19	0.46	0.58
U	3.89	3.07	4.49	0.65	2.5	2.84	0.73	0.46	0.31	5.43	1.44	0.13	2.92
V	11	64	<5	255	89	150	168	312	356	8	27	288	59
W	2	<1	1	<1	<1	1	1	1	<1	<1	<1	1	2
Y	49.7	39	44.9	30.6	8.4	16.9	22	75.2	34.3	3.3	13.8	28.5	37.5
Yb	5.37	4.4	4.73	3.43	0.78	1.73	2.19	8.31	3.81	0.58	1.24	3.38	3.8
Zr	107	417	122	116	121	158	119	275	118	44	160	83	382

Table 10, continued. Geochemical data of igneous samples.

		Reference			Result	Δ(res-ref)	95% conf. - |Δ|
major elements:							
Al2O3	%	20.69	±	0.08	20.9	0.210	-0.130
CaO	%	8.05	±	0.04	8.21	0.160	-0.120
Fe2O3t	%	6.21	±	0.03	6.39	0.180	-0.150
K2O	%	1.66	±	0.02	1.67	0.010	0.010
LOI	%	4.56	±	0.07	4.65	0.090	-0.020
MgO	%	0.54	±	0.01	0.54	0.000	0.010
MnO	%	0.108	±	0.001	0.11	0.002	-0.001
Na2O	%	7.1	±	0.05	7.19	0.090	-0.040
P2O5	%	0.131	±	0.004	0.13	-0.001	0.003
SiO2	%	49.9	±	0.1	50.9	1.000	-0.900
TiO2	%	0.287	±	0.003	0.29	0.003	0.000
trace and rare earth elements:							
Ba	µg/g	340	±	5	331	-9.00	-4.000
Ce	µg/g	122	±	2	122	0.00	2.000
Co	µg/g	2.8	±	0.2	3	0.20	0.000
Cr	µg/g	12	±	1	10	-2.00	-1.000
Cs	µg/g	1.5	±	0.1	1.48	-0.02	0.080
Cu	µg/g	7	±	1	5	-2.00	-1.000
Dy	µg/g	18.2	±	0.6	19.05	0.85	-0.250
Er	µg/g	14.2	±	0.5	14.1	-0.10	0.400
Eu	µg/g	2	±	0.04	1.9	-0.10	-0.060
Ga	µg/g	35	±	1	36.1	1.10	-0.100
Gd	µg/g	14	±	0.5	14.05	0.05	0.450
Hf	µg/g	10.6	±	0.4	11.8	1.20	-0.800
Ho	µg/g	4.3	±	0.1	4.51	0.21	-0.110
La	µg/g	58	±	1	57.3	-0.70	0.300
Li	µg/g	37	±	2	40	3.00	-1.000
Lu	µg/g	2.1	±	0.1	2.17	0.07	0.030
Nb	µg/g	13	±	1	13.8	0.80	0.200
Nd	µg/g	57	±	1	56	-1.00	0.000
Ni	µg/g	9	±	1	5	-4.00	-3.000
Pb	µg/g	10	±	1	12	2.00	-1.000
Pr	µg/g	15	±	0.3	14.95	-0.05	0.250
Rb	µg/g	55	±	1.5	52.3	-2.70	-1.200
Sm	µg/g	12.7	±	0.4	14.05	1.35	-0.950
Sr	µg/g	1191	±	12	1250	59.00	-47.000
Ta	µg/g	0.9	±	0.1	0.9	0.00	0.100
Tb	µg/g	2.6	±	0.1	2.69	0.09	0.010
Th	µg/g	1.4	±	0.2	1.1	-0.30	-0.100
Tm	µg/g	2.3	±	0.1	2.31	0.01	0.090
U	µg/g	0.8	±	0.1	0.88	0.08	0.020
V	µg/g	8	±	1.6	7	-1.00	0.600
Y	µg/g	119	±	2	116.5	-2.50	-0.500
Yb	µg/g	14.8	±	0.4	15.55	0.75	-0.350
Zn	µg/g	93	±	2	102	9.00	-7.000
Zr	µg/g	517	±	16	615	98.00	-82.000

Table 10. Comparison of the certified standard composition for SY-4 (Natural Resources Canada, 1995) with the values measured in this study. Values lying outwith the certified 95% confidence intervals are underlined.

		Reference						
		n	stdev	WV	95-% CL	Result	Δ(res-ref)	95% CI - |Δ|
major elements:								
Al2O3	%	115	0.41	10.07	0.08	9.89	-0.18	-0.100
CaO	%	12	0.37	13.87	0.22	14.3	0.43	-0.210
Fe2O3T	%	130	0.35	12.84	0.06	13.3	0.46	-0.400
K2O	%	118	0.11	1.39	0.02	1.4	0.01	0.010
MgO	%	116	0.44	13.15	0.08	13.45	0.3	-0.220
MnO	%	116	0.02	0.2	0.004	0.2	0	0.004
Na2O	%	116	0.23	3.18	0.04	3.16	-0.02	0.020
P2O5	%	92	0.13	1.05	0.03	1.09	0.04	-0.010
SiO2	%	113	0.62	38.2	0.12	38.5	0.3	-0.180
TiO2	%	117	0.14	2.61	0.03	2.67	0.06	-0.030
LOI	%	44	0.4	2.45	P.V.	2.74	0.29	N/A
trace and rare earth elements:								
As	µg/g	13	0.56	1.8	0.3	6	4.2	-3.900
Ba	µg/g	68	125	1025	30	975	-50	-20.000
Cd	µg/g	7	0.08	0.12	P.V.	0.9	0.78	N/A
Ce	µg/g	51	24.08	152	4	147	-5	-1.000
Co	µg/g	62	7.78	60	2	63	3	-1.000
Cr	µg/g	71	48.84	360	12	380	20	-8.000
Cs	µg/g	22	0.33	0.8	0.1	0.66	-0.14	-0.040
Cu	µg/g	56	10.86	72	3	73	1	2.000
Dy	µg/g	18	0.2	6.4	0.2	6.07	-0.33	-0.130
Er	µg/g	15	0.24	2.5	0.1	2.41	-0.09	0.010
Eu	µg/g	36	0.52	3.6	0.18	3.53	-0.07	0.110
Ga	µg/g	22	6.2	17	2	17.6	0.6	1.400
Gd	µg/g	22	1.4	9.7	0.6	9.82	0.12	0.480
Hf	µg/g	23	0.37	5.6	0.16	5.9	0.3	-0.140
Ho	µg/g	12	0.22	1.1	0.13	1.01	-0.09	0.040
La	µg/g	48	3	82	1.5	77.7	-4.3	-2.800
Li	µg/g	28	3.37	13	1.3	10	-3	-1.700
Lu	µg/g	26	0.08	0.24	0.03	0.25	0.01	0.020
Mo	µg/g	9		2.8	0.3	3	0.2	0.100
Nb	µg/g	36	24.01	105	8	107	2	6.000
Nd	µg/g	36	2.6	67	1.5	59.1	-7.9	-6.400
Ni	µg/g	67	26.48	267	7	289	22	-15.000
Pb	µg/g	31	5.38	4	2	8	4	-2.000
Pr	µg/g	11	3.36	17.5	0.6	16.65	-0.85	-0.250
Rb	µg/g	76	8.79	47	2	45.3	-1.7	0.300
Sc	µg/g	30	4.08	22	1.5	21	-1	0.500
Sm	µg/g	36	0.6	12.2	0.3	13	0.8	-0.500
Sn	µg/g	7	0.39	2	0.3	1	-1	-0.700
Sr	µg/g	78	100	1370	25	1400	30	-5.000
Ta	µg/g	20	0.88	5.7	0.4	5.5	-0.2	0.200
Tb	µg/g	24	0.28	1.3	0.1	1.22	-0.08	0.020
Th	µg/g	39	2.01	10.4	0.65	9.89	-0.51	0.140
Tm	µg/g	11	0.07	0.34	0.04	0.33	-0.01	0.030
U	µg/g	30	0.49	2.4	0.18	2.24	-0.16	0.020
V	µg/g	47	33.37	235	10	242	7	3.000
W	µg/g	15	10.73	29	5.6	32	3	2.600
Y	µg/g	45	5	30	1.5	26.5	-3.5	-2.000
Yb	µg/g	36	0.68	1.8	0.2	1.76	-0.04	0.160
Zn	µg/g	61	49.67	120	13	123	3	10.000
Zr	µg/g	60	38.13	260	10	266	6	4.000

Table 11. Comparison of the certified standard composition for BE-N (Govindaraju, 1995) with this study's measured values. Values lying outwith the certified 95% confidence intervals are underlined.

		Reference				2(stdev.)
		WV	stdev	Result	Δ(res-ref)	- |Δ|
major elements:						
Al2O3	%	18.4	0.66	18.35	0.0	1.270
CaO	%	1.1	0.04	1.11	0.0	0.060
Fe2O3	%	5.4	0.13	5.27	-0.1	0.140
K2O	%	4.1	0.2	4.18	0.1	0.290
MgO	%	0.1	0.015	0.12	0.0	0.030
Na2O	%	8.9	0.51	8.84	-0.1	0.960
P2O5	%	0.2	0.02	0.16	0.0	0.030
SiO2	%	61.0	2.95	59.9	-1.1	4.820
TiO2	%	0.2	0.02	0.15	0.0	0.030
trace and rare earth elements:						
Ba	µg/g	639.0	61	668	29.0	93.000
Ce	µg/g	256.0	23	266	10.0	36.000
Cs	µg/g	1.5	0.06	1.42	-0.1	0.020
Eu	µg/g	3.5	0.25	3.4	-0.1	0.450
Ga	µg/g	34.0	1.4	35.6	1.6	1.200
Hf	µg/g	27.0	0.8	27.5	0.5	1.100
La	µg/g	154.0	11	151	-3.0	19.000
Li	µg/g	36.0	4	30	-6.0	2.000
Lu	µg/g	0.6	0.04	0.62	0.0	0.060
Mo	µg/g	6.2	1.1	6	-0.2	2.000
Nb	µg/g	267.0	43	253	-14.0	72.000
Nd	µg/g	81.0	4.8	87.2	6.2	3.400
Pb	µg/g	12.0	1.6	12	0.0	3.200
Pr	µg/g	25.0	1.8	26.2	1.2	2.400
Rb	µg/g	114.0	11	112.5	-1.5	20.500
Sm	µg/g	12.0	0.9	13.65	1.7	0.150
Sr	µg/g	782.0	19	847	65.0	-27.000
Ta	µg/g	16.0	1.1	16.9	0.9	1.300
Th	µg/g	27.0	5	27.4	0.4	9.600
Tm	µg/g	0.6	0.09	0.65	0.1	0.080
Y	µg/g	43.0	2	42.7	-0.3	3.700
Yb	µg/g	4.2	0.08	4.39	0.2	-0.030
Zn	µg/g	223.0	19	247	24.0	14.000
Zr	µg/g	1280.0	62	1380	100.0	24.000

Table 12. Comparison of the certified standard composition for STM-2 (Wilson, 2010) with the values measured in this study. Values lying outwith double the certified standard deviation are underlined.